LEABHARLANN CHOLÁISTE NA TRÍONÓIDE, BAILE ÁTHA CLIATH
Ollscoil Átha Cliath

TRINITY COLLEGE LIBRARY DUBLIN
The University of Dublin

Terms and Conditions of Use of Digitised Theses from Trinity College Library Dublin

Copyright statement

All material supplied by Trinity College Library is protected by copyright (under the Copyright and Related Rights Act, 2000 as amended) and other relevant Intellectual Property Rights. By accessing and using a Digitised Thesis from Trinity College Library you acknowledge that all Intellectual Property Rights in any Works supplied are the sole and exclusive property of the copyright and/or other IPR holder. Specific copyright holders may not be explicitly identified. Use of materials from other sources within a thesis should not be construed as a claim over them.

A non-exclusive, non-transferable licence is hereby granted to those using or reproducing, in whole or in part, the material for valid purposes, providing the copyright owners are acknowledged using the normal conventions. Where specific permission to use material is required, this is identified and such permission must be sought from the copyright holder or agency cited.

Liability statement

By using a Digitised Thesis, I accept that Trinity College Dublin bears no legal responsibility for the accuracy, legality or comprehensiveness of materials contained within the thesis, and that Trinity College Dublin accepts no liability for indirect, consequential, or incidental, damages or losses arising from use of the thesis for whatever reason. Information located in a thesis may be subject to specific use constraints, details of which may not be explicitly described. It is the responsibility of potential and actual users to be aware of such constraints and to abide by them. By making use of material from a digitised thesis, you accept these copyright and disclaimer provisions. Where it is brought to the attention of Trinity College Library that there may be a breach of copyright or other restraint, it is the policy to withdraw or take down access to a thesis while the issue is being resolved.

Access Agreement

By using a Digitised Thesis from Trinity College Library you are bound by the following Terms & Conditions. Please read them carefully.

I have read and I understand the following statement: All material supplied via a Digitised Thesis from Trinity College Library is protected by copyright and other intellectual property rights, and duplication or sale of all or part of any of a thesis is not permitted, except that material may be duplicated by you for your research use or for educational purposes in electronic or print form providing the copyright owners are acknowledged using the normal conventions. You must obtain permission for any other use. Electronic or print copies may not be offered, whether for sale or otherwise to anyone. This copy has been supplied on the understanding that it is copyright material and that no quotation from the thesis may be published without proper acknowledgement.

Investigation of Vertically Stacked Hybrid Devices

by

Chanyoung Yim

A thesis submitted for the degree of Doctor of Philosophy in University of Dublin

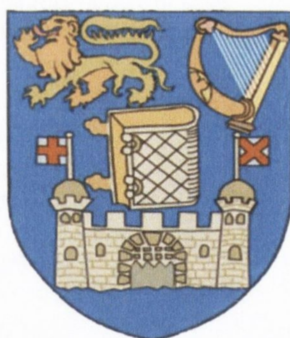

School of Chemistry

Trinity College Dublin

2015

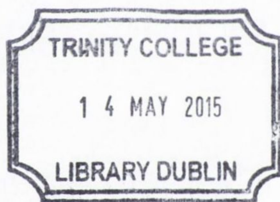
TRINITY COLLEGE
1 4 MAY 2015
LIBRARY DUBLIN

Declaration

I declare that this thesis has not been submitted as an exercise for a degree at this or any other university and it is entirely my own work.

I agree to deposit this thesis in the University's open access institutional repository or allow the library to do so on my behalf, subject to Irish Copyright Legislation and Trinity College Library conditions of use and acknowledgement.

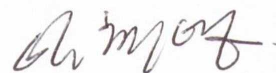

....

Chanyoung Yim

Acknowledgements

First of all, I would like to gratefully and sincerely thank my supervisor, Prof. Georg S. Duesberg for his guidance, support and encouragement over the years.

I also gratefully acknowledge financial support of my PhD from Irish Research Council and Intel via Enterprise Partnership Scheme Postgraduate Research Scholarship. In addition, Chris Murray was my official mentor from Intel and I thank him for his mentoring during my PhD.

I would like to express sincere appreciation to Prof. Gyu-Tae Kim in Korea University since he introduced Prof. Duesberg to me and encouraged me to apply for a PhD position in Trinity College Dublin.

I was hosted at CRANN (Centre for Research on Adaptive Nanostructures and Nanodevices) and School of Chemistry in Trinity College Dublin. By working at CRANN and using their facilities, I was able to become more skilful, build a lot of experiences and finish my study, so I thank these bodies for providing such a good chance to me for finishing my PhD.

Technical supports and training from the staff of CRANN and AML (Advanced Microscopy Laboratory) are very helpful in doing various experiments. Mike Finneran, James Dempsey, and Des Keany managed and maintained CRANN facilities, making everything go smoothly. Cathal McAuley managed all facilities in AML. Tarek Lutz and Dermot Daly helped in using an electron beam lithography tool and scanning electron microscopy. Clive Downing gave some help in HRTEM imaging. I thank all of them.

The completion of my PhD could not have been accomplished without the support of our group members. Parts of my work have been done with the assistance of our group members. They gave enormous supports and help, so I wish to thank them for their assistance, discussions, and contributions to my results. Dr. Niall McEvoy carried out Raman spectra measurements and helped to analyse the data. Dr. Hye-Young Kim shared my work and helped in electron beam lithography. Dr. Kangho Lee set up the electrical measurement system of our group. Ehsan Rezvani did HRTEM imaging of carbon films and Christian Wirtz helped in annealing samples. Maria O'Brien prepared MoS_2 films and conducted its HRTEM imaging, and Sinead Winters measured UV-visible absorption of the MoS_2 films. Moreover, it has been my pleasure to work with

all other group members as well. Dr. Ronan Daly, Anne Weidlich, Dr. Shishir Kumar, Dr. Ashok Kumar Nanjundan, Dr. Toby Hallam, Dr. Nina C. Berner, Dr. Ravi Joshi, Dr. Rohit Mishra, Hugo Nolan and Riley Gatensby, they are really wonderful. I am very pleased to become a member of Prof. Duesberg's group because of them.

Some parts of my work have been done through collaborations with other research groups. Prof. James G. Lunney and Dr. Inam Mirza in School of Physics of Trinity College Dublin helped XRR measurements and its analysis. Prof. Max C. Lemme, Sarah Riazimehr, Dr. Heiko Schäfer-Eberwein and Dr. Andreas Bablich in University of Siegen carried out spectral response measurements of MoS_2 films. Prof. Gianluca Fiori, Prof. Giuseppe Iannaccone and Dr. Ravinder Pawar in University of Pisa conducted density functional theory calculations of MoS_2 films. I really appreciate all their contributions.

I would like to deeply thank my parents and my wife's parents for their great support and love. They always respect my decision, encourage me to do what I want to do, and never stop sending endless support. I also thank my brother and sisters for their consistent help and kindness. Finally I thank my wife for all her love and devotion in past year. This thesis is dedicated to her.

Abstract

Conductive carbon thin films are known to be promising candidates for future electrode materials for micro/nano-electronic device applications due to their favourable electrical properties and diversity of formation. In particular, recent enormous interest in graphene, a two-dimensional carbon material, has triggered many broad and comprehensive studies not only on graphene itself, but also on other two-dimensional layered materials such as transition metal dichalcogenides. The introduction of such materials to real electronic device applications can be effectively achieved by making hybrid devices where these materials are combined with conventional semiconductors in device fabrication. Therefore, it is very important to understand and define the electrical characteristics of such hybrid devices thoroughly in the initial stages of research.

In this thesis two types of hybrid electronic devices have been realised using conductive carbon materials and a semiconducting transition metal dichalcogenide thin film, respectively. Material properties have been characterised by a number of techniques and integrated with standard silicon technology. The electrical characteristics of the resulting devices have been investigated using several experimental techniques.

First, Schottky barrier diodes have been fabricated on silicon substrates using three different conductive carbon thin films namely pyrolytic carbon, glassy carbon from pyrolysed photoresist and graphene. Pyrolytic carbon and glassy carbon thin films are deposited on n-type silicon wafers by chemical vapour deposition and by pyrolysing pre-coated photoresist, respectively, resulting in Schottky contacts with the n-type silicon substrates. Graphene is grown on copper foils using chemical vapour deposition and transferred onto pre-patterned n-type silicon substrates in order to fabricate Schottky diodes. The carbon thin films have been characterised using various experimental techniques such as electron microscopy, Raman spectroscopy, and spectroscopic ellipsometry throughout the fabrication process. Important electrical parameters of the Schottky diodes including the Schottky barrier height, the ideality factor, and series resistance are extracted by analysing the dc current-voltage measurement data. Furthermore, ac impedance spectra of the Schottky diodes are measured. The impedance data of the devices can be interpreted by simulating the experimental data using a developed equivalent circuit model. Applying the ac

impedance spectroscopy technique, the effects of the metal electrode contacts of the devices, which cannot be determined from the dc current-voltage measurements, are verified and additional information on the Schottky contacts is obtained, including the built-in potential and a more reliable value of the barrier height.

Next, vertically stacked p-n heterojunction diodes consisting of a thin n-type molybdenum disulfide film and p-type silicon have been investigated. A vapour phase sulfurisation process is used to grow continuous large-scale molybdenum disulfide thin films from pre-deposited molybdenum metal layers on insulators. Molybdenum disulfide thin films with various thicknesses can be obtained by modulating the pre-deposited molybdenum metal thickness. The grown thin films have been characterised using electron microscopy, Raman spectroscopy, UV-visible absorption spectroscopy and spectroscopic ellipsometry. The n-type molybdenum disulfide thin films are transferred onto the pre-patterned p-type silicon substrates, forming p-n heterojunction diodes. The fabricated large-scale p-n heterojunction diodes show notable photoconductivity which can be tuned by modifying the thickness of the molybdenum disulfide layers. Moreover, spectral response measurements reveal that the p-n heterojunction diodes have a broad spectral response resulting from direct and indirect band transitions of the nanoscale molybdenum disulfide thin films.

In summary, a number of diodes have been realised with the novel thin films. They have been characterised using various methods, which proves that they have high performance, thus can be possibly used in practical device applications.

Table of Contents

Acknowledgements i

Abstract iii

Table of Contents v

List of Figures viii

List of Tables xviii

List of Acronyms xx

1. Introduction 1

1.1 Conductive Carbon Materials 1
1.1.1 Glassy Carbon Films 2
1.1.2 Pyrolytic Carbon Films 4
1.1.3 Graphene 7
1.2 Molybdenum Disulfide 10
1.3 Schottky Barrier Diodes 13
1.4 Photodiodes 17
1.5 Outline of Thesis 21

2. Experimental Methods 22

2.1 Chemical Vapour Deposition 22
2.2 Pyrolysis of Photoresist Films 24
2.3 Electron Microscopy 25
2.4 Raman Spectroscopy 27
2.5 Spectroscopic Ellipsometry 31
2.6 Electrical Measurement 33
2.7 Impedance Spectroscopy 35

3. Conductive Carbon-Silicon Schottky Contacts 40

3.1 Schottky Contacts between PyC/PPF and Silicon 40
3.1.1 Background 40
3.1.2 Film Synthesis 41
3.1.3 Film Characterisation 42
3.1.4 Device Fabrication 47
3.1.5 Current-Voltage Measurement 48
3.1.6 Impedance Spectroscopy 53
3.1.7 Conclusion 62
3.2 Graphene-Silicon Schottky Contacts 64
3.2.1 Background 64
3.2.2 Graphene Growth 65
3.2.3 Device Fabrication 66
3.2.4 Film Characterisation 67
3.2.5 Current-Voltage Measurement 70
3.2.6 Impedance Spectroscopy Measurement 72
3.2.7 Conclusion 77

4. Heterojunction Hybrid Devices from Vapour Phase Grown MoS_2 79

4.1 Background 79
4.2 MoS_2 Synthesis 79
4.3 Film Characterisation 80
4.3.1 Thickness Measurements 80
4.3.2 Raman Analysis 81
4.3.3 HRTEM Analysis 83
4.4 Device Fabrication 84
4.5 Current-Voltage Measurement 85
4.6 Photoconductivity 88
4.7 Spectral Response 91
4.8 Conclusion 96

5. Summary and Future Work 97

5.1 Summary 97
5.2 Future Work 98

Appendix 102

A.1 Analysis of MoS_2 Thin Films using Spectroscopic Ellipsometry 102
A.1.1 Background 102
A.1.2 MoS_2 Synthesis 103
A.1.3 Film Characterisation 103
A.1.4 Optical Properties Analysis 104
A.1.5 Optical Band Gap 110
A.1.6 Conclusion 112

List of Publications and Presentations 114

References 117

List of Figures

Figure 1 Crystal structures of the different allotropes of carbon. Three-dimensional (3D) diamond and graphite, two-dimensional (2D) graphene, one-dimensional (1D) nanotubes, and zero-dimensional (0D) buckminsterfullerenes (C_{60}).[14] 2

Figure 2 Structure of glassy carbon.[20] 3

Figure 3 The chemical structure of the main repeated unit in AZ nLof 2070 resin (2-methoxy-1-methylethyl acetate). 4

Figure 4 Schematics of the nanocrystalline structure of PyC (top left) and different orientations of PyC (top right).[35] TEM images of three PyC textures: isotropic, smooth laminar and rough laminar from bottom left to right.[38] 5

Figure 5 General reaction scheme describing the process of PyC deposition from a hydrocarbon (left) and its corresponding reaction scheme in the case of PyC deposition from methane (right). 6

Figure 6 HRTEM images of the interface between PyC and the SiO_2 substrate. (growth condition t = 15 min, P = 20 Torr, T = 950 °C).[41] 6

Figure 7 Hexagonal honeycomb lattice of graphene with two atoms (A and B) per unit cell (left), and schematic energy band structure of monolayer graphene where its conduction and valence bands touch each other at the Dirac point (right). Depending on the nature of the doping and the transport carrier, the position of the Fermi level varies. 7

Figure 8 Schematic representation of the crystal structure of bulk MoS_2. 10

Figure 9 Energy band structure of the metal and semiconductor (a) before contact, (b) after contact, (c) under forward bias (V_F) and (d) reverse bias (V_R). 14

Figure 10 Electron-hole photo-generation in a semiconductor.............................17

Figure 11 Plot of current-voltage measurements for a commercial silicon photodiode (BPW21, OSRAM) under different incident light power. 18

Figure 12 Cross sectional view of the p-n semiconductor diode structure and its energy band diagram under illumination..18

Figure 13 CVD mechanism; (1) diffusion of reactant to surface, (2) absorption of reactant to surface, (3) chemical reaction, (4) desorption of by-product gas, (5) out-diffusion of by-product gas. 22

Figure 14 A schematic of the furnace system used for pyrolysis. 24

Figure 15 The Schematic outline of TEM (left)[136] and SEM (right).[137] 26

Figure 16 Raman spectrum of a nano-graphite sample taken with a laser excitation energy (wavelength) of 2.41 eV (514.5 nm).[139] 28

Figure 17 Raman spectra of monolayer, bilayer, three layers, and four layers graphene on (a) quartz and (b) SiO_2/Si substrate. The enlarged 2D-band regions with curve fit are also shown in panels (c) and (d).[141] 28

Figure 18 Raman spectra of bulk, single-, and few-layer MoS_2 films.[25] 29

Figure 19 Photograph of a Witec Alpha 300R confocal Raman microscope. 30

Figure 20 Interaction of polarised light with a sample in the ellipsometry system (left)[146] and photograph of Alpha SE (J. A. Woollam Co.) measurement system (right). 32

Figure 21 Four-point probe method of measuring resistivity. 33

Figure 22 Image of the probe station connected with a Keithley 2400 SMU (left) and schematic of operation principle for two-terminal needle prober for electrical characterisation of carbon-silicon SBD (right). 34

Figure 23 Current-voltage plot measured from a diode, giving a general idea of IS measurements. 35

Figure 24 Nyquist plot (left) and Bode plot (right) which was measured from the same system. 37

Figure 25 Examples of Nyquist plots of IS spectra measured from a serially (left) and parallel (right) connected RC system. 37

Figure 26 Equivalent electrical circuit model of a system consisting of RC components (left), and the experimental data measured by IS and its simulated values (right) using the equivalent circuit model. 38

Figure 27 Serial and parallel combinations of impedances. 39

Figure 28 Cross-sectional SEM images of (a) PPF and (b) PyC, and HRTEM images of (c) PPF and (d) PyC on silicon substrates. 43

Figure 29 Raman spectra of PPF and PyC films with an excitation wavelength of 532 nm exhibiting broad D and G bands. 44

Figure 30 Optical constants (n and k) plots for (a) PPF and (b) PyC films from this work. (c) n and k values of glassy carbon (GC) and PPF from ref[177]. (d) n and k values of pyrolytic graphite from ref[178]. 46

Figure 31 Carbon-silicon SBD device fabrication process. 47

Figure 32 Schematic and optical microscope image (top view) of the carbon/n-Si Schottky barrier diode. 48

Figure 33 *J-V* measurements of (a) the PPF/n-Si SBD and (b) the PyC/n-Si SBD on a linear scale. Insets denote the plots on a semi-logarithmic scale and the dc equivalent circuit model of the diode. Plots of *dV/d(*ln*J)* vs. *J* and *H(J)* vs. *J* for (c) the PPF/n-Si and (d) the PyC/n-Si SBDs. (e) Energy-band diagram of a conductive carbon thin film on n-Si substrates under zero, forward and reverse bias. φ_B, E_c, E_v, E_F, E_{FC}, V_{bi}, V_{for} and V_{rev} indicate the Schottky barrier height, bottom energy of conduction band of n-Si, top edge of valence band of n-Si, Fermi energy level of n-Si, Fermi energy level of carbon, built-in potential, forward bias and reverse bias, respectively. 50

Figure 34 Semi-logarithmic current-voltage curves of six different carbon/n-Si Schottky diode devices for (a) PPF/n-Si diode and (b) PyC/n-Si diode. 52

Figure 35 Nyquist plots of the PPF/n-Si SBD (a) under forward dc bias voltages and (b) under zero and reverse dc bias voltages. Nyquist plots of the PyC/n-Si SBD (c) under forward dc bias voltages and (d) under zero and reverse dc bias voltage with frequencies increasing from the right to the left of the x axis (from 0.1 Hz to 1 MHz). 53

Figure 36 (a) A typical equivalent circuit model (ECM 1) of a Schottky diode. C_P denotes the depletion layer capacitance of the contact, R_P is associated with a shunt resistance and R_S is a series resistance. (b) ECM 2 with C_1 and C_2 being capacitances with corresponding shunt resistances R_1 and R_2 associated with the interfaces of metal electrodes (Ni-carbon and silicon-Ti) and a carbon-silicon interface , respectively. (c) ECM 3 with C_1, C_2 and C_3 being capacitances with corresponding shunt resistances R_1, R_2 and R_3, associated with a Ni-carbon interface, a carbon-silicon interface and a silicon-Ti interface, respectively. R_S is the series resistance and *L* represents a parasitic inductance associated with the electrical leads. 54

Figure 37 Nyquist plots and corresponding best fit from the equivalent circuit models of ECM 1, ECM 2 and ECM 3 on the PPF/n-Si SBD (a) under dc bias of

+0.4 V and (b) -0.4 V, and the PyC/n-Si SBD (c) under dc bias of +0.4 V and (d) -0.4 V. 56

Figure 38 Nyquist plots and corresponding best fit from ECM 3 on the PPF/n-Si SBD under dc bias of (a) +0.6 V, (b) +0.2 V, (c) -0.2 V and (d) -0.6 V. 57

Figure 39 Nyquist plots and corresponding best fit from ECM 3 on the PyC/n-Si SBD under dc bias of (a) +0.6 V, (b) +0.2 V, (c) -0.2 V and (d) -0.6 V. 58

Figure 40 Resistance and capacitance values for dc bias voltages in the range of +0.6 V-0.6 V obtained from the best fit of the measured impedance spectra of the PPF/n-Si (a, b) and PyC/n-Si (c, d) SBDs using ECM 3. 59

Figure 41 The plot of $1/C^2$ vs. V for the PPF/n-Si and PyC/n-Si SBDs with C_2 values derived from the simulated results using ECM 3. 62

Figure 42 Process flow of graphene transfer onto the pre-patterned substrate using a polymer-supported transfer method. 66

Figure 43 (a) Photograph of the G/n-Si SBD device (top) and its schematic diagram (bottom). (b) Average Raman spectrum of high quality graphene on the SiO2 layer of the device. 67

Figure 44 (a) Optical micrograph of area of graphene scanned. Raman maps of (b) D band intensity, (c) G band intensity, (d) 2D band intensity, (e) D/G intensity ratio and (f) Lorentzian fit of 2D band FWHM were extracted. 68

Figure 45 (a) 2D FWHM Raman map marked with spots 1 and 2 from which point spectra were extracted. (b) Average Raman spectrum of the sample as well as point spectra from spots 1 and 2, normalized to the G band intensity. (c) Average Raman spectrum of the sample as well as point spectra from spots 1 and 2 normalized to the 2D band intensity so as to highlight the change in 2D band shape and FWHM. (d) Lorentzian fitting of the 2D band for spot 2 indicating a FWHM of 26 cm^{-1}. 69

Figure 46 Dark J-V measurement of the G/n-Si SBD on a linear scale. Inset: J-V curve on a semi-logarithmic scale. 71

Figure 47 Plots of $dV/d(\ln J)$ vs. J and $H(J)$ vs. J for the G/n-Si SBD. 72

Figure 48 Nyquist plots of the G/n-Si SBD under (a) forward, (b) zero and reverse dc bias. 73

Figure 49 Equivalent circuit model of the G/n-Si SBD for the IS analysis where R_1C_1, R_2C_2 and R_3C_3 represent the RC networks related to the interfaces of Au-graphene, graphene-Si and Si-Ti respectively. R_S is the series resistance and L represents a parasitic inductance associated with the electrical leads. 73

Figure 50 Nyquist plots and corresponding fit from the equivalent circuit model on the G/n-Si SBD under dc bias of (a) +0.4 V, (b) 0.0 V, (c) -0.3 V and (d) -0.5 V. 75

Figure 51 Semi-logarithmic plots of (a) resistance and (b) capacitance values for dc bias voltages in the range of +0.6 V to -0.6 V achieved from the best fit of the impedance spectra of the G/n-Si SBD using the equivalent circuit model of Figure 49. 75

Figure 52 Mott-Schottky plot ($1/C^2$ vs. V) of the G/n-Si SBD with C_2 values extracted from the simulated results using the equivalent circuit model of Figure 49. 77

Figure 53 Schematic diagram of the vapour phase sulfurisation process used for MoS_2 thin film synthesis. 80

Figure 54 Raman spectra of the MoS_2 thin films with various thicknesses grown by vapour phase sulfurisation of Mo thin films. A slight shift of the E^1_{2g} band is evident. 81

Figure 55 (a) Optical microscopy image of MoS_2 film transferred onto SiO_2. The red box indicates the 25 × 25 μm area over which Raman spectra were acquired.

(b) Raman spectrum obtained by averaging over 10,000 discrete spectra which comprised the Raman map. Raman maps showing the intensity of the (c) E^{1}_{2g} and (d) A_{1g} peaks. 82

Figure 56 HRTEM image of a MoS_2 thin film transferred to a TEM grid (Inset: a corresponding image at high magnification). 83

Figure 57 Representative electron diffraction patterns from different areas of the MoS_2 film revealing Mo-Mo lattice spacing of (a) 0.324 nm and (b) 0.306 nm, respectively. 84

Figure 58 Transfer process of as-grown MoS_2 thin films onto the pre-patterned substrate. 85

Figure 59 Schematic (left) and photograph (right) of the n-type MoS_2/p-Si heterojunction diode. 86

Figure 60 A *J-V* plot of the diode with 12.52 nm thick MoS_2 on a linear scale (left) and semi-logarithmic scale (right) under dark (black) and illuminated (red) conditions. Inset of the left indicates open-circuit voltage (0.13 V) and short-circuit current (0.01 mA/cm^2). 86

Figure 61 Plot of *dV/dJ* vs. *1/J* extracted from the *J-V* data of the diode with 12.52 nm thick MoS_2, giving a series resistance value of 7.3 kΩ and an ideality factor value of 1.68. 87

Figure 62 Cross sectional view of the n-type MoS_2/p-Si diode structure (left) and its energy band diagram in reverse bias (right) under illumination, describing the movement of electrons (ⓔ) and holes (ⓗ). E_c, E_F, E_v, E_g and hv denote the conduction band, Fermi energy level, valence band, band gap and photon energy of the incident light, respectively. 88

Figure 63 (a) J-V plot of the diode with the 12.52 nm thick MoS_2 film under various incident light intensities (dark, 10, 30, 60 and 100 % of full intensity) and (b) an associated photocurrent density (J_{ph}) plot extracted from the J-V measurements in the reverse bias region. 89

Figure 64 A J_{ph} plot with varying incident light intensity at reverse biases of V = -1 and -2 V. 90

Figure 65 Semi-logarithmic J-V plots of the MoS_2/p-Si diode devices with MoS_2 film thickness of (a) 4.17 nm, (b) 8.26 nm, and (c) 15.96 nm in the dark and illumination (5 % of full intensity). (d) A plot of J_{ph} of the diode devices with different MoS_2 thickness (4.17, 8.26, 12.52 and 15.96 nm) under reverse dc bias. 91

Figure 66 (a) Schematic of the heterojunction diode with mask openings for MoS_2 and p-Si indicated for spectral response measurements. (b) Plot of absolute spectral response (Abs. SR) vs. wavelength (lower x-axis) and energy (upper x-axis) related to the diode device with an 8.26 nm thick MoS_2 film at zero bias and reverse bias (V_R) of 1 and 2 V with the mask openings on MoS_2 and (c) p-Si. The inset indicates the area of the diode illuminated. 92

Figure 67 Plot of absolute spectral response (Abs. SR) vs. wavelength (lower x-axis) and energy (upper x-axis) related to the diode device with an 8.26 nm thick MoS2 film at zero bias and reverse bias (VR) of 1 and 2 V with the mask openings on p-Si. 93

Figure 68 (a) Calculated energy bands for bulk MoS_2. (b) Variation of the direct and indirect band gaps, with respect to the equilibrium case, as a function of the interlayer distance (expressed in %) and (c) variation of the direct and indirect band gaps, with respect to the equilibrium case, as a function of the lattice spacing (expressed in %). 94

Figure 69 Schematic diagram of a graphene-silicon SBD sensor. Example of the chemical sensor device (top) showing variation of the series resistance of the SBD

as a function of the concentration of anisole in benzene, and example of gas sensor (bottom) showing change of current-voltage characteristics of the SBD depending on the concentration of ammonia in argon.[193] 99

Figure 70 Optical image of triangular vapour phase sulfurised MoS_2 on a SiO_2/Si substrate and its dark-filed TEM image with the diffraction pattern inset showing that the triangle is a continuous single crystal (top row).[216] Schematic diagram of a single-crystalline monolayer MoS_2 FET device and atomic force microscopy image (10 μm) of a two-terminal FET device where the shape of the triangular crystal is highlighted (bottom row).[218] 100

Figure A - 1 Photograph of MoS_2 samples synthesised by vapour phase sulfurisation with increasing thickness (A – E). 103

Figure A - 2 Raman spectra of the MoS_2 thin films on the SiO_2/Si substrates (sample A, B, C, D and E). 104

Figure A - 3 Schematic diagram of the optical model of MoS_2 samples and SE measurement system. 105

Figure A - 4 Plots of the experimental and simulated (model) SE spectra (psi and delta) of MoS_2 samples A – E ((a) – (e)). 107

Figure A - 5 Representative plot of XRR data measured from sample E for the thickness measurement. 109

Figure A - 6 Plots of (a) the refractive index *n* and (b) extinction coefficient *k* values of the MoS_2 layers for the five samples (A, B, C, D and E) derived from the optical model with the best fits. The inset of (b) shows a UV-visible absorption spectrum of a MoS_2 thin film on a quartz substrate. 110

Figure A - 7 Plots of $(\alpha h\nu)^{1/2}$ vs. $h\nu$ for sample A, B, C, D and E. The extrapolation of the linear region to $(\alpha h\nu)^{1/2} = 0$ (red line) gives the E_g value.......................... 111

Figure A - 8 Plot of E_g vs. MoS_2 thickness/layer number obtained from this work (circle) and literature[106] (triangle). It is assumed that single layer MoS_2 thickness is 0.65 nm. 112

List of Tables

Table 1 Electron affinity of some semiconductors.[130] 16

Table 2 Work functions of some metal elements.[130] 16

Table 3 Summary of resist thickness before and after pyrolysing.[28] 24

Table 4 Mathematical expression of impedances for commonly used circuit elements. 38

Table 5 The summary on the oscillator parameters of the Tauc-Lorentz model developed for the material dispersion models of PPF and PyC. (MSE*: Root Mean Square Error). 45

Table 6 Summary of data taken on six different carbon/n-Si Schottky barrier diode devices at room temperature. 52

Table 7 Values of R_1, C_1, R_2, C_2, R_3, C_3, R_S and L along with the applied dc bias voltages from +0.6 V to -0.6 V obtained from the best fit of the measured impedance spectra of the PPF/n-Si SBD using ECM 3. 60

Table 8 Values of R_1, C_1, R_2, C_2, R_3, C_3, R_S and L along with the applied dc bias voltages from +0.6 V to -0.6 V obtained from the best fit of the measured impedance spectra of the PyC/n-Si SBD using ECM 3. 60

Table 9 Summary of peak intensity ratio (I_{2D}/I_G), peak position and FWHM for the 2D and G band in Figure 45(b). 69

Table 10 Summary of the ideality factor (n) and SBH ($q\varphi_B$) values of different graphene-silicon SBDs. 72

Table 11 Values of R_1, C_1, R_2, C_2, R_3, C_3, R_S and L along with the applied dc bias voltages from +0.6 V to -0.6 V obtained from the best fit of the measured impedance spectra of the G/n-Si SBD using the equivalent circuit model of Figure 49. 76

Table A - 1 Thickness values of the MoS_2 thin films (sample A, B, C, D and E) from SE and fitting parameter values of the Tauc-Lorentz (T-L) oscillation model for the best fit. 108

Table A - 2 Summary of the MoS_2 thickness values from SE data and XRR measurements for the five MoS_2 samples (sample A, B, C, D and E). Thickness values of samples A and B from XRR measurements are not available due to the thickness resolution limit of XRR. 109

List of Acronyms

CCD	Charge-Coupled Device
C-V	Capacitance-Voltage
CVD	Chemical Vapour Deposition
DRAM	Dynamic Random-Access Memory
FET	Field Effect Transistor
FWHM	Full Width at Half Maximum
G-Si	Graphene-Silicon
HF	Hydrofluoric Acid
HRTEM	High Resolution Transmission Electron Microscopy
HOPG	Highly Oriented Pyrolytic Graphite
IS	Impedance Spectroscopy
J-V	Current-Voltage
M-S	Metal-Semiconductor
MFC	Mass Flow Controllers
MSI	Metal-Silicon-Insulator
n-Si	n-type Silicon
PMMA	Poly(methyl methacrylate)
p-Si	p-type Silicon
PPF	Pyrolysed Photoresist Film
PyC	Pyrolytic Carbon
SBD	Schottky Barrier Diode
SBH	Schottky Barrier Height
sccm	Standard Cubic Centimetres per Minute
SE	Spectroscopic Ellipsometry
SEM	Scanning Electron Microscope
SiC	Silicon Carbide
SMU	Source Meter Unit
SWE	Single Wavelength Ellipsometry
TEM	Transmission Electron Microscope
T-L	Tauc-Lorentz
TMD	Transition Metal Dichalcogenide

XRR X-ray Reflectivity

1. Introduction

1.1 Conductive Carbon Materials

Conductive carbon materials have been studied in various research fields including analytical chemistry, materials science as well as industrial electrochemistry due to its great diversity of formation and notable potential in commercial applications.

As shown in Figure 1, there are several very well-known allotropes of carbon such as three-dimensional (3D) graphite and diamond, two-dimensional (2D) graphene, one-dimensional (1D) carbon nanotubes, and zero-dimensional (0D) buckminsterfullerenes (C_{60}), each of which can exist in a variety of configurations with different electrical and chemical properties. Many common materials for electrodes are based on the graphitic structure. It has a 3D structure which consists of sheets of graphene stacked like parallel sheets of chicken wire. Each carbon atom in a single sheet is covalently bonded to three other surrounding carbon atoms. The flat sheets of carbon atoms are bonded into hexagonal structures and these exist in layers. Different layers are connected together by weak forces called van der Waals forces.[1-4] The 3D graphite materials are comprised of highly oriented pyrolytic graphite (HOPG) and natural crystalline graphite. HOPG is synthesised by high temperature decomposition of gaseous hydrocarbons, followed by hot pressing at high pressure and temperature. Graphite materials have a variety of crystalline and disordered structures depending on their synthesis process. Diamond, another form of 3D carbon-based material, is basically an insulator in its pure state, but recent studies have revealed that dopants can imbue diamond with sufficient conductivity for high-power and high-frequency electronics.[5-7] Carbon nanotubes, which can be described as single or multiple layers of graphite sheets rolled up to form tubes of varying diameter and length, are of interest for a number of applications due to their unique electronic properties.[8,9] They can be semiconducting or metallic depending on their structure. The most recently discovered allotrope is graphene, which is the simplest graphitic material having a 2D structure. Many studies on the synthesis and properties of a wide variety of graphene structures have recently been performed[10] and its experimental discovery led to the award of the Nobel Prize in 2010.[11-13]

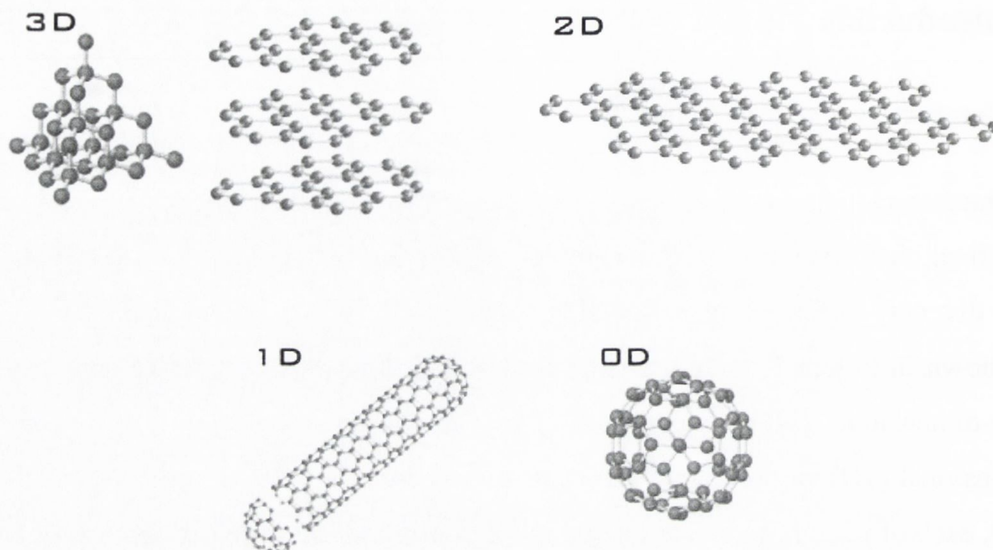

Figure 1 **Crystal structures of the different allotropes of carbon. Three-dimensional (3D) diamond and graphite, two-dimensional (2D) graphene, one-dimensional (1D) nanotubes, and zero-dimensional (0D) buckminsterfullerenes (C_{60}).[14]**

1.1.1 Glassy Carbon Films

Glassy carbon is made by heat treatment of various polymers and has different properties from other disordered graphitic materials, such as amorphous carbon, polycrystalline graphite, and carbon black.[15] By heating the polymer under pressure in an inert atmosphere to 1000 – 3000 °C, the heteroatoms are evaporated until only carbon remains.[16] When heated slowly in a suitable environment to high temperatures, the polymers decompose and reorganise to produce a network of bonded carbon atoms. The C-C bonds in the polymer backbone do not break at these temperatures, so the carbon can only form graphitic planes of limited size. The interplanar spacing is larger than that of HOPG, about 0.36 nm. As shown in Figure 2, the structure is generally presented as randomly intertwined ribbons of graphitic planes, although the randomness results in significant uncertainty about the detailed microstructure.[17-20] It is known that glassy carbon has about 60 % of the density of HOPG and must contain many voids, but its disordered nature makes structural characterisation difficult at the atomic level. Glassy carbon can also be made from a reactive polymeric precursor at relatively low temperature (~ 700 °C), which permits doping with various hetero-atoms in the

polymer, as well as the final product, including halogens, silicon, and metal catalysts.[21-23] As for electrochemical applications, bulk glassy carbon has been commercially used as an electrode material for over half a century due to its excellent thermal and electrical stability, large potential window, and low background noise.[24] Its good electrical conductivity lends to applications in micro-batteries where micro-machined structures of glassy carbon are used as electrodes.[25]

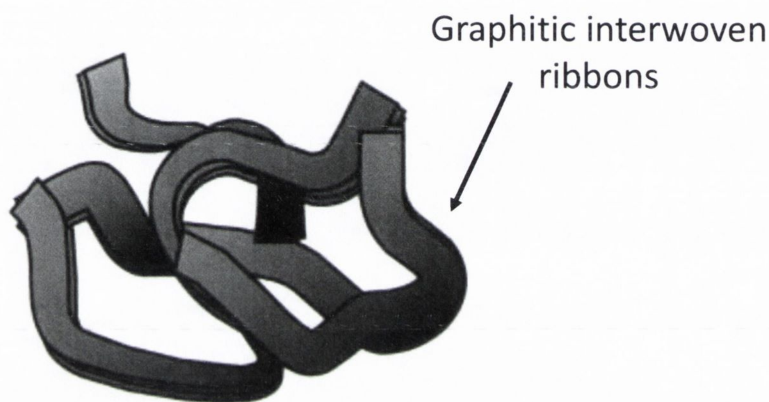

Figure 2 **Structure of glassy carbon.[20]**

Pyrolysed photoresist films (PPFs) are electrically conductive materials with a microstructure much like that of glassy carbon. PPFs have tuneable conductivity via modulation of the pyrolysis temperature and have been investigated as transparent conductors.[26-28] In addition, PPFs have little surface oxygen due to hydrogen termination during the pyrolysis, and therefore are relatively resistant to oxidation on air.[29] Also, the cost of the fabrication is inexpensive, compared to glassy carbon. In general, PPFs can be prepared by spin-coating a thin layer of photoresist onto a clean inert substrate (e.g. Si, SiO_2, and Al_2O_3). The thickness of the photoresist layer can be controlled by the spin speed and photoresist viscosity. Afterwards the coated substrate is soft-baked at approximately 90 – 100 °C for 2 minutes on a hotplate, the substrate is placed in a quartz tube furnace for pyrolysis. The pyrolysis is usually conducted at 1000 °C for 1 hour under inert gas atmosphere. A certain amount of film shrinkage occurs during pyrolysis, primarily in the film thickness, due to decomposition of the photoresist. The main benefits of PPF films are their very high smoothness and the possibility of patterning the films before pyrolysis by photolithography.[26,30-34]

In the previous work of our group, the fabrication of thin conductive carbon layers by pyrolysing a layer of photoresist (AZ nLof 2070) was demonstrated.[28] AZ nLof 2070, which is a negative tone photoresist, was used as the polymer material to obtain a conductive carbon thin film. The chemical structure of AZ nLof 2070 is shown in Figure 3. The PPF showed high conductivity with an average value of 1.6×10^4 S/m and a surface roughness less than 0.2 nm. Due to its high conductivity and smoothness, PPF can be used as an electrode material in micro-electrical devices.

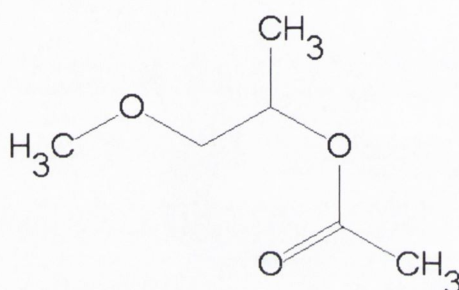

Figure 3 **The chemical structure of the main repeated unit in AZ nLof 2070 resin (2-methoxy-1-methylethyl acetate).**

1.1.2 Pyrolytic Carbon Films

Pyrolytic carbon (PyC), also called pyrocarbon, is a disordered form of graphite in which the graphene sheets are arranged parallel in domains, having nanoscale crystallinity. PyC can be formed through gas phase dehydrogenation (or pyrolysis) of hydrocarbons. As shown in Figure 4, PyC can have different order depending on the growth parameters used.[35] Lieberman and Pierson classified PyC into three textures depending on the degree of anisotropy, which are the isotropic, smooth laminar and rough laminar PyC (Figure 4).[36] Furthermore, they examined the relationship between the molar ratio of hydrocarbon species R = C_2H_2/C_6H_6 and the resultant PyC microstructure.[37] According to their results, rough laminar PyC is formed for a molar ratio R in the range of 5 – 20, smooth laminar PyC for lower values and isotropic PyC for higher values.

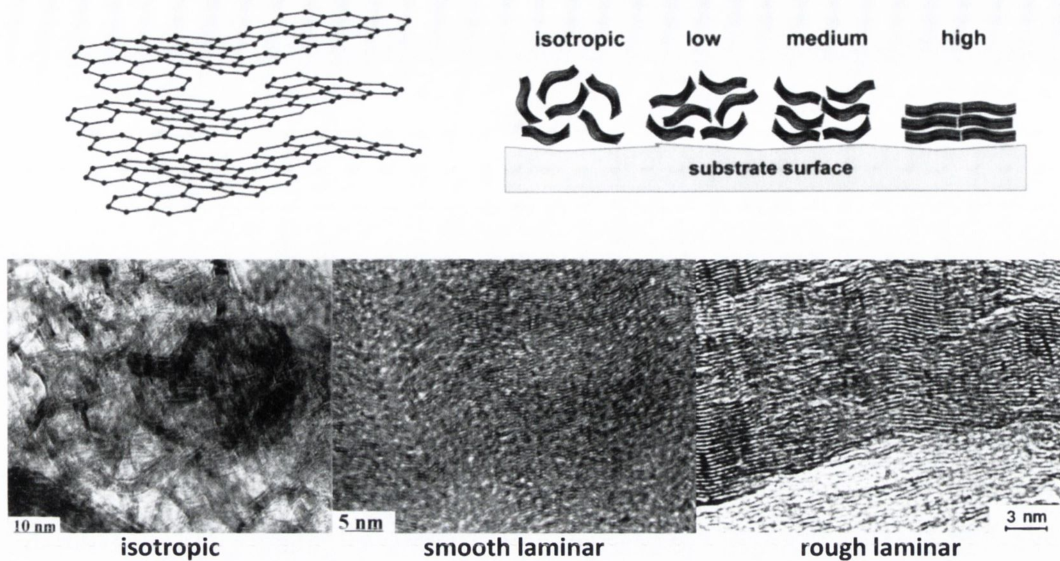

Figure 4 Schematics of the nanocrystalline structure of PyC (top left) and different orientations of PyC (top right).[35] TEM images of three PyC textures: isotropic, smooth laminar and rough laminar from bottom left to right.[38]

The pyrolysis of hydrocarbons is a complex process with a large number of different reaction pathways. Benzinger *et al.* demonstrated that deposition reactions of PyC are heterogeneous surface reactions which are in competition with homogeneous gas-phase reactions.[39,40] They suggested a general reaction scheme to describe the process of PyC deposition from a hydrocarbon, as shown in Figure 5. It is assumed that a hydrocarbon A cannot form PyC directly. In the first step, an intermediate B is generated from the corresponding homogeneous reaction (k_1). The intermediate B forms PyC from the heterogeneous reaction on the substrate (k_3), and at the same time it forms another intermediate C from the corresponding reaction (k_2), which also forms PyC from the heterogeneous reaction (k_4). This reaction scheme was adopted in the case of PyC deposition from methane (CH_4), where the species A, B and C correspond to the C_1 hydrocarbon methane, the C_2 hydrocarbons ethylene (C_2H_4) and acetylene (C_2H_2), and the C_6 hydrocarbon benzene (C_6H_6). The homogeneous gas-phase reactions involve dehydrogenation and cracking reactions of hydrocarbons. Although complex reactions are occurring in the gas phase, the decisive steps for the deposition of PyC are heterogeneous reactions on the substrate such as adsorption, surface reactions and desorption.

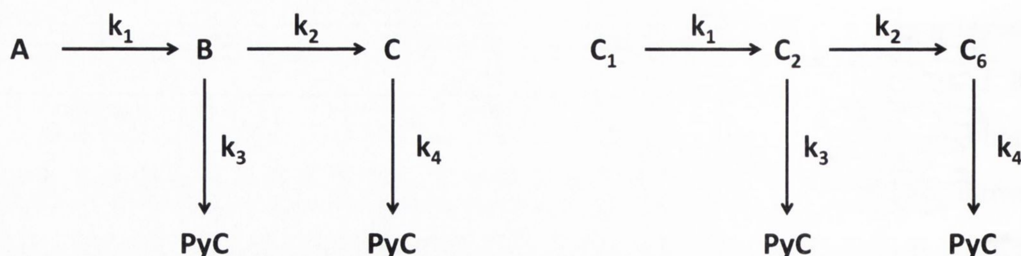

Figure 5 General reaction scheme describing the process of PyC deposition from a hydrocarbon (left) and its corresponding reaction scheme in the case of PyC deposition from methane (right).

PyC possesses good thermal and electrical conductivity in addition to high durability and chemical resistance.[41] Due to its thermal and mechanical properties, it has been widely used as a coating for individual pebbles in pebble bed reactors and rocket nozzles[42] as well as electronic thermal management applications in heat spreaders.[43] PyC has been investigated as a coating for heart valves and other forms of prosthesis because of its biocompatibility.[44,45] It has also been used as a coating for optical fibres making them more resistant to harsh environmental conditions.[46] Recently, owing to its ease of processing and favourable properties, PyC has been suggested as an electrode material for microelectronics applications including vertical interconnects and wires, gate electrodes, Schottky diode devices, liners for trench capacitors in dynamic random-access memory (DRAM), and metal-silicon-insulator (MSI) capacitors.[47-54]

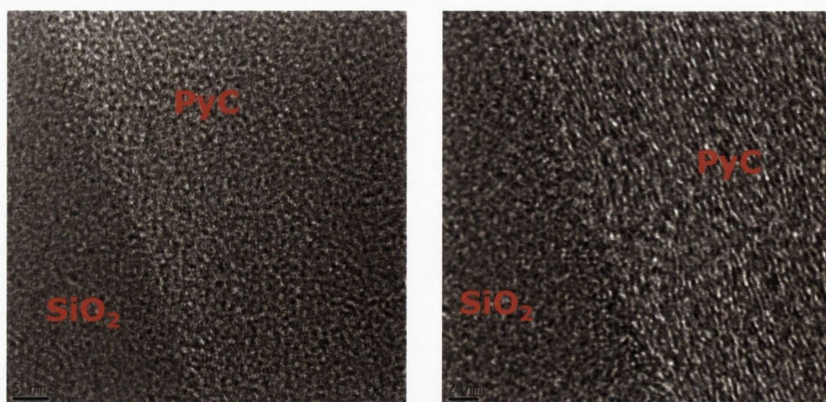

Figure 6 HRTEM images of the interface between PyC and the SiO_2 substrate. (growth condition t = 15 min, P = 20 Torr, T = 950 °C).[41]

Within our group a detailed study of the deposition of PyC films from acetylene and their usage as thin conducting films has been carried out.[41] Images of the interface between PyC and SiO_2 from electron microscopy analysis are shown in Figure 6, which give information on the crystallinity of the PyC grown. A laminar like deposition of the crystallites is observed from the high resolution transmission electron microscopy (HRTEM) images of the cross-sectional interface in Figure 6.

1.1.3 Graphene

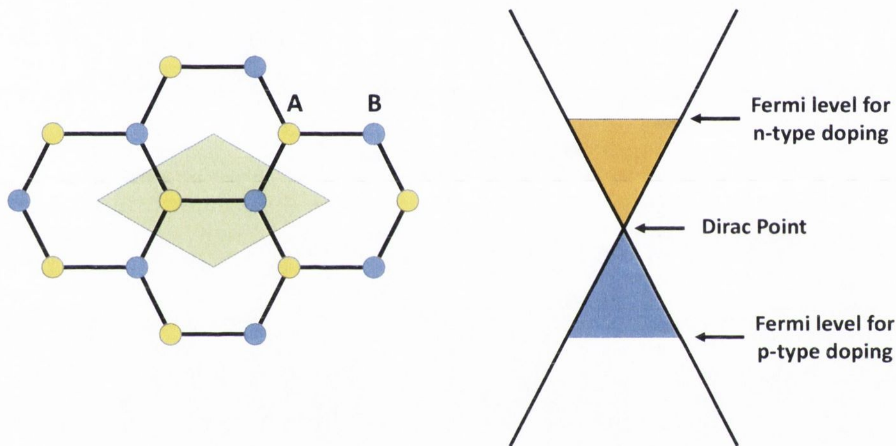

Figure 7 Hexagonal honeycomb lattice of graphene with two atoms (A and B) per unit cell (left), and schematic energy band structure of monolayer graphene where its conduction and valence bands touch each other at the Dirac point (right). Depending on the nature of the doping and the transport carrier, the position of the Fermi level varies.

Graphene is a two-dimensional (2D) crystal consisting of carbon atoms that form an ordered hexagonal network where each carbon atom has covalent bonds with three nearest carbon atoms. As shown in Figure 7, the structure can be explained as a hexagonal honeycomb lattice with two carbon atoms (A and B) per unit cell, leading to a rather unique band structure.[55] Monolayer graphene has its conduction and valence bands touching each other at the corners of the Brillouin Zone, and the touch points are called the Dirac points. Theoretical studies of graphene were first explored in 1940s and 1950s as a starting point for understanding the electronic properties of 3D graphite,[56-58] and ongoing studies of its electronic and magnetic properties were carried

out in the 1980s.[59,60] Ever since its experimental isolation was first demonstrated in 2004, using a relatively simple mechanical exfoliation method using scotch tape, a massive number of experimental studies have been conducted.[11,61]

As predicted by theory, graphene has displayed an array of exciting properties experimentally. It has very high intrinsic mobility (~200,000 cm^2 V^{-1} s^{-1}), a large theoretical specific surface area (2630 m^2 g^{-1}), good thermal conductivity (~5000 W m^{-1} K^{-1}), and a high Young's modulus (~1.0 TPa).[62-65] As all of the atoms in graphene are surface atoms, pristine graphene is likely to be chemically modified through exposure to external molecules. Moreover, its good optical transmittance (~97.7%) and high electrical conductivity suggest it could be used in transparent conductive electrodes,[66,67] and this combined with its flexibility holds promise for transparent flexible electronics. Moreover, its high electrical mobility has allowed graphene to become one of the most promising candidates for future nano-electronics, especially for high speed devices.[68-71] However, recently reported graphene transistors showed inferior performance including poor intrinsic gains and low on-off ratios compared to conventional semiconducting channel devices.[72,73] This is because the semi-metallic nature of monolayer graphene (i.e. zero band gap at Dirac points) causes a relatively high off-state current in graphene channel devices. While a number of routes have been explored to open a band gap in graphene, including spatial confinement of charge carriers,[74-76] use of multilayer graphene,[77-79] and chemical modification like doping or functionalisation of graphene,[80-82] it is still challenging to apply these techniques to the industrial environments for mass production. Nevertheless, graphene-based electronic devices are still believed to be excellent candidates for other applications such as chemical or biological sensors and radio-frequency applications where completely switching off the transistors is not critical.

It is essential to produce high quality graphene for such electronic applications to be realised, and various methods have been suggested. A mechanical exfoliation technique has been frequently used to obtain homogeneous high quality graphene owing to the layered nature of graphite.[12,13] Mechanical exfoliation is a simple peeling process whereby commercially available highly oriented pyrolytic graphite (HOPG) is peeled off layer-by-layer using an adhesive tape like Scotch tape. While mechanical exfoliation can still be considered as the method which produces the highest quality graphene, it is not appropriate for industrial electronic device applications owing to its

low yield and low throughput and the lack of scalability. Chemically exfoliated graphene which can be produced mainly via reduction of graphene oxide is beneficial because of its relatively low cost and possibility of large-scale production.[83-85] However, the quality of graphene obtained by this method is not satisfactory because of inevitable lattice defects generated by the oxidation process, resulting in undesirable disorders and degradation of the electronic properties. In addition, liquid phase exfoliation of graphite has been suggested as a possible method to produce high quality graphene in large quantities,[86,87] which still has some drawbacks like difficulties in controlling the graphene layer number and the lateral size of exfoliated flakes.

Recently, a direct growth method on metallic surfaces such as nickel (Ni) and copper (Cu) using chemical vapour deposition (CVD) has been introduced as an alternative pathway to large-scale graphene synthesis.[88-93] Particularly, CVD-grown graphene on Cu is continuous with uniform thickness over large areas, thus making it promising for electronic applications. Although precise control over its grain size and the number of graphene layers has yet to be fully realised, graphene sheets produced on metallic surfaces generally show a good quality in terms of electronic properties. However, a significant drawback of this method is that it is essential to transfer the as-grown graphene sheets to appropriate substrates for electronic device applications. Several techniques, including the use of a polymer support layer, pressing and stamping with thermal-release tapes, and modification of the surface tension of metal etchant solution, have been suggested for the stable transfer of CVD-grown graphene sheets.[67,91,94-98] Among these, polymer supported transfer is the most commonly used method and has also been demonstrated successfully on a large scale. Moreover, direct synthesis of graphene on insulators or semiconductors has been introduced as a possible solutions to avoid such a graphene transfer process. The most successful and representative example is epitaxial growth of graphene on silicon carbide (SiC) substrates,[99-102] where graphene can be produced by heating single/polycrystalline SiC substrates in vacuum to high temperatures (1200 – 1600 °C). While it is considered to have a high feasibility for the synthesis of wafer-scale uniform graphene layers, the necessity of very strict conditions for the graphene growth such as high temperature, ultrahigh vacuum and the relatively high cost of SiC substrates limits the use of this technique in large-scale practical applications.

1.2 Molybdenum Disulfide

In recent years there has been a large volume of research conducted on layered materials such as graphene and transition metal dichalcogenides (TMDs) due to their suitability for future electronic/optoelectronic device applications.[61,103-105] In particular, molybdenum disulfide (MoS_2), a semiconducting TMD, has drawn a lot of attention owing to its fascinating electronic and optical/optoelectronic properties.[61,106-108] It has been identified as one of the most promising 2D materials for nano-electronic applications because its electrical properties can be tuned by controlling the number of layers or by careful selection of substrate/gate dielectric materials.[106,109-111] Moreover, unlike pristine graphene which has no band gap, monolayer MoS_2 has a direct band gap of ~1.8 eV while bulk MoS_2 has an indirect band gap of ~1.3 eV.[106]

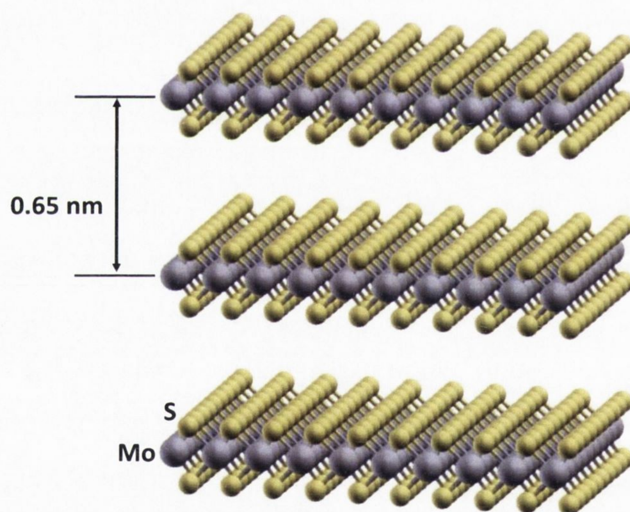

Figure 8 Schematic representation of the crystal structure of bulk MoS_2.

As depicted in Figure 8, the crystal structure of bulk MoS_2 consists of vertically stacked 2D layers composed of an atomic plane of metal atoms (Mo) sandwiched between two planes of chalcogen (S) atoms.[112,113] Within a single S-Mo-S layer, the Mo and S atoms form a 2D hexagonal sublattice with a thickness of ~0.65 nm. There are covalent bonds between the intra-layer atoms, whereas very weak van der Waals bonding exists between layers. Therefore, it can be exfoliated along the layer surface.

Thus far the first electronic devices based on single- or multilayer MoS_2 films have shown good photodetection capability.[110,114] Recent studies on MoS_2 thin film field

effect transistors have shown that the MoS_2 channel has very clear n-type characteristics with high mobility and good current on/off ratios,[109,111,115] which indicate that this layered material could be utilised in integrated circuits and logic circuit applications.[116,117] Furthermore, the ability to tune the optical band gap of MoS_2 by thickness modulation suggests a wide range of applications in optoelectronic devices including phototransistors and photodetectors.[110,114,118,119].

Similar to graphene, a number of studies on the optical and electrical characteristics of MoS_2 have been done using crystals prepared using the micromechanical exfoliation technique,[106,109,110,118] but as in the case of graphene this suffers from low throughput and poor scalability. In order to resolve these problems, another exfoliation method was introduced which is the solvent-based liquid phase exfoliation method. Coleman *et al.* proposed a direct liquid exfoliation technique for MoS_2 and other layered materials,[120] which makes it possible to obtain single and/or a few layers of MoS_2 flakes in large quantities. However, the lateral dimensions of the flakes produced are small and it is still difficult to get single-layer MoS_2 sheets using this method. Besides this, chemical exfoliation methods using lithium ion intercalation have been used as an alternative solution-based exfoliation technique.[121,122] This is known to give high-yield production of single-layer MoS_2, but the flammability of lithium needs a great care during the process and it is a time-consuming, environmentally sensitive process.[123] Additionally, the ion intercalation procedure can cause the structural deformation of the MoS_2 material which can degrade the electronic properties of the pristine single-layer MoS_2 sheets.[122]

Recently, several techniques for the direct growth of MoS_2 films on substrates have been demonstrated in order to obtain continuous large-scale films, whereby different solid precursors such as molybdenum trioxide (MoO_3) and sulfur powders are heated to high temperature for deposition of MoS_2 films. Large-area MoS_2 films can be directly synthesised on insulating substrates via the reaction of vapourised MoO_3 and sulfur powders,[124] or by direct sulfurization of pre-deposited Mo or MoO_3 on insulators.[125,126] Moreover, a two-step thermolysis process, where the precursor ammonium thiomolybdate ($(NH_4)_2MoS_4$) was dip-coated on insulators followed by annealing in argon/hydrogen (Ar/H_2) atmosphere and further annealing in sulfur vapour, was reported for the production of large-area highly crystalline MoS_2 thin films.[127] In spite of the excellent scalability of the direct growth techniques, the reliable production of

large-scale uniform MoS_2 thin films with high crystalline quality and good control over layer numbers has yet to be fully realised using these methods.

MoS_2 thin films used in this study were synthesised using vapour sulfurisation, where Mo layers with various thicknesses were pre-deposited on insulators, followed by the reaction with evaporated sulfur. The reactor consists of a quartz tube with two different heating zones for subliming sulfur powders and sulfurisation of the loaded Mo samples, respectively. Sulfur vapour is transported to the Mo samples using argon gas as carrier during the process.

1.3 Schottky Barrier Diodes

Schottky barrier diodes (SBDs) consisting of a metal-semiconductor contact are one of the simplest devices in modern semiconductor technology. In spite of the fact that Schottky diodes have a simple structure, they are the basis of a large number of compound semiconductor devices such as integrated circuits, high-frequency units, photodiodes, and power diodes.[128,129] There is an increasing demand for high speed and high performance diodes, particularly in mobile communication and power management. The first practical SBDs were used in the early 1900s. This diode, also called a point contact diode, was made by touching a metallic whisker to an exposed semiconductor surface. These metal-semiconductor diodes were not very reproducible or mechanically reliable and were replaced by the p-n junction in the 1950s. However, nowadays semiconductor and vacuum technology is much more advanced and able to fabricate reproducible and reliable metal-semiconductor contacts.[130]
The Schottky barrier diode is formed by a metal contact to a semiconductor, instead of the more common junction between p- and n-type semiconductors. Schottky diodes differ from p-n junction devices in that rectification occurs because of a difference in work function between the metal contact and the semiconductor, rather than a non-uniform doping profile. The work function is the difference between the Fermi level (E_F) for each material and the free-space energy level (vacuum level). For a particular metal and n-type semiconductor contact, a Schottky barrier is formed when the work function of the metal is larger than that of the n-type semiconductor. Conduction is not controlled by minority carrier recombination in the semiconductor, but by thermionic emission of majority carriers over the barrier created by the unequal work functions. The Schottky diode is, therefore, a majority carrier device whose switching speed is not limited by minority carrier effects. Many metals can create Schottky barriers with semiconductors. In commercial products semiconductors such as silicon or gallium arsenide (GaAs) are commonly used in combination with metals like platinum, titanium or gold.[131]

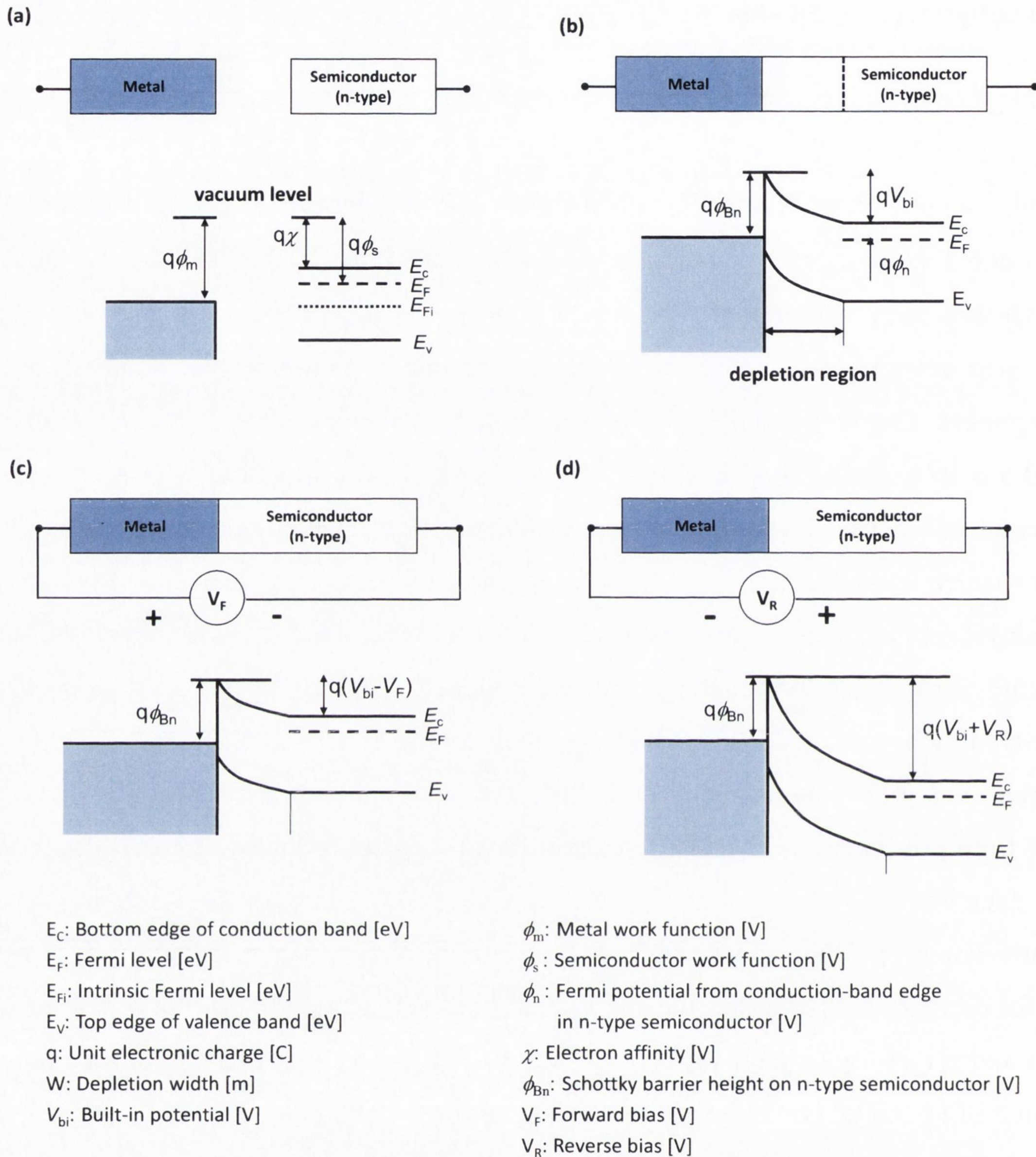

Figure 9 Energy band structure of the metal and semiconductor (a) before contact, (b) after contact, (c) under forward bias (V_F) and (d) reverse bias (V_R).

Figure 9 shows the energy band diagrams of a metal and an n-type semiconductor. The work function is the average energy required to remove an electron from the material. The electron affinity is the energy required to detach an electron from the singly charged negative ion, which is a constant for each material, and must remain constant throughout it. However, the Fermi level of the semiconductor, and hence its work function, can be expected to vary with doping density. When the metal and semiconductor are in equilibrium and are not in contact (in Figure 9(a)), the energy

levels are constant throughout the materials. The Fermi levels are generally unequal, indicating that the electrons in one material (in this case, the metal) have less energy on average than those in the semiconductor. Therefore, when the materials are brought into contact, some of the electrons move from the semiconductor spontaneously into the metal and they are aggregated with electrons in the metal on the surface. These leave behind ionised donor locations, which are positively charged, and create a negative surface charge in the metal. An electric field is set up between these positive charges and the electrons that eventually inhibit further electron flow into the metal. The positively charged region is called the depletion region, since it is almost completely depleted of mobile electrons. The shape of the energy diagram of the metal - semiconductor junction is governed by three rules: (1) at equilibrium, the Fermi levels for the semiconductor and metal must be constant throughout the system, (2) the electron affinity must be constant, and (3) the free space energy level must be continuous.

Figure 9(b) shows the resulting band structure when the metal and semiconductor are joined. In order to satisfy all three rules simultaneously, the valence and conduction bands of the semiconductor are forced to bend at the junction; the upward bend of the conduction band of the n-type semiconductor indicates the depletion region. The resulting potential difference (V_{bi}) across this region, as shown in the figure, is simply the difference between the work function, $V_{bi} = \varphi_m - \varphi_s$. This is called the built-in potential of the junction. Figure 9(c) and (d) show a biased Schottky junction. Since a bias voltage is applied, the junction is no longer in equilibrium, and the requirement that the Fermi levels should be constant throughout the diode no longer applies. Instead, the Fermi levels, which are called quasi-Fermi levels for the non-equilibrium case, move with applied voltage. The offset from their equilibrium position is simply equal to qV, where V is the applied voltage. The voltage across the junction then is $V_{bi} - V$, where V is defined as forward or reverse bias depending on its polarity across the junction. If a positive voltage is applied to the metal with respect to the semiconductor (forward bias, V_F), the semiconductor-to-metal barrier V_{bi} is reduced while φ_m remains constant in this idealised case. In this situation, electrons can more easily flow from the semiconductor into the metal since the barrier has been reduced. This bias condition is the forward bias. If one applies a positive voltage to the semiconductor with respect to the metal (reverse bias, V_R), the semiconductor-to-metal barrier height increases while

φ_m again remains essentially constant. This bias condition is the reverse bias. Electron affinity values of some semiconductors and work functions of some metal elements are listed in Table 1 and Table 2.

Table 1 Electron affinity of some semiconductors.[130]

Element	Electron affinity, $q\chi$ [eV]
Ge, germanium	4.13
Si, silicon	4.01
GaAs, gallium arsenide	4.07
AlAs, aluminium arsenide	3.5

Table 2 Work functions of some metal elements.[130]

Element	Work function, $q\phi_m$ [eV]	Element	Work function, $q\phi_m$ [eV]
Ag, silver	4.26	Ni, nickel	5.15
Al, aluminium	4.28	Pd, palladium	5.12
Au, gold	5.1	Pt, platinum	5.65
Cr, chromium	4.5	Ti, titanium	4.33
Mo, molybdenum	4.6	W, tungsten	4.55

In general, the performance of the SBDs can be described by the ideality factor which is a value of how closely the diode follows ideal diode behaviour on a logarithmic scale and has a value of 1 in the ideal case. Typical diodes have ideality factors between 1 and 2, and in commercial products values between 1.05 and 1.2 are generally used. In general, the stability of the interface between the metal and semiconductor is one of the most critical conditions in diode performance.

1.4 Photodiodes

Photoelectric detectors are electronic devices which measure photon flux or optical power by converting the energy of absorbed photons (optical signals) into electrical signals.[132] A photodiode (or junction photodiode) is one of the most frequently used photoelectric detectors in the photonics industry. Photoelectric detectors operate on the basis of the photoelectric effect (also called the photoeffect) where a photon is converted into an emitted electron or an electron-hole pair. The former is called the external photoeffect which involves photoelectric emissions and the latter is called the internal photoeffect which involves photoconductivity.[133] Most modern photoelectric detectors are based on the internal photoeffect, in which the photoexcited electron-hole pairs change the electrical conductivity of a material. For example, when a photon is absorbed in an intrinsic semiconductor and it has a higher energy than the band gap (E_g), a free electron which is excited from the valence band (E_v) to the conduction band (E_c) can be generated and the associated hole is generated in the valence band (see Figure 10). If an electric field is applied to the material, it will induce the transport of the photo-generated electron and hole, producing a current flow in the electrical circuit.

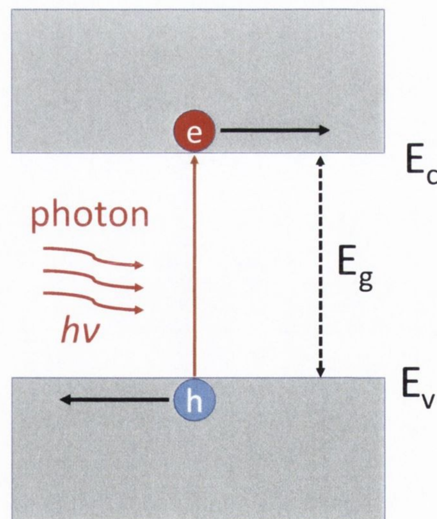

Figure 10 **Electron-hole photo-generation in a semiconductor.**

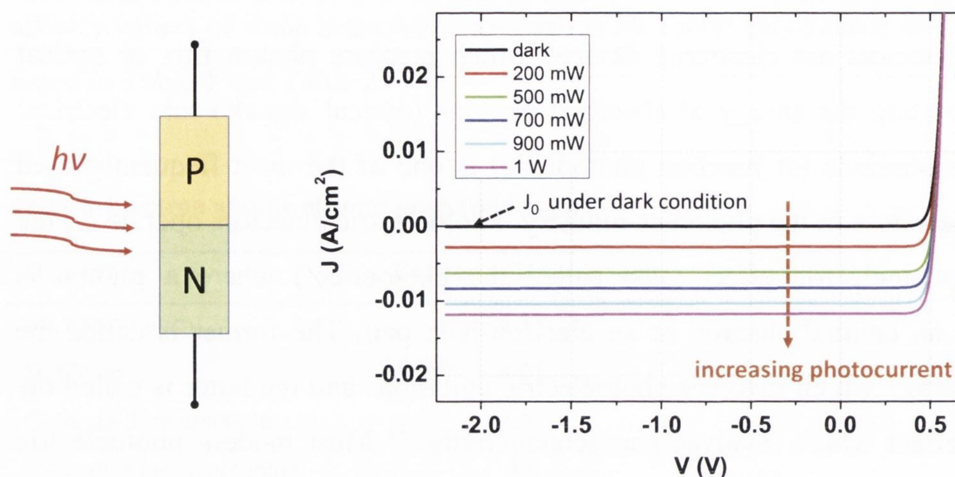

Figure 11 Plot of current-voltage measurements for a commercial silicon photodiode (BPW21, OSRAM) under different incident light power.

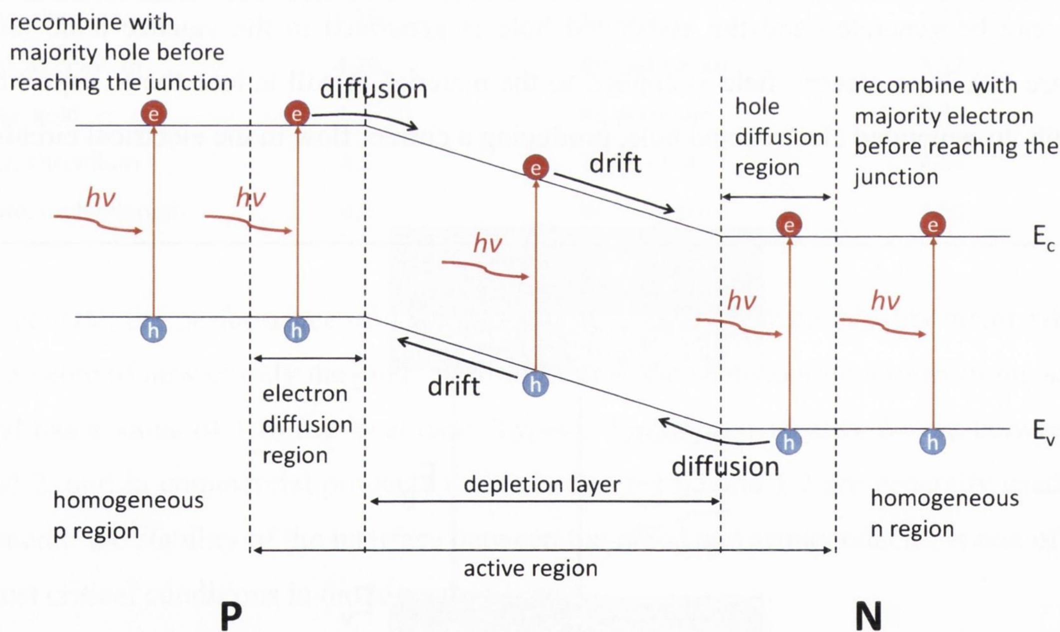

Figure 12 Cross sectional view of the p-n semiconductor diode structure and its energy band diagram under illumination.

A semiconductor photodiode is also based on the internal photoeffect. A plot of current-voltage measurements for a silicon photodiode (BPW21, OSRAM) is depicted in Figure 11. It has a p-n junction structure and its reverse current increases when the incident light power increases because more photons are absorbed in the photodiode at

higher incident light power. A cross sectional view of the p-n semiconductor diode structure and its energy band diagram under illumination are shown in Figure 12. There is a depletion layer at the junction where electrons and/or holes have completely diffused away in thermal equilibrium and only ionised donors and acceptors are left, forming an energy barrier called a built-in potential. If the incident photons have an energy greater than the band gap of the semiconductors, the valence band electrons are excited to the conduction band, generating electron-hole pairs. In a semiconductor photodiode, electron-hole pairs can be generated in three possible locations which are the depletion layer, the diffusion regions and homogeneous regions. In the depletion layer, the excited electrons and holes are accelerated to the n-type and the p-type area, respectively, under the influence of the strong electric field, producing a drift current. The direction of current flow induced from the external photon energy always has the opposite direction to the original p-n diode circuit. If electron-hole pairs are generated within one of the diffusion regions at the edges of the depletion layer, they have a probability of entering the depletion layer by random diffusion. In this case, the minority carrier (electrons in p-type area and holes in n-type area) can be diffused up to the depletion layer. Once they reach the depletion layer, they are quickly transported across the junction, resulting in photocurrent to the external circuit. The current flow from the diffusion also has the reverse direction. Electron-hole pairs generated away from the depletion layer (p- or n-type homogeneous region) by absorption of photons cannot contribute to the generation of photocurrent since an internal electric field, which is necessary to separate the charges, does not exist and they cannot diffuse to the depletion layer before recombining with majority carrier.

Since the response of a photodetector depends on the wavelength of the incident light, a photodetector selectively responds to a finite, specific range of the optical spectrum. The material, the structure, and the packaging of the detector are the main factors which determine the spectral range of response for a photodetector. The spectral response of a photodetector is usually specified in terms of the spectral responsivity of the detector. Responsivity is one of the important parameters commonly used to define the performance of photodetectors, which allows one to resolve the available output signal of a detector for an input optical signal. In general, the responsivity is defined as the ratio of the output current to the incident light power (the input optical signal) and the

responsivity, R, can be expressed as $R = I_S/P_S$ with a unit of ampere per watt (AW^{-1}), where I_S is the output current and P_S is the incident light power.

1.5 Outline of Thesis

In this thesis hybrid electrical devices such as Schottky barrier diodes (SBDs) and photodiodes have been fabricated using three different conductive carbon or semiconducting transition metal dichalcogenide (TMD) thin films. The characteristics of each film and electrical properties of the devices are rigorously analysed using various measurement techniques.

In the first chapter, a brief introduction of the materials used in this study is given. In the second chapter, basic principles and theory of the device operation, and experimental techniques employed to characterise the devices are presented.

In the third chapter, Schottky contacts between conductive carbon thin films and silicon are characterised. Electrical characteristics of the carbon-silicon SBDs are investigated and diode device parameters such as Schottky barrier height, the ideality factor, and series resistance are extracted from dc current-voltage measurements. In addition, impedance spectroscopy (IS) is employed in order to investigate the properties of the Schottky contacts of the devices. From analysis of the IS data, the effects of the metal electrode contacts of SBDs as well as the built-in potential and more reliable barrier height values can be revealed.

In the fourth chapter, p-n heterojunction photodiodes are investigated. The photodiodes are composed of a thin n-type MoS_2 layer transferred onto p-type silicon. The p-n heterojunction diodes show good photoconductivity which can be modulated by changing the thickness of the MoS_2 layer. The diodes have a broad spectral response due to direct and indirect band transitions of the nanoscale MoS_2.

In the appendix, the results of comprehensive SE characterisation of the vapour phase sulfurised MoS_2 films are described in detail. Analysing the SE spectra measured from MoS_2 thin films, an optical dispersion model of the MoS_2 thin film has been developed, which gives values of optical constants such as the extinction coefficient and refractive index, as well as the thickness of MoS_2 films. Moreover, the optical band gap values of the MoS_2 layers with different thicknesses are extracted from SE, showing a clear dependence on the MoS_2 film thickness.

2. Experimental Methods

2.1 Chemical Vapour Deposition

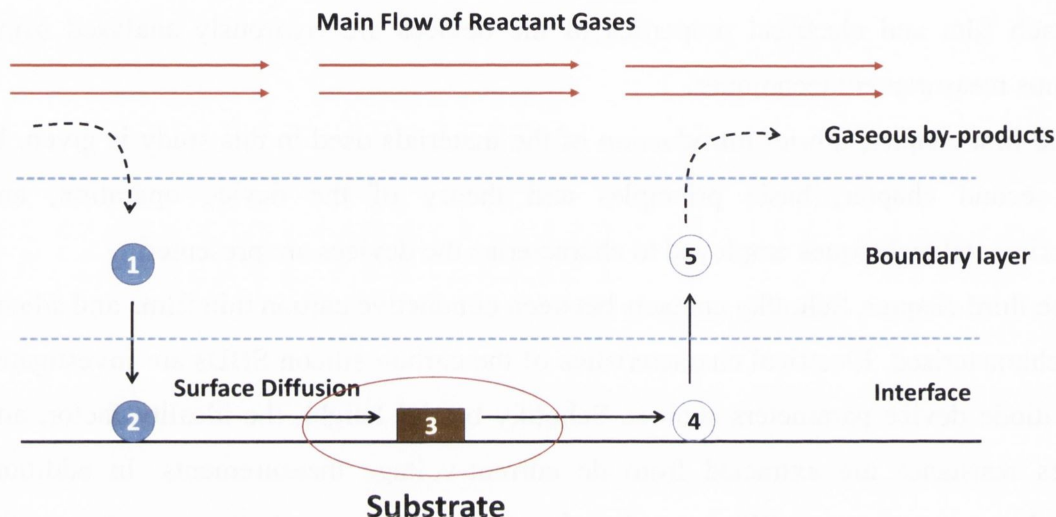

Figure 13 CVD mechanism; (1) diffusion of reactant to surface, (2) absorption of reactant to surface, (3) chemical reaction, (4) desorption of by-product gas, (5) out-diffusion of by-product gas.

The PyC films and graphene studied in this work were grown using chemical vapour deposition (CVD). CVD is a generic name for a group of processes that involve depositing a solid material from a gaseous phase. The benefits of CVD typically include uniformity (thickness, density), purity, control over composition and stoichiometry, structural composition, excellent adhesion, conformality, low defects and low cost.[134] The versatility of CVD has allowed it to be used in wide ranging areas, and a number of variants of CVD exist including atmospheric pressure CVD, low pressure CVD, metal-organic CVD, plasma assisted or enhanced CVD, and laser CVD. In a typical CVD process, precursor gases are delivered into the reaction chamber at approximately ambient temperatures. As they pass over and come into contact with a heated substrate, they react or decompose forming a solid phase and are deposited onto the substrate. The substrate temperature is critical and can influence what reactions will take place.[134] The CVD mechanism is depicted schematically in Figure 13. CVD coatings are usually only a few microns thick and are generally deposited at rates of the order of a few hundred microns per hour.

In this work, self-built tube furnaces (Gero GmbH and Carbolite) were used as a source of heat for the CVD process. The furnace was equipped with a quartz tube and mass flow controllers (MFC) which allowed for precise adjustment of gas flows into the furnace. Moreover, the furnace had a temperature set point programmer to enable diverse controllable heating/dwelling programmes. The PyC used in this study was grown in a Gero quartz tube furnace using acetylene (C_2H_2) as the hydrocarbon feedstock at a flow rate of 180 sccm and a pressure of 20 Torr. The growth temperature was 950 °C and the growth time was 5 minutes, giving a film of ~70 nm thickness. The graphene was grown on Cu foils in a Carbolite quartz tube furnace. The growth temperature was 1035 °C, and high purity methane (CH_4) was used as the hydrocarbon precursor with a supply of hydrogen.

2.2 Pyrolysis of Photoresist Films

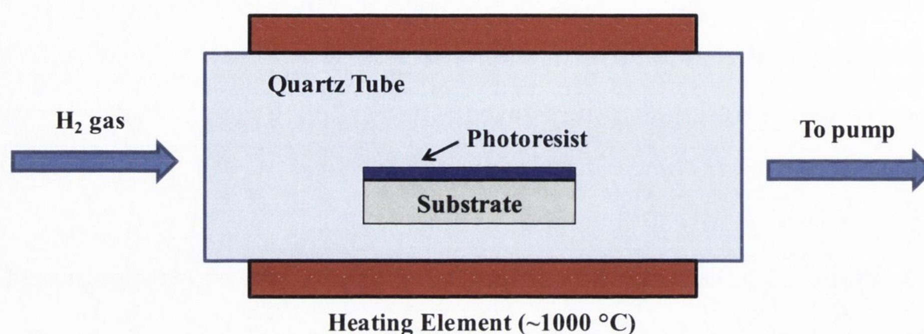

Figure 14 **A schematic of the furnace system used for pyrolysis.**

PPFs are produced by pyrolysing photoresist films at high temperature usually in a reducing hydrogen gas flow. The photoresist films were spun on substrates. The samples were then pyrolysed in a quartz tube furnace at high temperature (~1000 °C), as shown in Figure 14. The reaction chamber is connected at one end to a supply of gases via control valves and at the other to the pump for disposal of gas. The temperature increases up to 1000 °C with a ramp rate of 850 °C per hour and samples are pyrolysed for 1 hour at 1000 °C. Hydrogen gas (10 sccm) flows into the chamber during the pyrolysis process to assist the polymer decomposition. As previously explained, some film shrinkage occurs during pyrolysing, primarily in the film thickness, due to decomposition of the photoresist. Table 3 lists the thickness values for different photoresists before and after pyrolysing.[28]

Table 3 Summary of resist thickness before and after pyrolysing.[28]

Resist	Thickness before pyrolysis [nm]	Thickness after pyrolysis [nm]
nLof AZ 2070 (negative tone photoresist)	518	148
nLof AZ 2070 (diluted)	35	7
nLof AZ 4533 (positive tone resist)	4026	690
ma N 20401 (negative tone resist)	344	30

2.3 Electron Microscopy

Electron microscopy is a powerful tool for characterising samples at the nanoscale. Unlike an optical microscope which uses a light source to create an image of a specimen, it uses a beam of electrons. It is capable of much higher magnifications and has a greater resolving power than an optical microscope, allowing it to see much smaller objects in fine detail.

The resolving power of a microscope is directly related to the wavelength of the irradiation used to form an image. Reducing the wavelength increases the resolution. Therefore, the resolution of the microscope is increased if the accelerating voltage of the electron beam is increased. The faster the electrons travel, the shorter their wavelength.

All electron microscopes use electromagnetic and/or electrostatic lenses to control the path of electrons.[135] The electron beam passes through the centre of such electrostatic lenses on its way down the electron microscope towards the sample. Electrons are very sensitive to magnetic fields and can therefore be controlled by changing the current through the lenses.

The transmission electron microscope (TEM) and scanning electron microscope (SEM) are the two most generally used tools in electron microscopy. Schematic diagrams of TEM and SEM are shown in Figure 15. In TEM the electron beam that has been partially transmitted through the very thin specimen carries information about the structure of the specimen.[135] The spatial variation in this information is then magnified by a series of magnetic lenses until it is recorded by hitting a fluorescent screen or light sensitive sensor such as a charge-coupled device (CCD) camera. The image detected by the CCD is a two-dimensional black and white image, and is displayed in real time on a monitor or computer. Unlike the TEM, where electrons in the primary beam are transmitted through the sample, a SEM produces images by detecting secondary electrons which are emitted from the surface due to excitation by the primary electron beam or backscattered electrons. In the SEM, the electron beam is scanned across the surface of the sample in a raster pattern, with detectors building up an image by mapping the detected signals in relation to the beam position.[135] In general, the TEM has an order of magnitude better resolution than the SEM while its sample preparation and imaging process are rather difficult compared to the SEM.

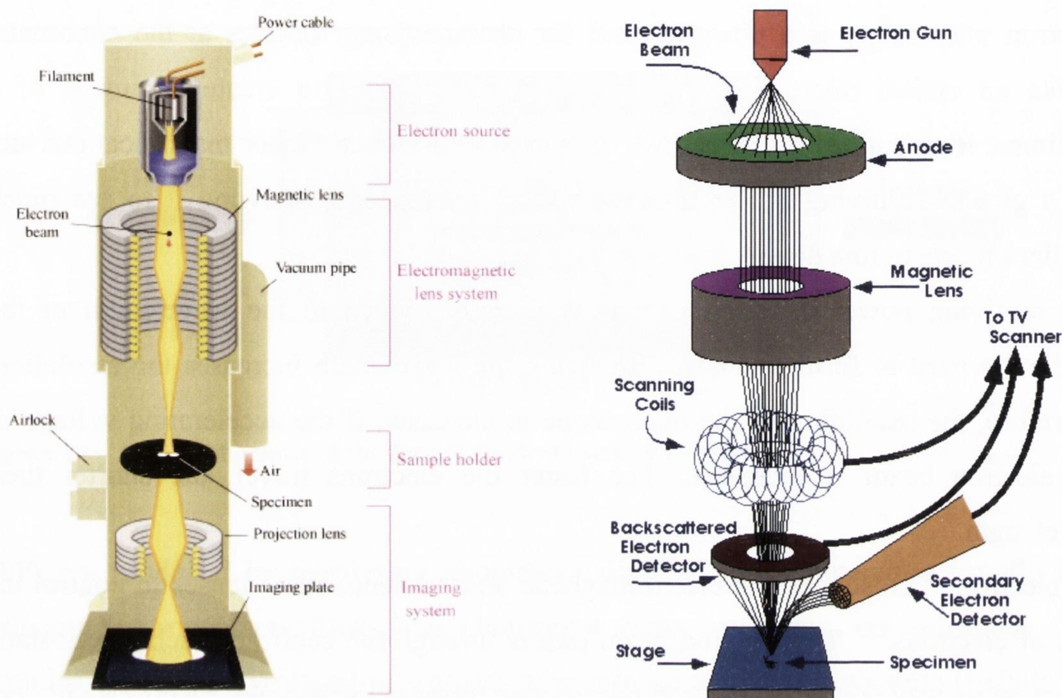

Figure 15 **The Schematic outline of TEM (left)[136] and SEM (right).[137]**

In this work, SEM and high resolution transmission electron microscopy (HRTEM) studies were performed on cross sections of carbon thin films and carbon-silicon interfaces. SEM images were acquired with a Zeiss Ultra FE-SEM at an acceleration voltage of 5 kV. For HRTEM analysis, samples were prepared in a Zeiss Auriga Focused Ion Beam (FIB) with a Cobra ion column. A reactive gas injection system was used for reactive ion etching and deposition of a Pt capping layer. The cross sections were imaged at 300 kV using an FEI Titan 80-300 (S) TEM equipped with a S-TWIN objective lens and a high brightness (X-FEG) Schottky field emission gun with a monochromator.

2.4 Raman Spectroscopy

Raman spectroscopy provides information about molecular vibrations that can be used for sample identification and quantitation. The technique involves shining a monochromatic light source (*i.e.* laser) on a sample and detecting the scattered light. The majority of the scattered light is of the same frequency as the excitation source; this is known as Rayleigh or elastic scattering. A very small amount of the scattered light (~10^{-3} % of the incident light intensity) is shifted in energy from the laser frequency due to interactions between the incident electromagnetic waves and the vibrational energy levels of the molecules in the sample. The process leading to this inelastic scattering is termed the Raman Effect. Raman scattering can occur with a change in vibrational, rotational or electronic energy of a molecule. Plotting the intensity of this shifted light versus frequency, typically expressed in reciprocal cm (cm^{-1}), results in a Raman spectrum of the sample.

Raman spectroscopy is particularly well suited to molecular morphology characterisation of carbon materials.[138] Every band in the Raman spectrum corresponds directly to a specific vibrational frequency of a bond within the molecule. As shown in Figure 16, the most prominent features in the Raman spectra of defective graphitic materials are the so-called G band appearing at 1582 cm^{-1} (graphite), the D band at about 1350 cm^{-1}, the D′ band at about 1620 cm^{-1} and the 2D band at about 2700 cm^{-1}.[139] The G band arises from the in-plane stretching of the C-C bond in graphitic materials, and is common to all sp^2 carbon systems. In contrast, sp^3 and sp carbon networks show characteristic Raman features at 1333 cm^{-1} and in the range 1850 – 2100 cm^{-1}, respectively. The D and D′ bands are defect-induced Raman features, and thus these bands are absent for highly crystalline graphite. The integrated intensity ratio I_D/I_G for the D band and G band is widely used for characterising the defect quantity in graphitic materials.[140]

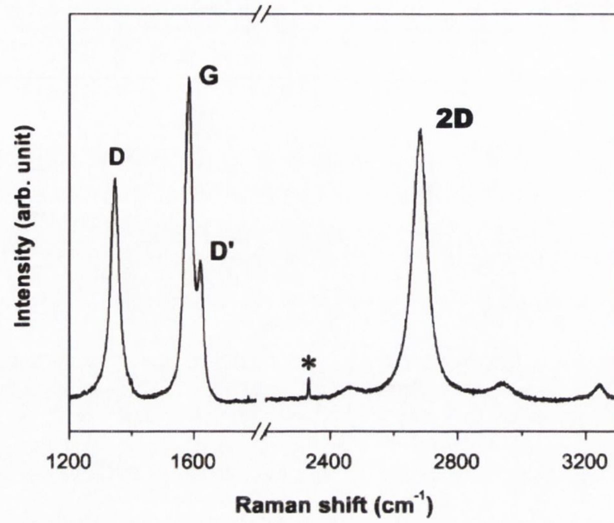

Figure 16 Raman spectrum of a nano-graphite sample taken with a laser excitation energy (wavelength) of 2.41 eV (514.5 nm).[139]

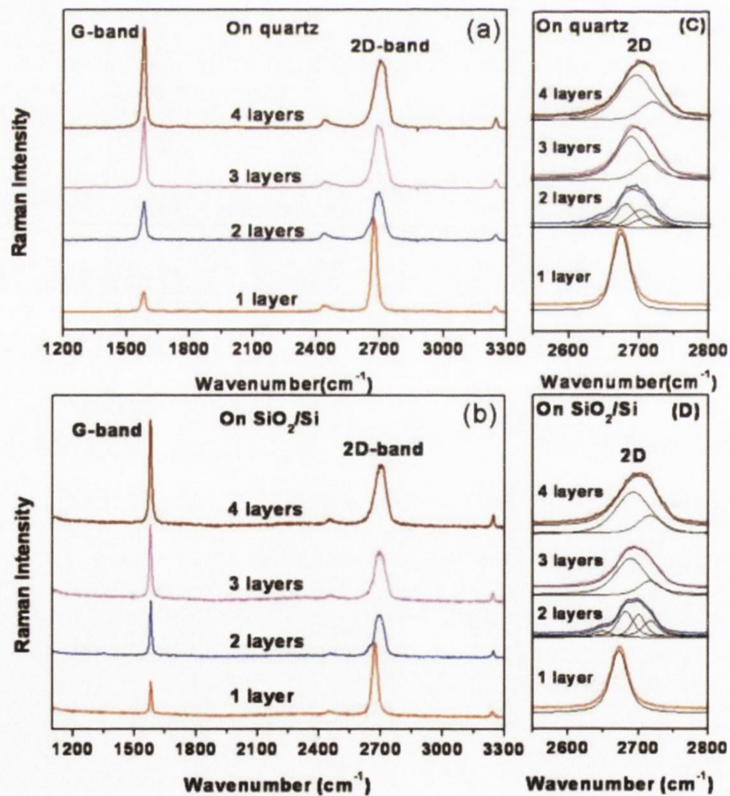

Figure 17 Raman spectra of monolayer, bilayer, three layers, and four layers graphene on (a) quartz and (b) SiO_2/Si substrate. The enlarged 2D-band regions with curve fit are also shown in panels (c) and (d).[141]

The 2D band appears for all kinds of sp^2 carbon materials, so combined with the G-band, this spectrum is a Raman signature of graphitic sp^2 materials. The 2D band can be used to determine the number of layer of graphene since the 2D band in the single-layer graphene is much more intense and sharper than the 2D band in multi-layer graphene,[139,141,142] as shown in Figure 17.

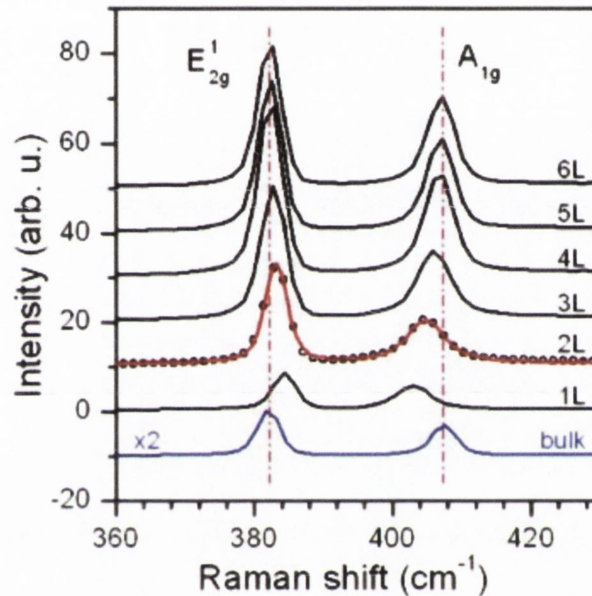

Figure 18 **Raman spectra of bulk, single-, and few-layer MoS_2 films.**[25]

Raman spectroscopy is also an important tool for the characterisation of TMDs. It has been typically used to determine crystal quality and identify the layer number of MoS_2 sheets.[25,143] The E^1_{2g} mode is related to the in-plane vibration where the opposite vibration of two S atoms with respect to the Mo between them, and the A_{1g} mode is related to the out-of-plane vibration of only S atoms in opposite directions.[144] It has been reported that E^1_{2g}, and A_{1g}, peaks are strongly dependent on the thickness, or number of layers, in the MoS_2 sample being probed.[25,143] Figure 18 shows representative Raman spectra for bulk, single- and few-layer MoS_2 samples obtained using 514.5 nm laser source, where the frequency of the E^1_{2g} peak decreases (red-shifted) and the frequency of the A_{1g} peak increases (blue-shifted) with increasing layer number. For films of four or more layers, the frequencies of both modes tend to the bulk values. This is because with increasing layer number the interlayer van der Waals forces in MoS_2 limits atomic vibrations, causing the A_{1g} peak to be blue-shifted. On the

other hand, when the layer number increases the effect of the long-range interlayer Coulombic interaction between molybdenum atoms become dominant, resulting in a red-shift of the E^1_{2g} peak.[25]

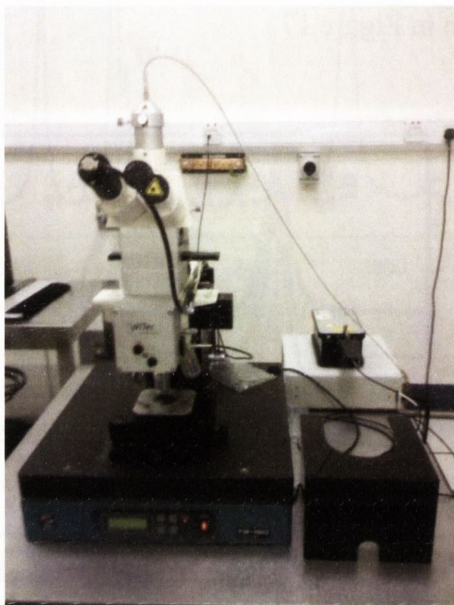

Figure 19 **Photograph of a Witec Alpha 300R confocal Raman microscope.**

In this work, Raman spectroscopy was carried out using a Witec Alpha 300R confocal Raman microscope with an excitation wavelength of 532 nm (Figure 19). In the Raman spectral imaging mode, a complete Raman spectrum is acquired at each image pixel and the images are calculated by isolating spectral characteristics (height, width, peak position, etc.) of these Raman spectra. In typical experiments, the acquisition time for a single Raman spectrum was 50 milliseconds and this results in complete images consisting of tens of thousands of spectra being collected within a few minutes at a spatial resolution of down to ~250 nm.

2.5 Spectroscopic Ellipsometry

Ellipsometry is an optical measurement technique that characterises light reflection (or transmission) from samples and it is a sensitive technique for determining the properties of surfaces and thin films. The key feature of ellipsometry is that it measures the change in polarised light upon reflection from a sample (or light transmission through a sample). The name 'ellipsometry' comes from the fact that polarised light often becomes 'elliptical' upon light reflection.[145]

Ellipsometry measures the two values, Ψ (psi) and Δ (delta). These represent the amplitude ratio Ψ and phase difference Δ between light waves known as p- and s-polarised light waves. A schematic of the interaction of polarised light with a sample in the ellipsometry system is depicted in Figure 20.[146] If linearly polarised light of a known orientation is reflected at oblique incidence from a surface, then the reflected light is elliptically polarised. The shape and orientation of the ellipse depend on the angle of incidence which is the direction of the polarisation of the incident light, and the reflection properties of the surface. One can measure the polarisation of the reflected light from the surface. Then the relative phase change (Δ) and the relative amplitude change (Ψ) between the incident light and reflected light can be calculated. If the sample undergoes a change, for example a thin film on the surface changes its thickness, then its reflection properties will also change. Measuring these changes in the reflection properties can allow us to deduce the actual change in the film's thickness. With this information, one can calculate optical constants (refractive index n, extinction coefficient k), thin film thickness, surface roughness, crystallinity, etc..

One of the most important applications of ellipsometry is thin film characterisation. In the context of ellipsometry, a thin film is one that ranges from essentially zero thickness to several hundred nanometres, although this range can be extended in some cases. The sensitivity of an ellipsometer is such that a change in film thickness of a few angstroms is usually easy to detect. Moreover, the ellipsometer is a very strong tool for thin film studies, which has several advantages including its non-destructive character, high sensitivity due to the measurement of the phase of the reflected light, its large measurement range which is from ~0.1 nm to ~10 µm, and the possibility to control complex processes in real time.

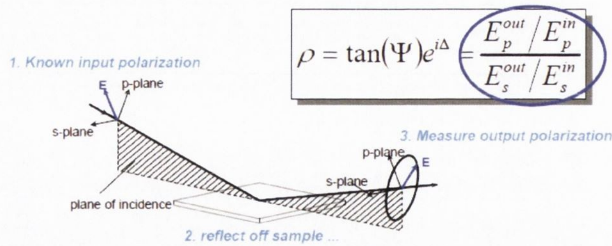

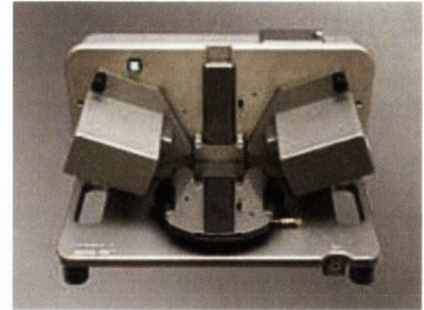

Figure 20 Interaction of polarised light with a sample in the ellipsometry system (left)[146] and photograph of Alpha SE (J. A. Woollam Co.) measurement system (right).

There are two types of ellipsometry; single wavelength ellipsometry (SWE) which measures spectra at single wavelength, and spectroscopic ellipsometry (SE) which measures spectra by changing the wavelength of light. In general, spectroscopic ellipsometry measurement is carried out in the ultraviolet and visible regions, but measurement in the infrared region has also been performed widely. SE can analyse complex structures such as multilayers, interface roughness, inhomogeneous layers, anisotropic layers and much more.

In this work, the Alpha SE model of J. A. Woollam Company (Figure 20) was used to characterise the optical constants, such as the refractive index and the extinction coefficient, of various thin films. The Alpha SE has a spectral range of 380 nm to 900 nm and three angle of incidence options (65 °, 70 ° and 75 °) are supported. The radius of the SE beam spot is the ~4 mm. It is equipped with rotating compensator technology with CCD detection and an automated sample height adjustment system.

2.6 Electrical Measurement

The electrical conductivity of carbon thin films can be investigated by measuring the sheet resistance value. In general, the four-point probe can be used to measure the sheet resistance of thin films or the bulk resistivity of bare wafers. A schematic representation of the four-point probe technique is shown in Figure 21. The theory behind this is a fixed current is injected into the wafer through the two outer probes, and a voltage is measured between the two inner probes.[147]

If probes with uniform spacing s are placed on an infinite flat material, then the resistivity, ρ, is given by $\rho = 2\pi sV/I$ for $t >> s$, and $\rho = (\pi t/\ln 2)V/I$ for $s >> t$, with t representing the thickness of the thin film. For thin film layers, the above equation gives the sheet resistance (R) as $R = \rho/t = (\pi/\ln 2)V/I = 4.53(V/I)$ for $s >> t$. In this work, the sheet resistance of carbon thin films was measured using a four-point probe head (Jandel) connected to a Keithley 2400 source meter unit (SMU).

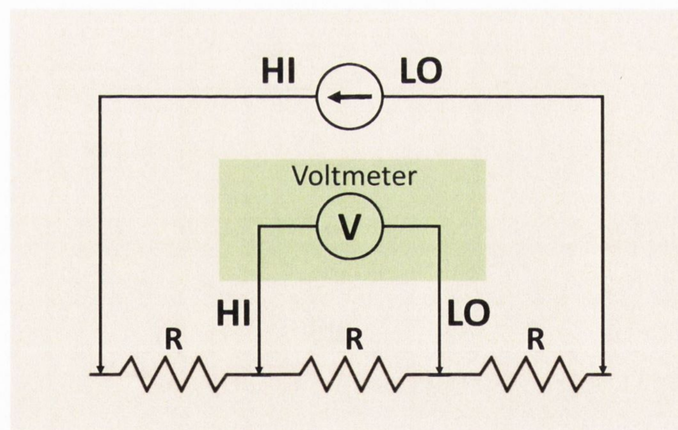

Figure 21 Four-point probe method of measuring resistivity.

In addition, a two-terminal electrical measurement system was set up with a needle probe station connected to Keithley 2400/2612A SMU for the electrical characterisation of devices. The system used home-made Labview software to gather measurement data. The voltage was applied between two metal electrodes of devices through the needle probes and swept in a certain range. The corresponding current values were plotted and gathered automatically using the Labview software. An image of the electrical measurement system and a schematic of the operation principle for

two-terminal needle probe measurement for electrical characterisation of a carbon-silicon SBD are shown in Figure 22.

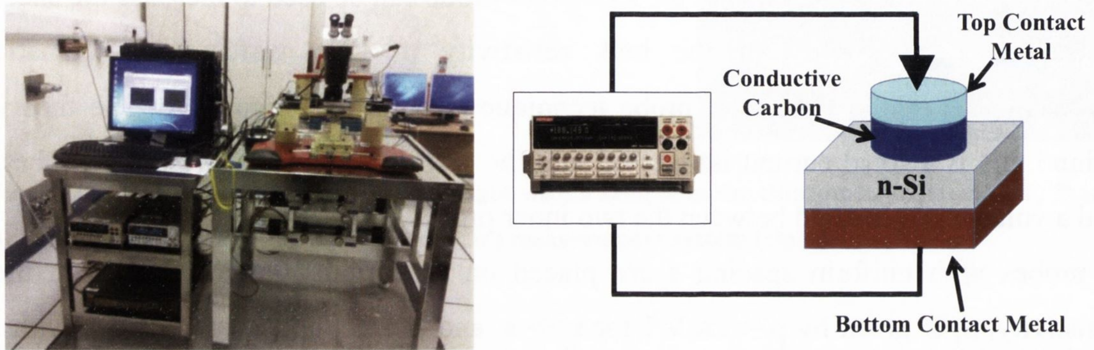

Figure 22 Image of the probe station connected with a Keithley 2400 SMU (left) and schematic of operation principle for two-terminal needle prober for electrical characterisation of carbon-silicon SBD (right).

2.7 Impedance Spectroscopy

Impedance Spectroscopy (IS) is a powerful technique for understanding electrochemical systems and it can be used to study the dynamics of bound or mobile charge in the bulk or interfacial regions of many kinds of solid or liquid materials.[148] In recent years, IS has been applied to investigate the electrical characteristics and conduction mechanism of various organic and inorganic semiconductor devices such as organic light-emitting diodes, organic thin film transistors and solar cells.[149-155]
IS measures the response of a system to a small amplitude sinusoidal signal applied at a constant dc bias and the measurements are conducted at a varying frequency range. Figure 23, which is a current-voltage plot of a diode, gives a general idea of the IS measurements.

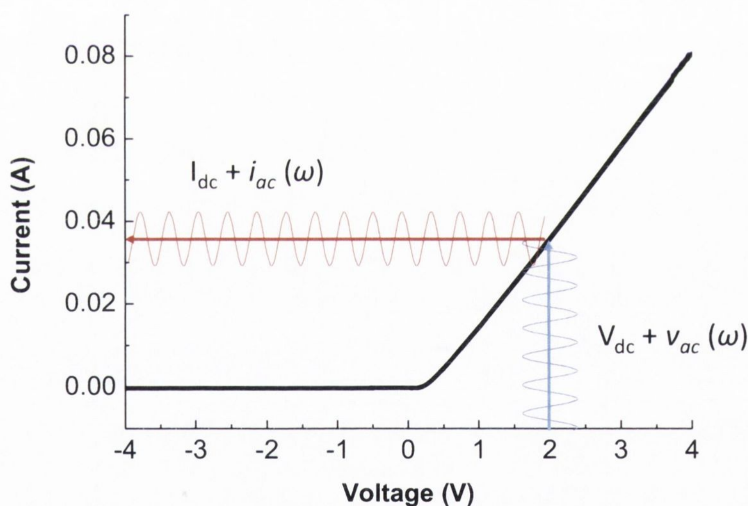

Figure 23 Current-voltage plot measured from a diode, giving a general idea of IS measurements.

IS data are often interpreted by using electrical equivalent circuit models and they can be quantified by analysing the system response, giving information about the interface and its structure. The main advantages of the IS technique are its non-destructive nature and rapid and/or easy measurement methods. On the other hand, the interpretation of the measured data and development of a proper electrical equivalent circuit model, which can well represent characteristics of the system, can prove to be challenging.

When a small amplitude alternating voltage signal, normally a sinusoidal potential excitation, is applied to the system, the response to this signal is an ac current signal, containing the excitation frequency and its harmonics. Using complex notation, the input ac signal which is expressed as a function of time (t) has the form of $v(t) = v_0 \sin(\omega t)$, where $v(t)$ is the potential at a certain time, v_0 is the amplitude of the signal, and ω is the radial frequency ($\omega = 2\pi f$, f is frequency in Hertz.). In a linear system, the response signal, the current $i(t)$, can be expressed as $i(t) = i_0 \sin(\omega t - \theta)$, where θ is the phase difference between the input voltage and output current and i_0 is the amplitude of the output current. If there is only a pure ideal resistive (R) element in the system, θ is zero. However, in a real world situation, there are additional elements such as capacitive (C) and inductive (L) in a system, and the response of such elements is given as $i(t) = [dv(t)/dt] \times C$ for a capacitive element and $v(t) = [di(t)/dt] \times L$ for an inductive element. Since it is quite complicated to find a solution to the differential equations in the time domain for a system, Fourier transformation is generally used to simplify the mathematical calculation. Applying Fourier transformation, the above differential equations become $V = I/(j\omega C)$ and $V = (j\omega L) \times I$ in the frequency domain, and both I and V are functions of ω, given by Fourier transformation of $i(t)$ and $v(t)$. Then, the current-voltage relations in the frequency domain can be considered to follow Ohm's law for dc current, and complex quantities of capacitance and inductance are found to be $1/(j\omega C)$ and $j\omega L$, respectively. The complex quantity $Z(\omega)$ is defined as the impedance function, and its value at a particular frequency is called the impedance of the electric circuit. $Z(\omega)$ is composed of a real (Z') and an imaginary (Z'') part, and expressed as $Z(\omega) = Z' + jZ''$.

$Z(\omega)$ can be plotted as a planar vector on a complex plane, where the real part is plotted on the x axis and the imaginary part on the y axis of a chart, in what is called a Nyquist plot or a Cole-Cole plot. In the Nyquist plot, in general, the y axis is negative and each point on the plot corresponds to the impedance Z at one frequency. There is another way to plot the impedance function, which is known as a Bode plot. The impedance is plotted with log frequency on the x axis and both the absolute value of the impedance and phase-shift on the y axis. Unlike the Nyquist plot, the Bode plot shows frequency information directly. Figure 24 shows an example of a Nyquist plot and Bode plot which was obtained from the same reference sample.

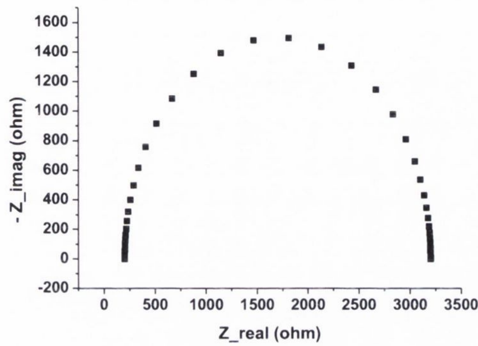

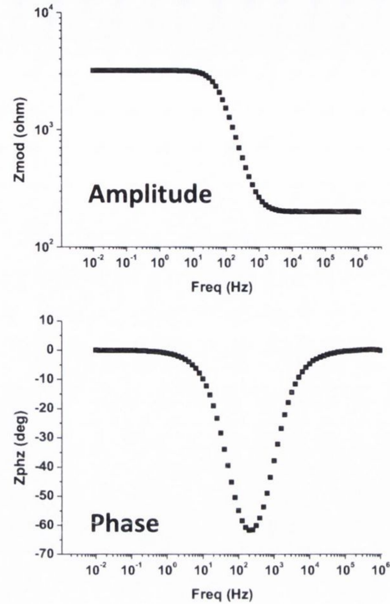

Nyquist plot

Bode plot

Figure 24 **Nyquist plot (left) and Bode plot (right) which was measured from the same system.**

As previously mentioned, impedance spectra can be interpreted using the combination of an appropriate electrical equivalent circuit model and a simulation process since IS spectra are dependent on the impedance elements of a system. Depending on which elements exist and how they are combined, different spectra are obtained. Examples of Nyquist plots of IS spectra which were measured from different systems are presented in Figure 25.

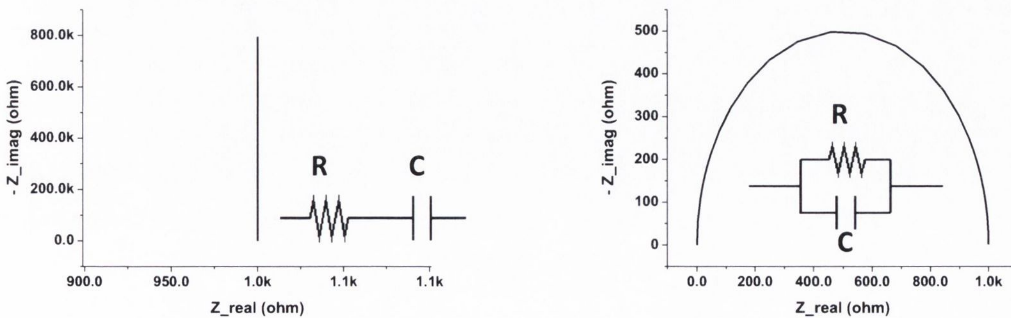

Figure 25 **Examples of Nyquist plots of IS spectra measured from a serially (left) and parallel (right) connected RC system.**

Therefore, it is essential to use proper circuit elements such as resistor (R), capacitor (C) and inductor (L) with their mathematical form of impedance. Table 4 lists the common circuit elements, the equation for their current-voltage relationship and their impedance.

Table 4 Mathematical expression of impedances for commonly used circuit elements.

Circuit Element	Current (I) vs. Voltage (V)	Impedance (Z)
Resistor (R)	V = I × R	$Z_R = R$
Inductor (L)	V = L × [dI/dt]	$Z_L = j\omega L$
Capacitor (C)	I = C × [dV/dt]	$Z_C = 1/(j\omega C)$

Once a proper equivalent circuit model is built, it is possible to quantify each circuit element from an iteration process, where calculated values from the model are compared with measured IS data and the calculated values of the circuit elements having the best fit with the experimental data are determined. Figure 26 shows an example of an equivalent circuit model for a system and the extracted values of the circuit elements in the model from a simulation process.

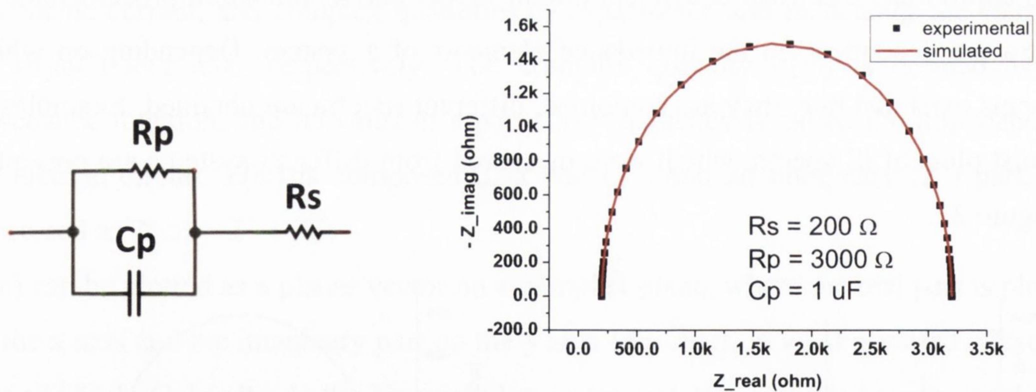

Figure 26 Equivalent electrical circuit model of a system consisting of RC components (left), and the experimental data measured by IS and its simulated values (right) using the equivalent circuit model.

When an equivalent circuit model for a system is composed of several impedance elements in a network, depending on its combination type (serial or parallel connection) it can be summed as a single equivalent impedance, which is analogous to the

calculation of the total resistance for combined resistors in a dc circuit. Examples of the calculation for the serial and parallel combination of impedances are shown in Figure 27.

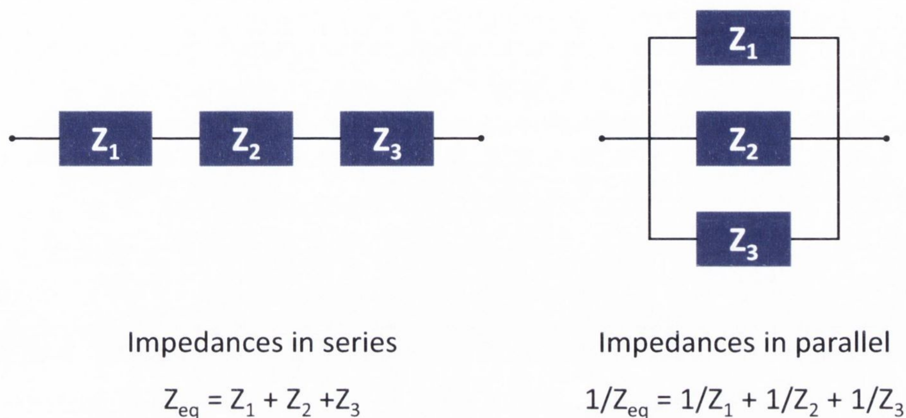

Figure 27 Serial and parallel combinations of impedances.

In this work, IS measurements were carried out using a Gamry Reference 600 Potentiostat with a two-electrode mode configuration and Gamry Echem Analyst software was used for the data analysis.

3. Conductive Carbon-Silicon Schottky Contacts

3.1 Schottky Contacts between PyC/PPF and Silicon*

3.1.1 Background

It is well known that the quality of metal-semiconductor (M-S) contacts is one of the most critical factors which determine the performance of semiconductor devices or integrated circuits. When a metal makes contact with a semiconductor, an energy barrier is formed at the interface. This barrier controls the current conduction at the interface. M-S contacts show either rectifying or ohmic behaviour at the contact area depending on the difference in work function of the two materials. Good ohmic contacts are essential for achieving excellent performance in a semiconductor device, while rectifying contacts (*i.e.* Schottky contacts) can be used for a wide variety of device applications. Schottky contacts can also be used as test vehicles for investigating the physical and electrical properties of a semiconductor material and its surfaces.[156,157] For example, a Schottky diode can be used to study bulk defects and interfacial properties of M-S systems.[158-160] Therefore, it is important to obtain a better understanding of the fundamental physical and electrical properties of M-S systems to assist the development of technologies for forming high quality M-S contacts, crucial for a wide variety of device applications.

Traditionally dc current-voltage (*J-V*) and capacitance-voltage (*C-V*) measurement techniques have been employed in order to define the electrical characteristics of M-S contacts. Complementary to this, impedance spectroscopy (IS) is a powerful method for characterising the electrical properties of materials and their interfaces.[161] In particular, the interfacial region of M-S contacts can be characterised with an appropriate equivalent circuit model developed from the impedance spectra. Although some analytical approaches have been introduced to describe the conduction mechanism between a metal electrode and a single individual semiconducting nanowire,[162,163] analyses of the electrical nature of the Schottky contacts in diode devices using ac impedance measurements have rarely been reported

It is also critical to choose a proper material depending on the current density of the diode device. Novel materials such as III-V semiconductors and SiC SBDs can provide

* Parts of this chapter appeared in P-7, P-9 and P-10.

higher performance than traditional silicon devices; however the cost of such substrates is very high. Thus, novel materials meeting high performance at low cost have great commercial opportunities. Since the discovery of carbon nanotubes and graphene their use for nano-electronics devices has been widely proposed,[8,164-169] but questions over their integration into devices remain. The use of graphene in a SBD has been shown principally by Chen *et al.,* however a lot of improvements in fabrication and performance are needed before viable applications can be considered.[170] On the other hand, glassy and pyrolytic carbon can be fabricated at low cost with reliable results. Since they have good electrical conductivity they can be considered as one of the possible alternatives to traditional metal electrodes.[28,41,47,48]

In this work, carbon-silicon interfaces in SBDs are investigated. The devices were fabricated with two different conductive carbon thin films as metallic layers on silicon substrates. Both dc *J-V* and ac IS analysis methods were used to investigate the electrical characteristics of the carbon-silicon SBDs alongside structural characterisation. From the dc *J-V* measurement, diode parameters of the conventional equivalent circuit model including the ideality factor, n, the barrier height, φ_B and the series resistance, R_S, are determined. From the ac impedance measurements, under various dc bias conditions, an advanced equivalent circuit model which offers more insight into the system was developed. As a result, a deeper understanding of the electrical properties of M-S contacts is possible using the introduced methods.

3.1.2 Film Synthesis

Two different types of conductive carbon thin films were synthesised on n-type silicon (n-Si) wafers with a dopant (Phosphorus) concentration of 5×10^{14} cm^{-3} and <100> orientation. The n-Si wafers were cleaned in acetone and isopropyl alcohol. The native oxide layer on the silicon surface was removed by wet-etching by immersion in 3.3 % solution of hydrofluoric acid (HF) for 1 minute followed by rinsing with DI water and blow drying with N_2.

Firstly, AZ nLOF 2070, which is a negative tone photoresist, was spin-coated on n-Si substrates at speeds of 5000 rpm for 45 seconds followed by soft baking for 1 minute at 100 °C, which gives a resist thickness of 100 nm to 500 nm. Then it was pyrolysed in a

furnace at 1000 °C for 1 hour with the hydrogen gas flow (10 sccm).[28] Upon pyrolysis, a conductive carbon layer known as a PPF was obtained.

Secondly, a PyC layer was grown on n-Si substrates by CVD. This was grown in a quartz tube furnace (700 × 90 mm) using acetylene (C_2H_2) as the hydrocarbon feedstock at a flow rate of 180 sccm at a growth temperature of 950 °C and a pressure of 20 Torr. The growth time was 5 minutes to give a film of approximately 60 nm thickness.[41]

3.1.3 Film Characterisation

Electron Microscopy Analysis: Electron microscopy tools have been used in order to define the cross-sectional structure of the conductive carbon thin film layer. Thickness information and the interface condition of the carbon thin film was verified through the cross-sectional images from SEM and HRTEM.[†] HRTEM studies were performed on cross sections of PPF and PyC on Si substrates.

Figure 28 shows cross-sectional images of conductive carbon thin films, PPF and PyC from SEM and HRTEM. The thickness of the carbon layers taken from cross-sectional images is 78 – 80 nm for the PPF layer and 62 – 65 nm for the PyC layer. This film thickness was found to be easily accessible experimentally and also practical for further processing such as etching and forming electrical contacts. Both films are reasonably homogenous in thickness as visible in the Figure 28(a) and (b), and therefore, they were well suited to sheet resistance measurements and ellipsometry analysis. Thus those measurements, which are much easier and non-destructive, could be used in the following to determine film thickness. Cross-sectional HRTEM analysis of the interface between carbon thin films and silicon substrates is depicted in Figure 28(c) and (d). The PPF film appears to be completely amorphous (Figure 28(c)).

The interface region between the bulk PPF and silicon is slightly darker than the bulk PPF region. However, it is obvious from the corresponding diffraction patterns that both the bulk and interface area of the PPF have the same amorphous structure typical for glassy carbon. In contrast, the PyC layer has a slightly laminar structure parallel to the underlying substrate with a very thin disordered carbon region at the interface

[†] Cross-sectional HRTEM imaging was performed by Ehsan Rezvani.

(Figure 28(d)), which is clearly verified by the corresponding diffraction patterns.[171] The typical length scale for this is in the order of a few nanometres in agreement with the assumption that PyC is composed of nanocystalline graphitic domains. No obvious interfacial layer (e.g. SiO_2) between the Si and carbon layers is visible implying direct linking of the crystalline Si to the carbon, however its existence cannot be completely ruled out by HRTEM analysis.

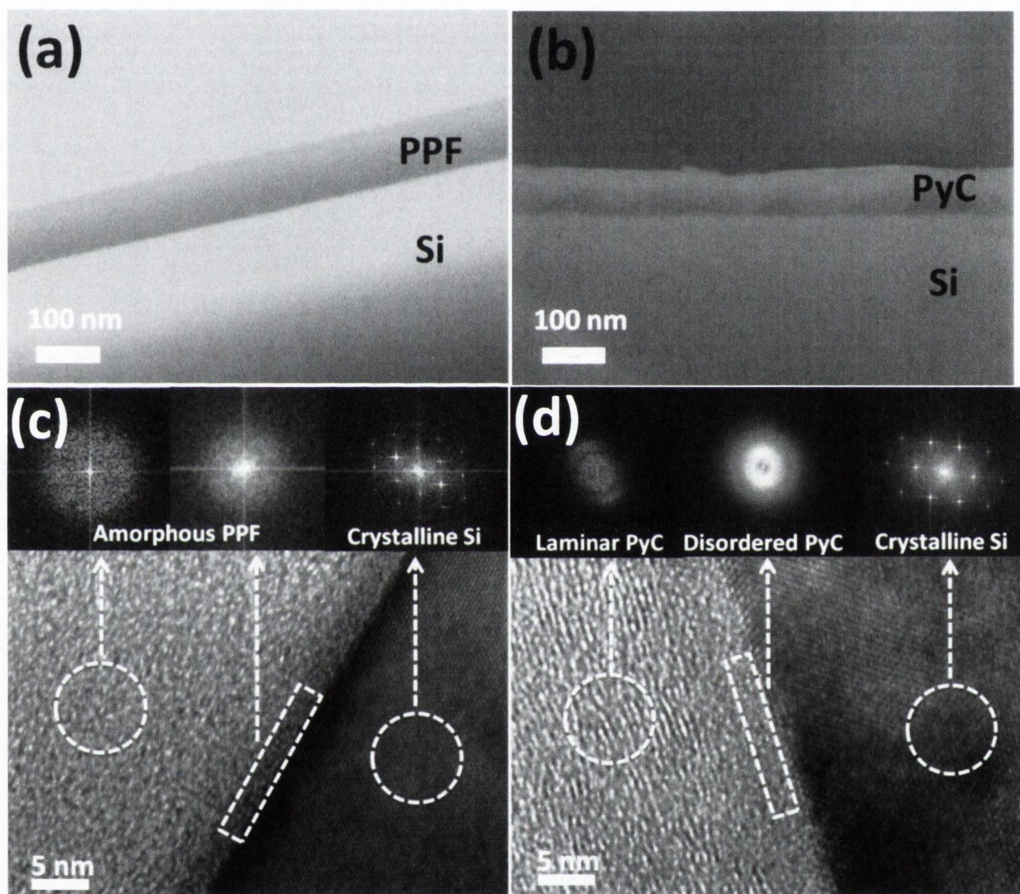

Figure 28 Cross-sectional SEM images of (a) PPF and (b) PyC, and HRTEM images of (c) PPF and (d) PyC on silicon substrates.

Raman Analysis: Raman spectroscopy was performed using a Witec Alpha 300R Raman microscope with an excitation wavelength of 532 nm.[‡] Figure 29 shows the result of Raman spectra from PPF and PyC films on silicon substrates exhibiting D and G bands. The Raman spectra of PPF and PyC are nearly identical and typical of highly disordered sp^2 carbon materials. PPF has a slightly larger D/G ratio with (~1.05) than

[‡] Raman spectroscopy was performed with the assistance of Dr. Niall McEvoy.

PyC with (~0.95) suggesting a higher degree of disorder, which is in agreement with the TEM observations depicted in Figure 28. Building on the work of Tuinstra and Koening,[172] Cancado *et al.* developed an equation relating the ratio of the integrated intensities of D and G band to the crystallite size.[173] The average crystallite sizes of PPF and PyC were estimated using this equation. By fitting D and G band components only this yielded values of 6.7 nm and 4.9 nm for PPF and PyC, respectively. However, this interpretation can be considered an over simplification as it fails to account for additional contributions seen in the Raman spectra of such heavily disordered nanocarbon systems as outlined previously.[41,174] In addition, the materials being probed lie at the end of the first branch of the amorphisation trajectory of graphitic materials at which point this equation becomes unreliable.[175] Using a more comprehensive fitting, taken into account contributions from D′, D″ and I bands, yields estimates for the average crystallite size of 5.5 nm and 5.7 nm for PPF and PyC, respectively.

A Si peak is observed in the PyC Raman spectrum below 1000 cm^{-1} which stems from the substrate, and this implies that the PyC film is slightly thinner than the PPF film, and therefore still optically transparent.[28,41] This result is in agreement with the thickness values of PPF and PyC from cross-sectional analysis with electron microscopy.

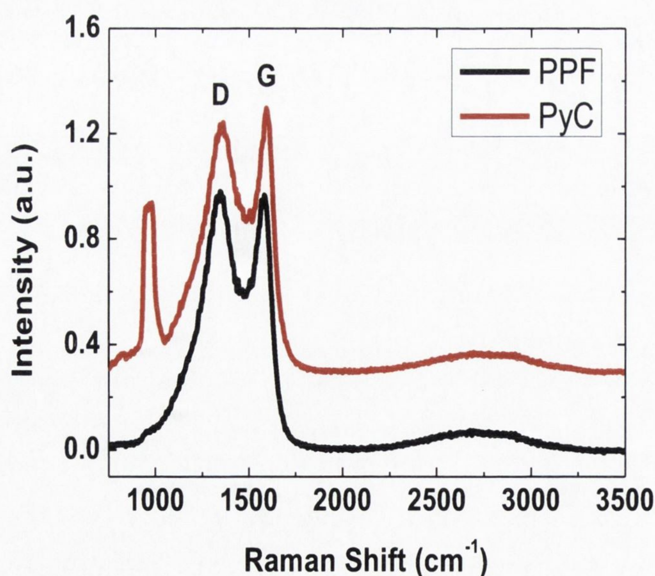

Figure 29 Raman spectra of PPF and PyC films with an excitation wavelength of 532 nm exhibiting broad D and G bands.

Spectroscopic Ellipsometry Analysis: Optical constants of thin films can be obtained using spectroscopic ellipsometry (SE). Carbon thin films with the size of 3 cm × 3 cm were prepared on Si substrates for SE measurement. SE spectra were gathered over the full spectral range (380 nm – 900 nm) with a spectroscopic resolution of 3 nm in order to define optical constants of the carbon thin films. Three incident angles (65 °, 70 °, and 75 °) were used for the measurement. Data analysis was carried out with CompleteEASE software, provided by J. A. Woollam Company. Material dispersion models for both PPF and PyC were developed using a Tauc-Lorentz model[146,176] which is one of the oscillator function models. The complex dielectric function of the energy (E) is defined as $\varepsilon(E) = \varepsilon_1 + i\varepsilon_2$ where ε_1 is the real part and ε_2 is the imaginary part of $\varepsilon(E)$ respectively. In the Tauc-Lorentz model,[176] ε_1 and ε_2 are defined as

$$\varepsilon_2 = \left[\frac{AE_0C(E-E_b)^2}{\left(E^2-{E_0}^2\right)^2+C^2E^2}\cdot\frac{1}{E}\right] \; for \; E > E_b, \qquad \varepsilon_2 = 0 \; for \; E \leq E_b, \tag{3.1}$$

$$\varepsilon_1 = \varepsilon_1(\infty) + \frac{2}{\pi}P\int_{E_b}^{\infty}\frac{\xi\varepsilon_2(\xi)}{\xi^2-E^2}d\xi, \tag{3.2}$$

where A, C, E_0 and E_b represent the amplitude, broadening, centre energy and band gap of the oscillator, respectively, which all have units of energy (eV), and P stands for the Cauchy principal part of the integral.

The values for the refractive index (n) and extinction coefficient (k) of PPF and PyC versus wavelength λ were determined through an iterative fitting process with the newly developed dispersion model. Two oscillator functions were used to model the dispersion of PPF and PyC. Table 5 summarises the oscillator parameters which were used in the developed dispersion model.

Table 5 The summary on the oscillator parameters of the Tauc-Lorentz model developed for the material dispersion models of PPF and PyC. (MSE*: Root Mean Square Error).

Parameter [unit]	Amp_1 [eV]	Br_1 [eV]	E_{01} [eV]	E_{g1} [eV]	Amp_2 [eV]	Br_2 [eV]	E_{02} [eV]	E_{g2} [eV]	MSE*
PPF	11.16	1.74	1.10	0.30	24.63	6.97	4.48	0.06	1.34
PyC	112.03	5.63	5.45	1.50	44.87	3.00	1.50	0.53	1.29

Figure 30(a) and (b) show plots of the extracted n and k values as a function of wavelength and energy for PPF and PyC. Both show an increase of k values at the range of 380 – 500 nm, implying the possible existence of an absorption peak in the UV

region. Compared to the previous ellipsometry studies on the optical constants of PPF[177] and pyrolytic graphite[178] which are presented in Figure 30(c) and (d), it can be verified that the extracted n and k values from this work show good agreement with them. Slight differences in the magnitude of n and k values between this work and literature could be due to the disparities in a number of factors such as surface roughness, the size and distribution of graphitic crystallites, the film growth parameters used, and the degree of anisotropy.

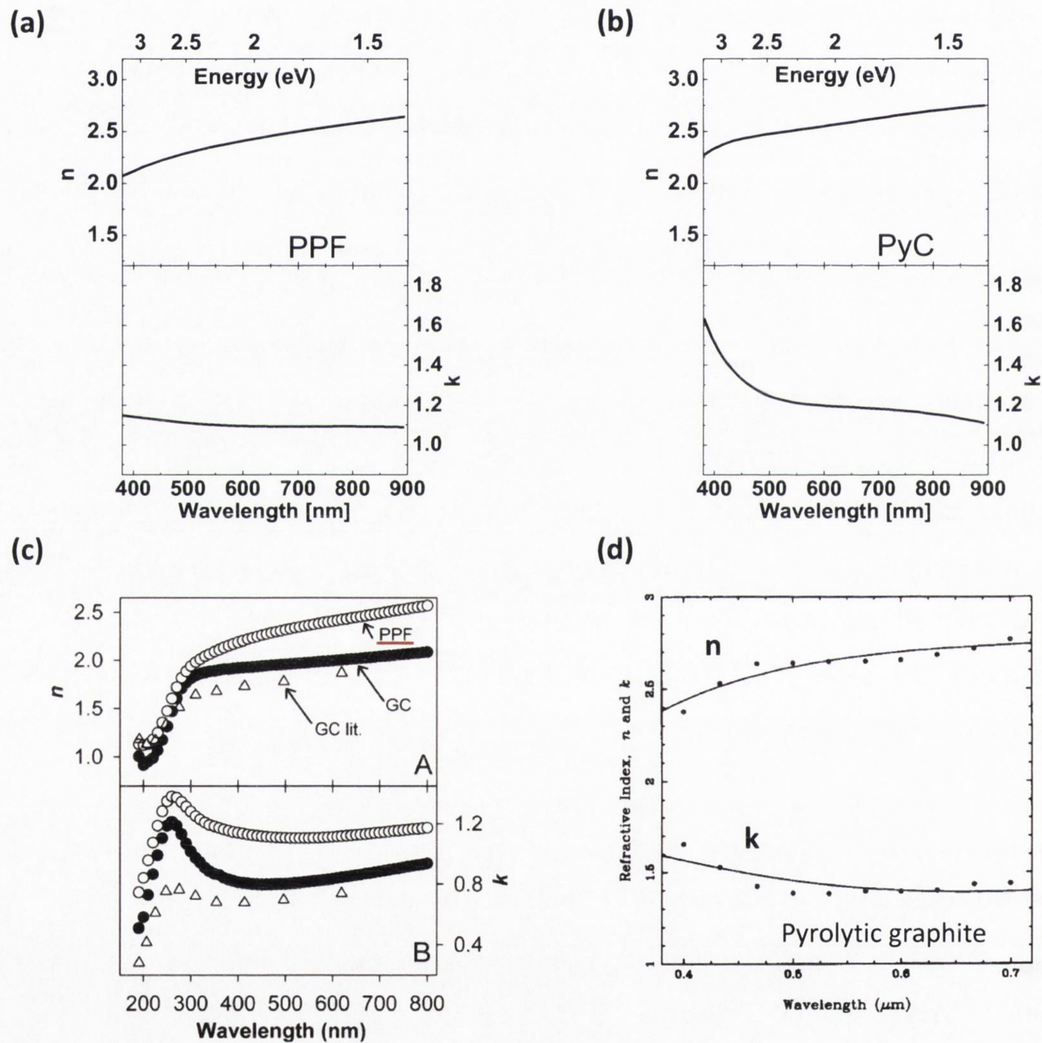

Figure 30 Optical constants (n and k) plots for (a) PPF and (b) PyC films from this work. (c) n and k values of glassy carbon (GC) and PPF from ref[177]. (d) n and k values of pyrolytic graphite from ref[178].

Sheet Resistance Measurement: The sheet resistance of PPF and PyC films was measured using a four-point probe head (Jandel) connected to a Keithley 2400 SMU. Four-point probe measurements at room temperature were taken at different locations on each film and ten measurements were taken to ensure the data integrity and the average value was calculated. The samples were also rotated to ensure that there was no anisotropy in the measurement of the films. As previously explained, the sheet resistance R is given by the formula; $R = \rho/t = (\pi/\ln 2)V/I = 4.53(V/I)$ [Ωm], where 4.53 is a correction factor which depends on the dimensions of the sample being probed and the inter-probe spacing. For samples with thicknesses (t) much less than the spacing (s) between probes and lateral dimensions much larger than the spacing between probes a correction factor of ($\pi/\ln 2 = 4.53$) is suitable. The resistivity values, deduced from four-point measurements on insulating substrates are 4.0×10^{-5} Ωm with standard deviation of 2.4×10^{-6} Ωm for PPF and 2.5×10^{-5} Ωm with standard deviation of 2.8×10^{-6} Ωm for PyC films, respectively. These similarities are remarkable as the two materials are related to glassy (PPF) and nanocrystalline (PyC) carbon structures.

3.1.4 Device Fabrication

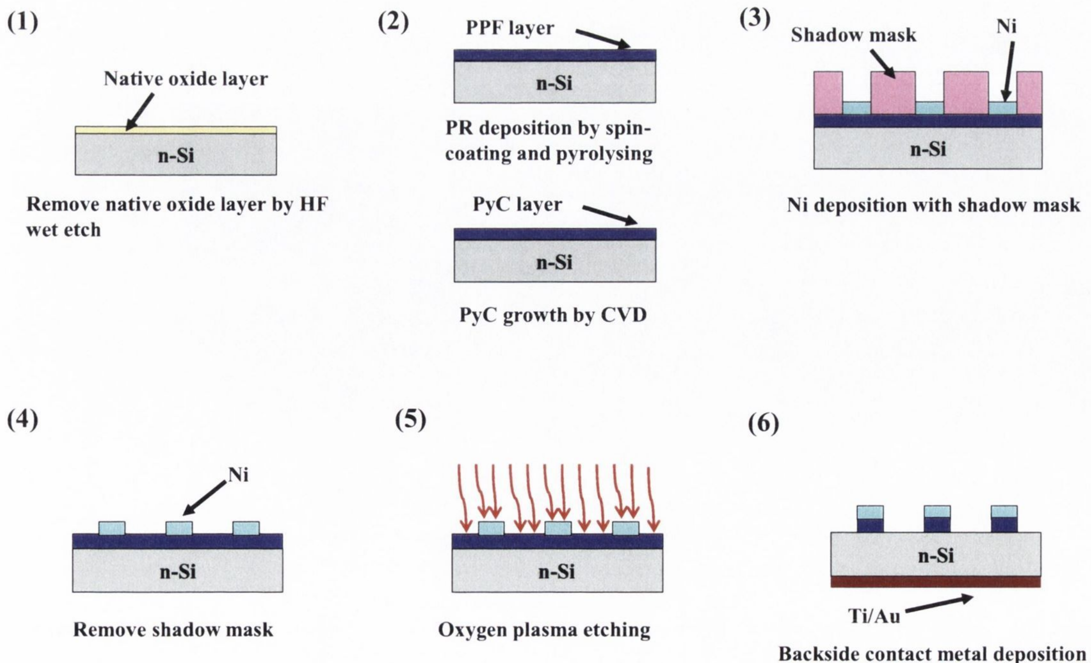

Figure 31 Carbon-silicon SBD device fabrication process.

A schematic of carbon-silicon Schottky barrier diode (SBD) device fabrication processes is shown in Figure 31. The devices were fabricated on n-Si wafers with a dopant (Phosphorus) concentration of 5×10^{14} cm^{-3} and <100> orientation. The n-Si wafers were cleaned in acetone and isopropyl alcohol. The native oxide layer on the silicon surface was removed by wet-etching by immersion in 3.3 % solution of hydrofluoric acid (HF) for 1 minute followed by rinsing with DI water and blow drying with N_2.

After carbon deposition arrays of 50 nm thick nickel (Ni) dots with a radius of 1 mm were created using a shadow mask as shown in Figure 31. Each dot with a nickel/carbon/silicon structure operates as a separate diode with an interface area of 3.1×10^{-2} cm^2. The carbon film between the metal dot patterns was removed with oxygen plasma etching using the nickel dots as a hardmask. The surface of the silicon backside was cleaned using oxygen plasma etching to completely remove carbon residue and other contamination. This was followed by native oxide removal by a HF dip. Ohmic contacts with 20 nm of titanium (Ti) and 40 nm of gold (Au) were then deposited. All metal layers were deposited using a Gatan Model 682 PECS.

3.1.5 Current-Voltage Measurement

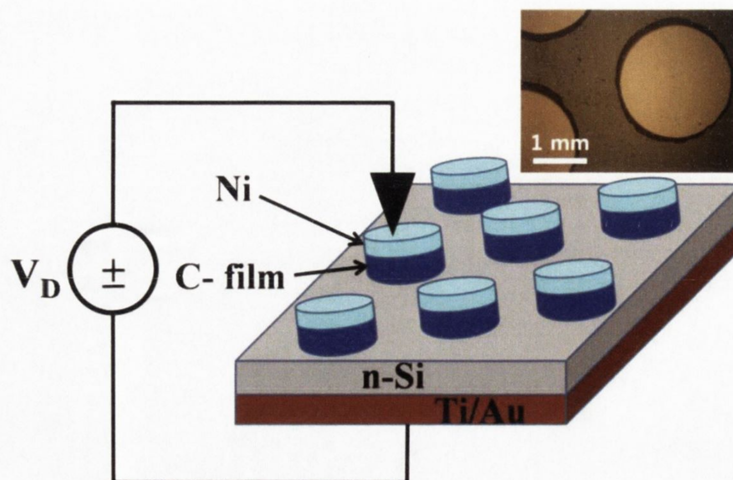

Figure 32 Schematic and optical microscope image (top view) of the carbon/n-Si Schottky barrier diode.

A schematic and an optical microscopy image of the diodes produced are depicted in Figure 32. The area of the interface is 3.1×10^{-2} ($\pm 1.8 \times 10^{-3}$) cm^2 without the usage of any guard ring to prevent leakage currents at the device perimeter. Figure 33(a) and (b) show the *J-V* characteristics of PPF/n-Si and PyC/n-Si SBD devices, respectively. The measurements were carried out with a dc bias range of ± 4 V under ambient conditions. The Ni metal dot electrodes are positively biased in the forward-bias region, and conversely biased in the reverse-bias region. Both devices present clear rectifying behaviour, indicating the formation of Schottky contacts between carbon thin films and n-Si substrates. Since the current transport in Schottky contacts can be explained by thermionic emission theory, the relationship between the current density, J and the voltage drop across the junction, V_D, can be given by the following equation:[157,179]

$$J = J_S\left[exp\left(\frac{qV_D}{nk_BT}\right) - 1\right], \tag{3.3}$$

where J_S is the reverse saturation current density and can be expressed as

$$J_S = A^{**}T^2exp(\frac{-q\varphi_B}{k_BT}), \tag{3.4}$$

where q is the elementary charge, T is the absolute temperature, k_B is the Boltzmann constant, n is the ideality factor, A^{**} is the effective Richardson constant which is equal to 112 $Acm^{-2}K^{-2}$ for n-Si, and φ_B is the effective barrier height at zero bias.

When the effect of series resistance, R_S, of the system is taken into account, the voltage across the diode can be expressed in terms of the total voltage drop, V, across the series combination of the diode and the resistor. Thus, $V_D = V - JR_S$, and for $V_D > 3k_BT/q$, Eq. (3.3) becomes

$$J = J_Sexp[\frac{q(V-JR_S)}{nk_BT}]. \tag{3.5}$$

Therefore, the carbon-silicon SBDs can be modelled with a conventional equivalent circuit model with the ideality factor n and the series resistance R_S as shown in the inset of Figure 33(a) and (b). Using Cheung's method,[180] Eq. (3.5) can be rewritten:

$$V = JAR_S + n\varphi_B + \left(\frac{nk_BT}{q}\right)ln(\frac{J}{A^{**}T^2}), \tag{3.6}$$

where A is the effective diode area.

When the Eq. (3.6) is differentiated with respect to the current density J, we obtain

$$\frac{dV}{d(lnJ)} = JAR_S + \frac{nk_BT}{q}. \tag{3.7}$$

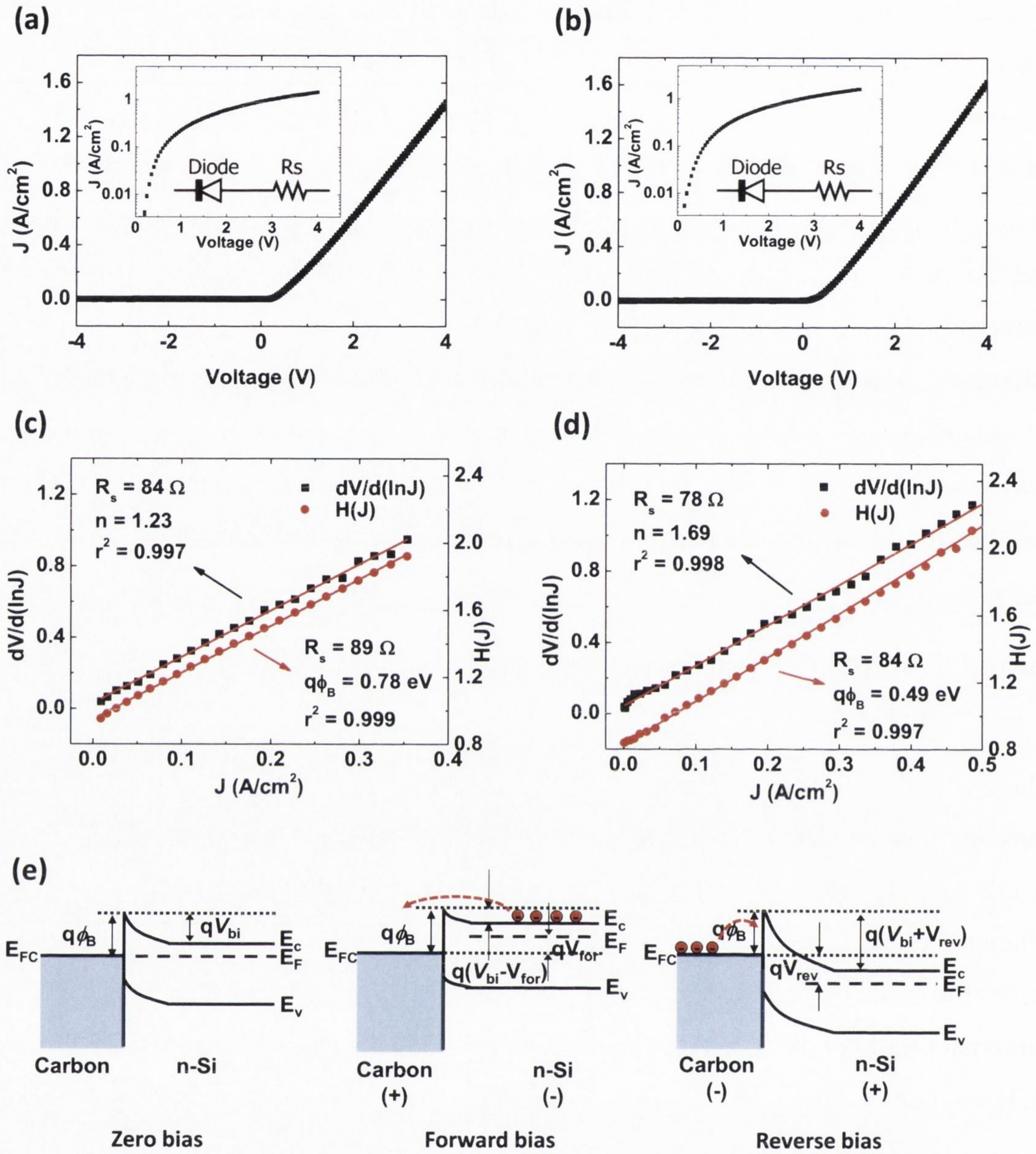

Figure 33 *J-V* measurements of (a) the PPF/n-Si SBD and (b) the PyC/n-Si SBD on a linear scale. Insets denote the plots on a semi-logarithmic scale and the dc equivalent circuit model of the diode. Plots of *dV/d(*ln*J)* vs. *J* and *H(J)* vs. *J* for (c) the PPF/n-Si and (d) the PyC/n-Si SBDs. (e) Energy-band diagram of a conductive carbon thin film on n-Si substrates under zero, forward and reverse bias. φ_B, E_c, E_v, E_F, E_{FC}, V_{bi}, V_{for} and V_{rev} indicate the Schottky barrier height, bottom energy of conduction band of n-Si, top edge of valence band of n-Si, Fermi energy level of n-Si, Fermi energy level of carbon, built-in potential, forward bias and reverse bias, respectively.

In Eq. (3.7), a linear relationship can be expected from the plot of $dV/d(\ln J)$ vs. J, giving the AR_S value from the slope and the n value from the y-axis intercept of the plot. Also, from Eq. (3.6), the auxiliary equation $H(J)$ can be defined as

$$H(J) = V - \left(\frac{nk_BT}{q}\right) ln\left(\frac{J}{A^{**}T^2}\right), \quad (3.8)$$

$$H(J) = JAR_S + n\varphi_B. \quad (3.9)$$

Using the value of n derived from Eq. (3.7) and the result of $H(J)$ from Eq. (3.8), the plot of $H(J)$ vs. J from Eq. (3.9) gives a straight line with y-axis intercept equal to $n\varphi_B$. In addition, the slope of this plot gives the value of series resistance by which the consistency of R_S from Eq. (3.7) can be checked. The plots of $dV/d(\ln J)$ vs. J and $H(J)$ vs. J for the PPF/n-Si and the PyC/n-Si SBD devices are presented in Figure 33(c) and (d). The PPF/n-Si SBD device has R_S values of 84 ± 1 Ω and 89 ± 1 Ω derived from the plots of $dV/d(\ln J)$ vs. J and $H(J)$ vs. J, respectively, which are in good agreement. The values of n and $q\varphi_B$ were found to be 1.23 ± 0.02 and 0.78 ± 0.01 eV, respectively. In the case of the PyC/n-Si SBD, the values of R_S from the plots of $dV/d(\ln J)$ vs. J and $H(J)$ vs. J are 78 ± 2 Ω and 84 ± 2 Ω, respectively with the values of n = 1.69 ± 0.03 and $q\varphi_B$ = 0.49 ± 0.02 eV. A schematic energy-band diagram of the interface between conductive carbon thin films and n-Si substrates under various dc bias conditions is depicted in Figure 33(e). A space-charge region accompanied by the built-in potential (V_{bi}) is formed in the n-Si near the carbon-Si interface under zero bias. Depending on the external dc bias, current can flow over the reduced barrier under forward bias, or can be blocked by the Schottky barrier under reverse bias, which is typical rectifying behaviour.

Six different carbon/n-Si SBD devices were fabricated for each type of carbon and their characteristics were examined to highlight their reproducibility. The PPF/n-Si SBDs showed all very reproducible behaviour while the PyC/n-Si SBDs had slight variation under reverse bias, still showing good rectifying characteristics. Current-voltage measurement plots and a data summary for these are presented in Figure 34 and Table 6, respectively. The results from current-voltage measurements taken on six different carbon/n-Si SBD devices show the average values of each diode parameter for these devices are n = 1.29, $q\varphi_B$ = 0.71 eV, R_S= 52.25 Ω for the PPF/n-Si SBD devices, and n = 1.44, $q\varphi_B$ = 0.56 eV, R_S= 49.96 Ω for the PyC/n-Si SBD devices. Considering the low values of the ideality factor calculated for these devices, one can say that these carbon-Si diodes show high performance and are within reach of commercial devices which have ideality factor values between 1.05 and 1.20. This in itself is a remarkable result considering it was achieved without any optimization. Furthermore, it is expected

that device performance can be improved up to the level of commercial requirements with more advanced fabrication processes.

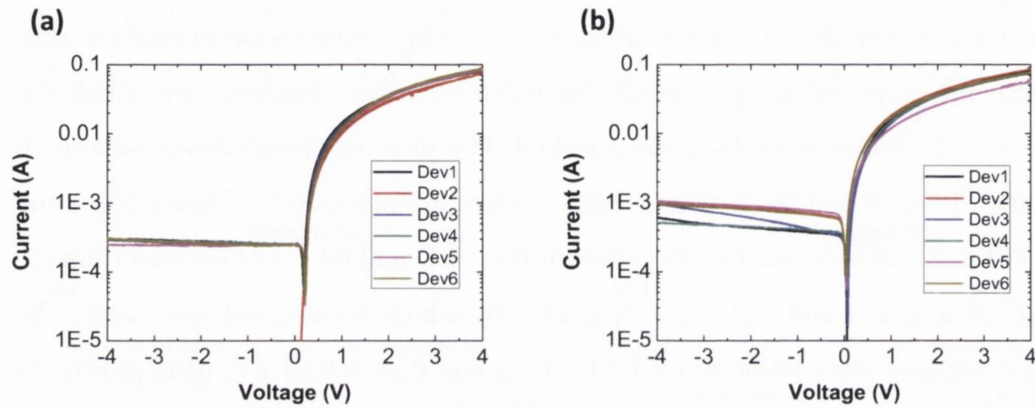

Figure 34 Semi-logarithmic current-voltage curves of six different carbon/n-Si Schottky diode devices for (a) PPF/n-Si diode and (b) PyC/n-Si diode.

Table 6 Summary of data taken on six different carbon/n-Si Schottky barrier diode devices at room temperature.

Device		Dev1	Dev2	Dev3	Dev4	Dev5	Dev6	AVG	STD
	n	1.28	1.37	1.25	1.32	1.22	1.29	**1.29**	0.05
PPF/n-Si	$q\phi_B$ [eV]	0.69	0.76	0.69	0.69	0.71	0.70	**0.71**	0.03
	R_S [Ω]	44.83	53.93	49.36	55.35	56.22	53.81	**52.25**	4.34
	n	1.44	1.45	1.45	1.41	1.55	1.37	**1.44**	0.06
PyC/n-Si	ϕ_B [eV]	0.60	0.52	0.62	0.58	0.52	0.53	**0.56**	0.04
	R_S [Ω]	42.10	45.02	46.58	48.97	68.33	48.73	**49.96**	9.35

3.1.6 Impedance Spectroscopy

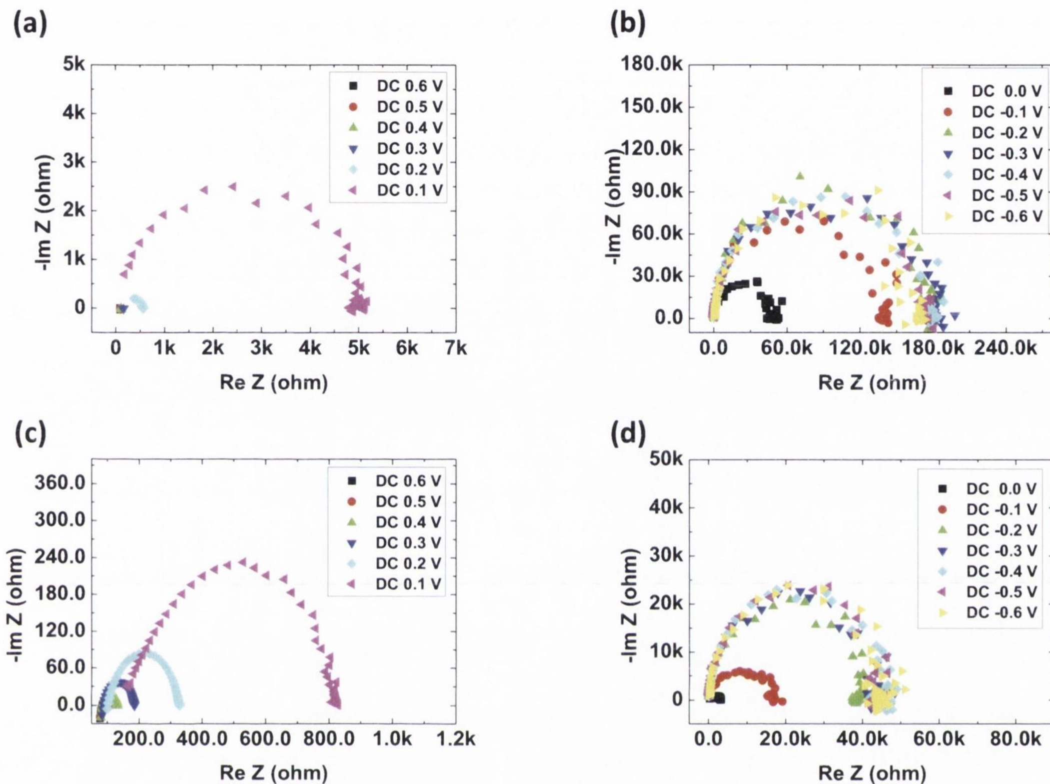

Figure 35 **Nyquist plots of the PPF/n-Si SBD (a) under forward dc bias voltages and (b) under zero and reverse dc bias voltages. Nyquist plots of the PyC/n-Si SBD (c) under forward dc bias voltages and (d) under zero and reverse dc bias voltage with frequencies increasing from the right to the left of the x axis (from 0.1 Hz to 1 MHz).**

Ac impedance spectra of the carbon-silicon SBD devices were recorded in the frequency range of 0.1 Hz to 1 MHz with an oscillating voltage of 10 mV during dc voltage scanning from -0.6 to +0.6 V in steps of 0.1 V at room temperature. Figure 35 shows the Nyquist impedance plots of each carbon-silicon SBD under varying dc bias voltages, in which the implicit variable is the frequency increasing from the right to the left on the x axis (from 0.1 Hz to 1 MHz). It is observed that the impedance spectra are nearly semi-circular over the whole dc bias range, implying that the equivalent circuit of the device consists of a combination of resistance and capacitance (RC) networks.[161] The diameter of each semi-circular arc corresponds to the total impedance of the device. It should be noted that the several uncompleted semicircles in these plots are due to instrument limitation in this frequency range. In both devices, the radius of the

semicircles increases when the positive dc bias is decreased and they further increase under negative bias, demonstrating the bias dependence of resistance and capacitance values of the devices. In addition, some scattering of the data points in the low-frequency regime is observed which is more pronounced at high reverse bias.

In order to gain a deeper understanding of the Schottky contact an ac equivalent circuit model (ECM) was developed. The typical equivalent circuit model of a Schottky diode (ECM 1) is composed of a parallel connected RC network and a series resistance which is serially connected to the RC network,[156] as shown in Figure 36(a). The capacitance component (C_P) in the equivalent circuit denotes the depletion layer capacitance of the contact and the parallel resistance component (R_P) is associated with a shunt resistance.

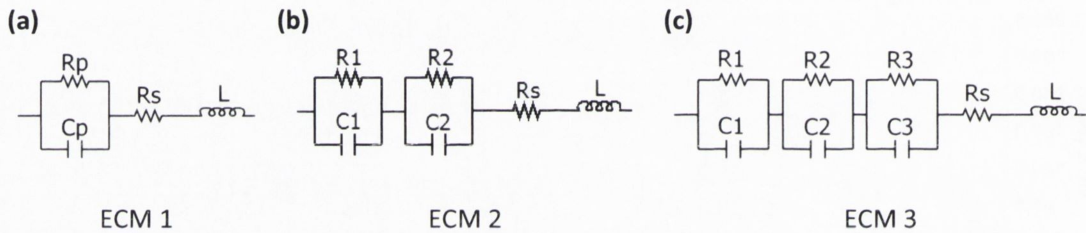

Figure 36 (a) A typical equivalent circuit model (ECM 1) of a Schottky diode. C_P denotes the depletion layer capacitance of the contact, R_P is associated with a shunt resistance and R_S is a series resistance. (b) ECM 2 with C_1 and C_2 being capacitances with corresponding shunt resistances R_1 and R_2 associated with the interfaces of metal electrodes (Ni-carbon and silicon-Ti) and a carbon-silicon interface , respectively. (c) ECM 3 with C_1, C_2 and C_3 being capacitances with corresponding shunt resistances R_1, R_2 and R_3, associated with a Ni-carbon interface, a carbon-silicon interface and a silicon-Ti interface, respectively. R_S is the series resistance and L represents a parasitic inductance associated with the electrical leads.

However, it is not always possible to match impedance spectra with this simple equivalent circuit since the contact area of metal electrodes can give rise to additional capacitive components in real devices. In this work, the simulated results from the best fit of the typical equivalent circuit model (ECM 1) in Figure 36(a) did not show good fitting with the measured data in the forward dc bias region, although they fitted well in the reverse dc bias region.

In order to better interpret the impedance spectra, a more complex version of the equivalent circuit model (ECM 2 and ECM 3) was developed, where the effect of contacts between the carbon and the Ni electrode, and/or the silicon and the Ti/Au

electrode was taken into account. The extended form of the equivalent circuit model of the carbon-silicon SBD structure is presented in Figure 36(b) and Figure 36(c). ECM 2 consists of two RC circuits in series lumped with a series resistance R_S and a parasitic inductance L. C_1 and C_2 are the capacitances associated with interfaces of the metal electrodes (Ni-carbon and silicon-Ti) and carbon-silicon interface, respectively with corresponding shunt resistances R_1 and R_2. ECM 3 consists of three RC circuits in series lumped with a series resistance R_S and a parasitic inductance L. C_1, C_2 and C_3 are the capacitances associated with a Ni-carbon interface, carbon-silicon interface and silicon-Ti interface, respectively with corresponding shunt resistances R_1, R_2 and R_3. The ac impedance of the circuit is given by[161]

$$Z(\omega) = Z'(\omega) - jZ''(\omega), \quad (3.10)$$

where ω represents the frequency, Z' and Z'' are the magnitudes of the real and imaginary parts of the impedance, and a minus sign arises due to capacitive reactance involved in the circuit. For the three ac equivalent circuit models of a Schottky diode in Figure 36, the magnitude of the real and imaginary parts of impedance can be written as following equations:

for ECM 1,

$$Z'(\omega) = \frac{R_p}{1+(\omega R_p C_p)^2} + R_S, \quad (3.11)$$

$$Z''(\omega) = \frac{\omega R_p^2 C_p}{1+(\omega R_p C_p)^2} - \omega L, \quad (3.12)$$

for ECM 2,

$$Z'(\omega) = \frac{R_1}{1+(\omega R_1 C_1)^2} + \frac{R_2}{1+(\omega R_2 C_2)^2} + R_S, \quad (3.13)$$

$$Z''(\omega) = \frac{\omega R_1^2 C_1}{1+(\omega R_1 C_1)^2} + \frac{\omega R_2^2 C_2}{1+(\omega R_2 C_2)^2} - \omega L, \quad (3.14)$$

for ECM 3,

$$Z'(\omega) = \frac{R_1}{1+(\omega R_1 C_1)^2} + \frac{R_2}{1+(\omega R_2 C_2)^2} + \frac{R_3}{1+(\omega R_3 C_3)^2} + R_S, \quad (3.15)$$

$$Z''(\omega) = \frac{\omega R_1^2 C_1}{1+(\omega R_1 C_1)^2} + \frac{\omega R_2^2 C_2}{1+(\omega R_2 C_2)^2} + \frac{\omega R_3^2 C_3}{1+(\omega R_3 C_3)^2} - \omega L. \quad (3.16)$$

The best fitted curves for forward (+0.4 V) and reverse (-0.4 V) bias data based on these equations are shown in Figure 37. The best fitted results from the equivalent circuit models show good fitting with the measured data under reverse dc bias (-0.4 V), while the fitted curve from the ECM 3 shows much better fitting with measured data than the fitted curve from the ECM 1 and ECM 2 under forward dc bias (+0.4 V). It

was also verified that the simulated data from ECM 3 led to a similarly good fit with the experimental data under various dc biases as shown in Figure 38 and Figure 39.

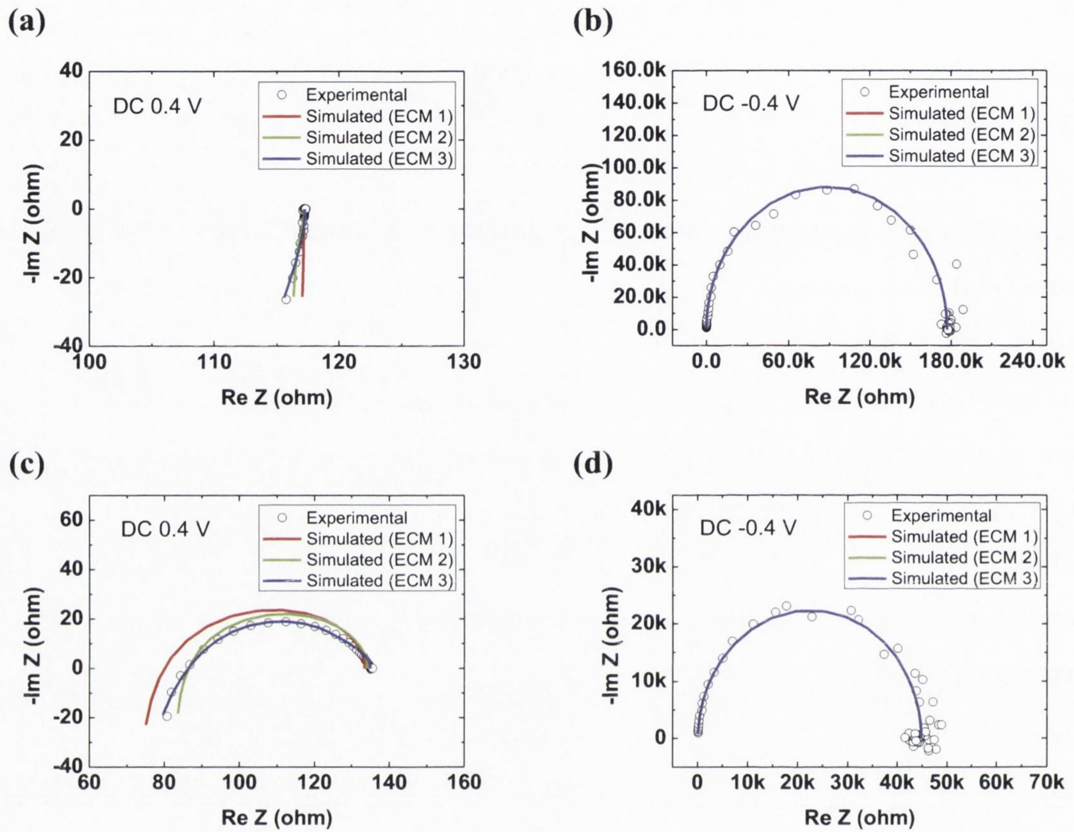

Figure 37 Nyquist plots and corresponding best fit from the equivalent circuit models of ECM 1, ECM 2 and ECM 3 on the PPF/n-Si SBD (a) under dc bias of +0.4 V and (b) -0.4 V, and the PyC/n-Si SBD (c) under dc bias of +0.4 V and (d) -0.4 V.

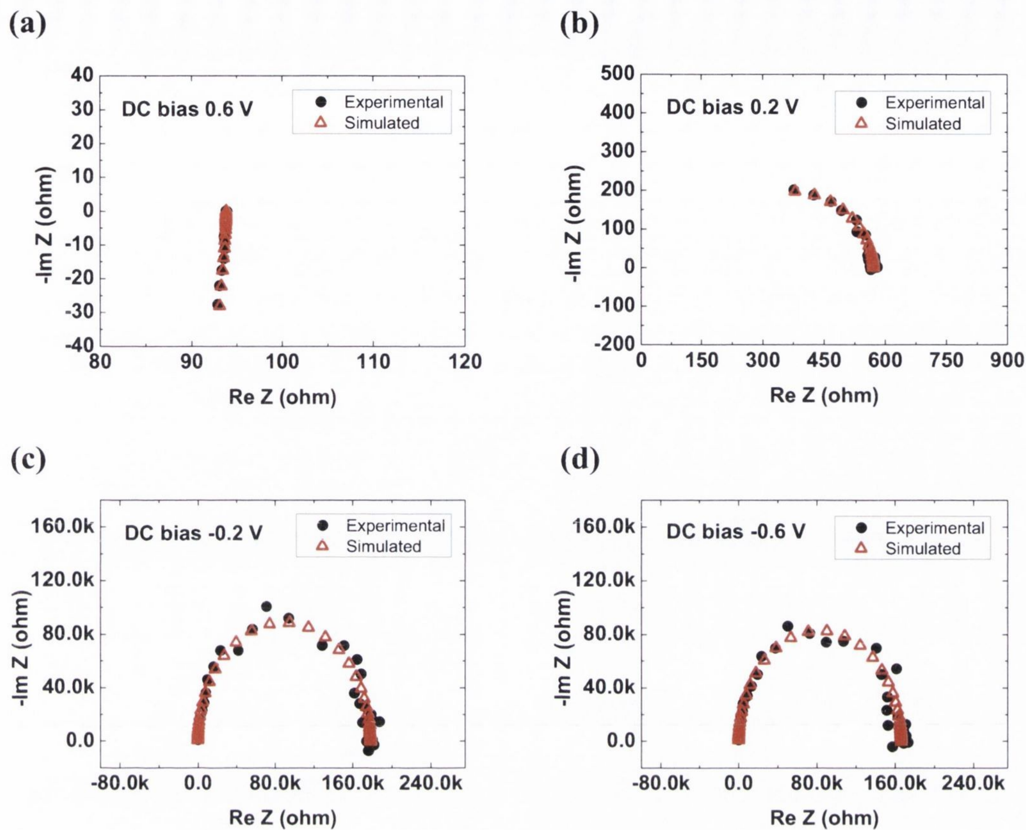

Figure 38 Nyquist plots and corresponding best fit from ECM 3 on the PPF/n-Si SBD under dc bias of (a) +0.6 V, (b) +0.2 V, (c) -0.2 V and (d) -0.6 V.

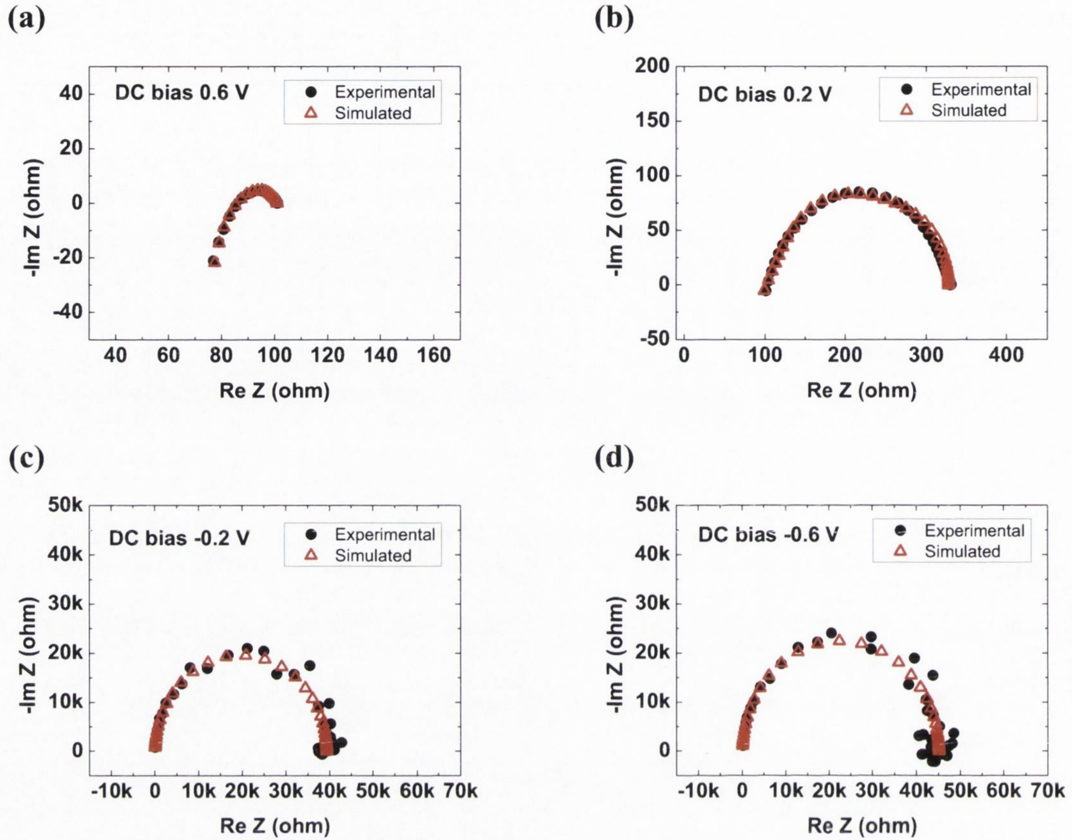

Figure 39 Nyquist plots and corresponding best fit from ECM 3 on the PyC/n-Si SBD under dc bias of (a) +0.6 V, (b) +0.2 V, (c) -0.2 V and (d) -0.6 V.

The values of resistance and capacitance obtained from the best fit of the measured impedance are plotted in Figure 40 for both carbon-silicon SBD devices and detailed data are presented in Table 7 and Table 8. The R_S of each device has a constant average value of 85 Ω for the PPF/n-Si SBD and 72 Ω for the PyC/n-Si SBD device. These do not show any significant change under different dc bias voltages and are in agreement with the R_S values from the dc *J-V* measurements. On the contrary, R_2 undergoes dramatic change when the dc bias is changed from the reverse region to the forward region in both devices. Moreover, R_2 has very high resistance values compared to R_1 and R_3 in the reverse dc bias regime, which clearly indicates that the R_2C_2 component is associated with the Schottky barrier between carbon and silicon because R_2 blocks the current flow through the junction under reverse dc bias. In the forward dc bias regime, R_2 drops significantly as the bias voltage increases, which makes sense given that more carriers are injected into the Schottky junction and thus the junction resistance drops when the forward dc bias voltage is raised. The other RC network components (R_1C_1

and R_3C_3) of the circuit, associated with the Ni-carbon interface and silicon-Ti interface, respectively, show only small variations under different dc bias conditions. In the ideal case, each metal electrode contact should have a constant value for its resistance and capacitance, however, possible defects on the surface of carbon thin films and the backside of silicon substrates can cause such variation. In addition, possible contributions from the edges of the diode structures such as fringe capacitances or changed interfaces due to the oxygen plasma etching or direct contact with air could result in bias dependent behaviour of the interface. These local resistance components can be distinguished using ac impedance analysis, something which is impossible with dc analysis where all of the resistance components merely contribute to a single series resistance.

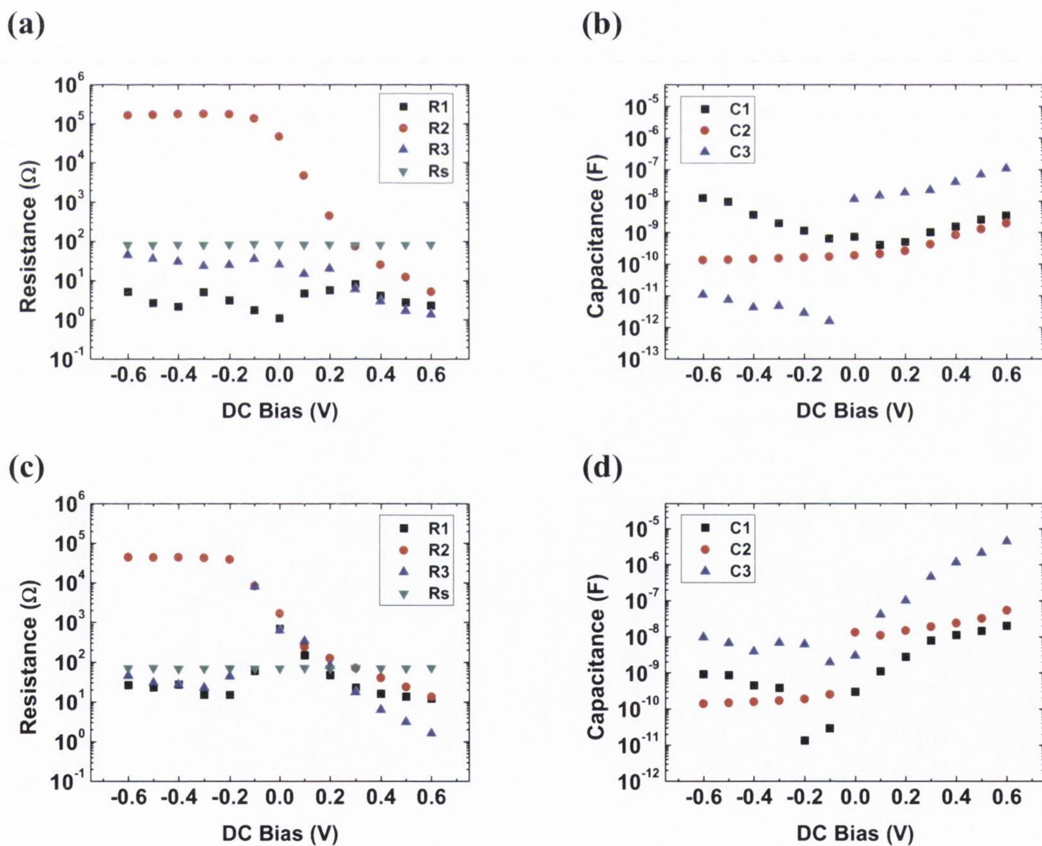

Figure 40 Resistance and capacitance values for dc bias voltages in the range of +0.6 V-0.6 V obtained from the best fit of the measured impedance spectra of the PPF/n-Si (a, b) and PyC/n-Si (c, d) SBDs using ECM 3.

Table 7 Values of R_1, C_1, R_2, C_2, R_3, C_3, R_S and L along with the applied dc bias voltages from +0.6 V to -0.6 V obtained from the best fit of the measured impedance spectra of the PPF/n-Si SBD using ECM 3.

DC Bias [V]	R_1 [ohm]	C_1 [F]	R_2 [ohm]	C_2 [F]	R_3 [ohm]	C_3 [F]	R_S [ohm]	L [H]
0.6	2.32	3.49E-09	5.37	2.02E-09	1.40	1.11E-07	84.76	4.65E-06
0.5	2.75	2.55E-09	12.59	1.33E-09	1.74	7.22E-08	84.28	4.75E-06
0.4	4.12	1.57E-09	25.81	8.65E-10	3.03	4.14E-08	84.32	4.93E-06
0.3	8.09	1.03E-09	75.80	4.39E-10	6.14	2.30E-08	82.74	5.15E-06
0.2	5.65	5.06E-10	4.60E+02	2.69E-10	20.53	1.91E-08	85.08	5.21E-06
0.1	4.66	4.11E-10	4.89E+03	2.16E-10	15.19	1.56E-08	84.75	4.03E-06
0	1.10	7.40E-10	4.77E+04	1.94E-10	26.49	1.20E-08	86.70	6.42E-06
-0.1	1.76	6.50E-10	1.39E+05	1.76E-10	36.23	1.62E-12	88.70	1.21E-05
-0.2	3.12	1.14E-09	1.78E+05	1.67E-10	25.61	2.96E-12	85.32	6.44E-06
-0.3	5.03	1.98E-09	1.81E+05	1.58E-10	24.08	4.88E-12	83.10	6.53E-06
-0.4	2.15	3.63E-09	1.77E+05	1.50E-10	31.39	4.40E-12	85.41	6.73E-06
-0.5	2.70	9.60E-09	1.72E+05	1.44E-10	37.07	7.78E-12	82.93	7.21E-06
-0.6	5.14	1.27E-08	1.66E+05	1.39E-10	45.40	1.13E-11	83.64	6.24E-06

Table 8 Values of R_1, C_1, R_2, C_2, R_3, C_3, R_S and L along with the applied dc bias voltages from +0.6 V to -0.6 V obtained from the best fit of the measured impedance spectra of the PyC/n-Si SBD using ECM 3.

DC Bias [V]	R_1 [ohm]	C_1 [F]	R_2 [ohm]	C_2 [F]	R_3 [ohm]	C_3 [F]	R_S [ohm]	L [H]
0.6	12.20	2.01E-08	13.68	5.55E-08	1.67	4.55E-06	73.42	4.79E-06
0.5	13.51	1.45E-08	24.18	3.30E-08	3.22	2.20E-06	71.73	5.03E-06
0.4	15.92	1.11E-08	41.05	2.44E-08	6.50	1.19E-06	71.56	5.27E-06
0.3	22.60	7.87E-09	72.46	1.95E-08	17.83	4.71E-07	73.02	5.49E-06
0.2	47.11	2.76E-09	1.27E+02	1.51E-08	83.25	1.05E-07	69.96	6.41E-06
0.1	147.50	1.11E-09	2.50E+02	1.12E-08	348.10	4.29E-08	72.90	1.05E-05
0	697.60	3.00E-10	1.72E+03	1.36E-08	641.90	3.11E-09	71.60	1.07E-05
-0.1	59.13	2.91E-11	8.44E+03	2.58E-10	8.31E+03	2.00E-09	70.62	1.79E-06
-0.2	14.93	1.34E-11	3.92E+04	1.92E-10	44.81	6.36E-09	71.42	5.13E-06
-0.3	15.02	3.87E-10	4.34E+04	1.73E-10	23.38	7.04E-09	70.80	6.83E-06
-0.4	27.27	4.55E-10	4.48E+04	1.61E-10	27.82	4.03E-09	70.23	8.08E-06
-0.5	23.34	8.72E-10	4.45E+04	1.51E-10	31.15	6.93E-09	73.14	5.51E-06
-0.6	26.72	9.20E-10	4.49E+04	1.42E-10	46.91	9.97E-09	72.38	9.24E-06

Using the capacitance values (C_2) corresponding to the Schottky contact of the devices derived from the impedance spectra, plots of $1/C^2$ against the reverse dc bias voltage can be obtained for each carbon-silicon SBD device, giving information on the built-in potential and the barrier height of the Schottky contact.[157] In general, capacitance measurements are widely used for determining the built-in potential in M-S contacts by analysis of the C-V characteristics. However, it has been revealed that the presence of series resistances in structures with potential barriers can have a significant effect on the measured capacitance with conventional capacitance measurements. Thus, differing from the true barrier capacitance, an ac analysis method based on IS is proposed to prevent errors arising from series resistances.[181] According to the C-V relationship at the depletion layer of a metal-semiconductor M-S contact, $1/C^2$ and V have a linear relationship and the intercept value (V_i) of the x axis can be found from plots based on the following equation,[157]

$$\frac{1}{C^2} = \left(\frac{2}{\varepsilon_S q N_d}\right)(V_i - V), \qquad (3.17)$$

$$V_i = V_{bi} - \left(\frac{k_B T}{q}\right), \qquad (3.18)$$

where ε_S is the permittivity of the silicon substrate, N_d is the silicon dopant concentration and V_{bi} is the built-in potential of the Schottky contact. $1/C^2$ vs. V plots for the devices are shown in Figure 41 and they give built-in potential values of 0.62 ± 0.01 V for the PPF/n-Si SBD and 0.32 ± 0.01 V for the PyC/n-Si SBD. In addition, the value of the Schottky barrier height can be calculated using the equation below[157]

$$\varphi_B = V_{bi} + \frac{(E_C - E_F)}{q} = V_{bi} + \left(\frac{k_B T}{q}\right)\left[\ln\left(\frac{N_c}{N_d}\right)\right], \qquad (3.19)$$

where E_C is the energy of the conduction band edge, E_F is the energy of the Fermi level and N_c is the effective density of states in the conduction band of n-type silicon. The determined barrier heights from Eq. (3.19) are 0.91 ± 0.01 eV for the PPF/n-Si SBD and 0.61 ± 0.01 eV for the PyC/n-Si SBD, respectively. When comparing the values of the Schottky barrier height from the C-V characteristics to the values from the J-V results (which are 0.78 eV for the PPF/n-Si SBD and 0.49 eV for the PyC/n-Si SBD) there is a slight discrepancy with a shift of 0.12 – 0.13 eV to higher values in both cases, which means that the PPF/n-Si SBD has a barrier 0.3 eV higher than the PyC/n-Si SBD. The discrepancy may stem from the presence of an insulating layer or charges exiting at the carbon-silicon interface,[182] however this is not clearly visible in the cross-sectional TEM images. A thin oxide or insulating layer can form at the junction of Schottky

diodes unless all the processing is done in high vacuum.[182] In our case this is more likely to occur for the PyC SBD, as the carbon deposition takes place in a high temperature environment, as opposed to the PPF, which is spun on at room temperature prior the high temperature anneal, protecting the interface from oxidation. Furthermore, using the thermionic emission model to calculate the barrier height neglects contributions from deep levels which possibly occur in the silicon band gap and image force lowering, meaning the *J-V* results yield an underestimated barrier height. The present method reveals that detailed analysis of the electrical characteristics can result in an understanding of the electrical properties of various carbon nanostructures and this could be extended to further material sets and their interfaces.

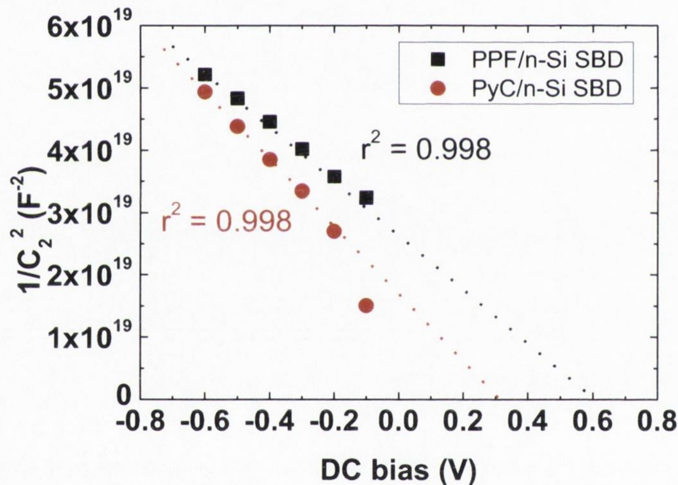

Figure 41 The plot of $1/C^2$ vs. V for the PPF/n-Si and PyC/n-Si SBDs with C_2 values derived from the simulated results using ECM 3.

3.1.7 Conclusion

The electrical properties of carbon-silicon Schottky contacts in high performance SBD devices have been explored using both dc *J-V* measurements and ac impedance measurements. Two different conductive carbon thin films, PPF and PyC, were employed to create new types of Schottky diodes with n-type silicon substrates. Diode parameters including the ideality factor, the Schottky barrier height and the series resistance were extracted on the basis of thermionic emission theory from dc *J-V* measurements. In addition, a more detailed investigation of the Schottky contact with

IS analysis under various dc biases has been carried out. An equivalent circuit model of the SBD taking into account second-order effects such as capacitance from the metal electrode contacts and parasitic inductance has been proposed to identify the built-in potential and the barrier height values at the Schottky junction. The electrical characteristics of the Schottky contact between the carbon thin films and the silicon substrates were verified using RC values extracted from the equivalent circuit model. Thus IS can be utilised for the evaluation and the simulation of Schottky contacts and allows for a better understanding of interfaces on a fundamental level.

3.2 Graphene-Silicon Schottky Contacts[§]

3.2.1 Background

Graphene is considered one of the most promising candidates for future industry applications because of its extraordinary properties.[11,55,58] Thus far it has drawn enormous attention from various research fields and intensive studies on its characteristics have been performed.[1,183-185] Based on its unique electrical properties, a number of works on electronic device applications[28,72,186-188] have been carried out. Its high conductivity makes it potentially suitable for replacing traditional metal electrodes in diodes, which results in the formation of a Schottky contact with various semiconducting materials.[170,189] In particular, the graphene-semiconductor Schottky contact structure has recently been employed in graphene-based devices such as solar cells,[190,191] barristors[192] and sensors.[193] Therefore, the investigation of Schottky contacts between graphene and semiconductors, which is the simplest but one of the most widely used structures in graphene-based devices, can be considered an important topic in graphene device application research. It is therefore essential to define the electrical characteristics of graphene-semiconductor interfaces in order to comprehensively understand the current transport mechanism at the interface.

In this work, graphene-silicon (G-Si) Schottky barrier diodes (SBDs) were fabricated and the interface between graphene and silicon was electrically characterised using dc current-voltage (*J-V*) measurements and ac impedance spectroscopy (IS) analysis. IS has primarily been used to study the charge carrier transport mechanism in organic semiconductor devices and solar cells[149,153] and measured impedance spectra can be electrically interpreted with a proper equivalent circuit model.[194] It is difficult to obtain reliable junction capacitance values for SBD devices using the traditional *C-V* method particularly when the devices have a high series resistance. It has been shown that the existence of series resistance in a diode device can cause considerable errors in calculation of the diode parameters,[181,195] but, in practice, it is not possible to make a SBD device without any series resistance. Here IS was used to obtain capacitance values at the junction as this gives more reliable values than the traditional *C-V* method, particularly for microscopic systems with varying series resistances. IS has

---

[§] Parts of this chapter appeared in P-5.

recently been applied to the analysis of the metal-semiconducting nanowire contacts and the interface of carbon-silicon SBD devices with series resistance.[163,194] In this study IS was employed for the investigation of the interface of G-Si SBD devices for an accurate analysis of the Schottky junction and to extract information about the interface between silicon and graphene.

3.2.2 Graphene Growth

Graphene was produced using CVD,** as described in detail elsewhere.[94] The graphene was grown on 25 μm Cu foils in a quartz tube furnace. The growth temperature was 1035 °C, and high purity methane (CH_4) was used as the hydrocarbon precursor with a supply of hydrogen.

A typical process for CVD graphene growth is as follows. Cu foil pieces which were rinsed using acetone and isopropyl alcohol were placed on a quartz shovel. The shovel was then inserted into the quartz tube of the furnace and the tube was evacuated by a vacuum pump. Hydrogen flow (typically 100 sccm) was established in the furnace by turning on an MFC at the inlet port, and the quartz tube was heated at a rate of 850 °C/hour to reach 1035 °C under hydrogen flow. After annealing for 60 minutes, the precursor (CH_4) flow started at a flow rate of 10 sccm with hydrogen flow (5 sccm). After a set of dwell time (20 minutes), the precursor flow was stopped, hydrogen flow was reduced to 2.5 sccm and the power supply of the heating element was turned off. When the temperature of the furnace was reduced to ~800 °C, the furnace was forcibly cooled by compressed air to room temperature.

** Graphene was prepared by Dr. Niall McEvoy.

3.2.3 Device Fabrication

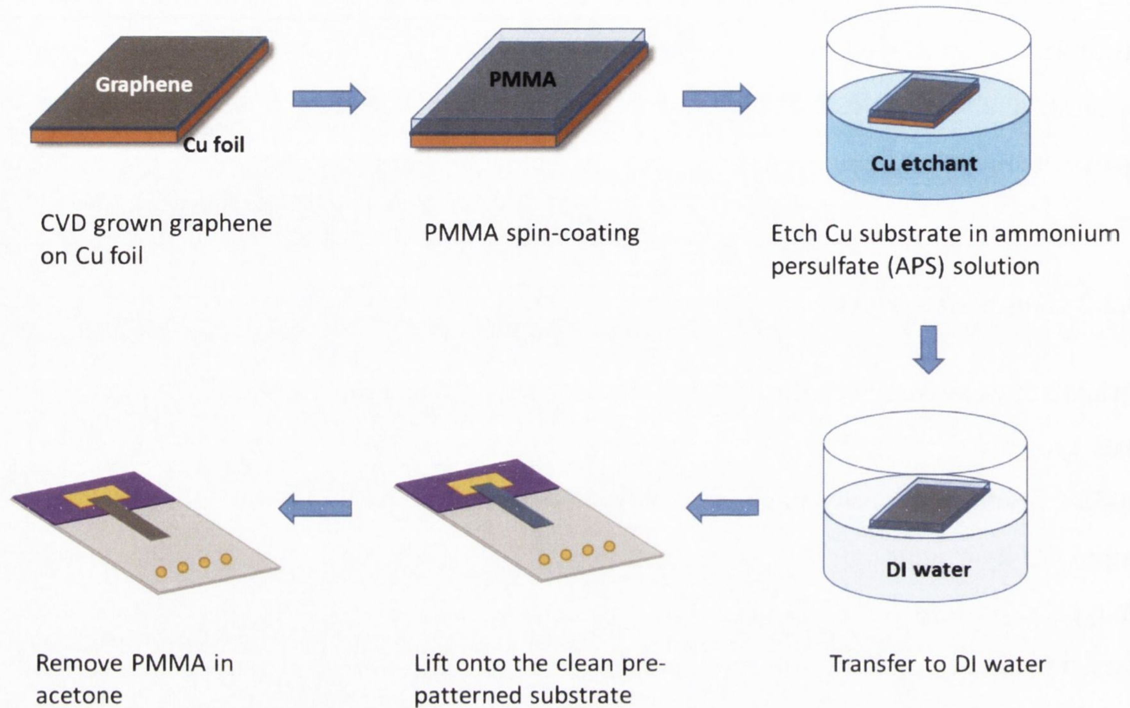

Figure 42 Process flow of graphene transfer onto the pre-patterned substrate using a polymer-supported transfer method.

A thermally grown silicon dioxide (SiO_2) layer (150 nm thick) on an n-Si wafer with a dopant (phosphorus) concentration of 5×10^{14} cm^{-3} and <100> orientation was used as a substrate for the device. Part of the SiO_2 layer was completely removed by a wet etching process with 3 % diluted hydrofluoric acid (HF) for 10 minutes, followed by rinsing with deionised water and drying. Using a shadow mask, titanium (Ti) and gold (Au) metal electrodes (Ti/Au = 20/80 nm) were sputtered on the top centre of the remaining SiO_2 layer and the exposed n-Si area, and a good ohmic contact was achieved between Ti and n-Si. The graphene was then transferred onto the pre-patterned substrate using a polymer-supported transfer method, directly after removing the native oxide layer from the exposed silicon surface with HF, in order to form a direct contact between the graphene and the silicon. One end of the graphene lies on the n-Si surface without touching the metal electrode deposited on the n-Si and the other end sits on the gold pad on the SiO_2 layer which prevents a direct contact between the metal electrode and the Si substrate. A detailed schematic of the transfer process is presented in Figure 42.

3.2.4 Film Characterisation

Raman Analysis: A photograph of the fabricated G-Si SBD device and its schematic diagram are depicted in Figure 43(a). The device has an effective interface area of ~0.2 cm^2 as measured by optical microscopy. Figure 43(b) shows a Raman spectrum of the graphene on the SiO_2 part of the device which was obtained by averaging over 6400 scans taken over a 20 × 20 μm area.[††] It has a large 2D (at 2670 cm^{-1}) to G (at 1580 cm^{-1}) peak intensity ratio (I_{2D}/I_G) which is approximately 3, clearly indicating that the graphene has a monolayer thickness. There is only a very small D-peak contribution underlining the high quality of the graphene.

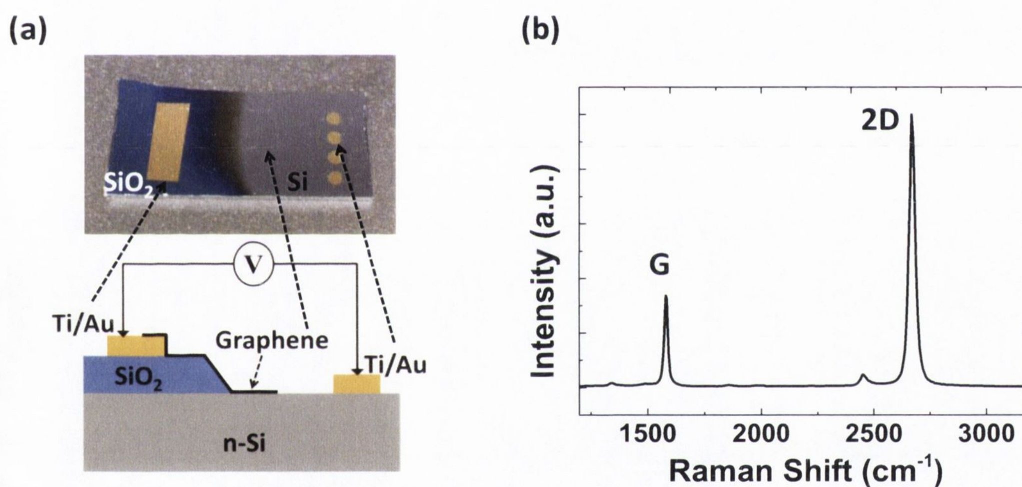

Figure 43 (a) Photograph of the G/n-Si SBD device (top) and its schematic diagram (bottom). (b) Average Raman spectrum of high quality graphene on the SiO2 layer of the device.

The area probed is shown in Figure 44(a), from this image it is evident that the film is mostly homogenous with some small darker spots corresponding to regions of multilayer island nucleation, which are often seen in CVD grown graphene. Maps of the D, G and 2D band intensity over this area are shown in Figure 44(b), (c) and (d), respectively. The G band intensity map indicates that the surface is mostly uniform, with some spots of high intensity stemming from the secondary nucleation sites. Similarly, the 2D band map is quite uniform, however in the regions of secondary nucleation the 2D band intensity is typically suppressed due to the thicker nature of the

[††] Raman spectroscopy was performed with the assistance of Dr. Niall McEvoy.

graphene present. Two of the secondary islands visible display higher 2D band intensity than the monolayer background, suggesting that these particular islands are not AB stacked. The D band intensity map indicates that defects present stem from either contributions from these secondary islands, which will have significant edge contributions, or from what appear to be the boundaries between different laterally growing crystallites.

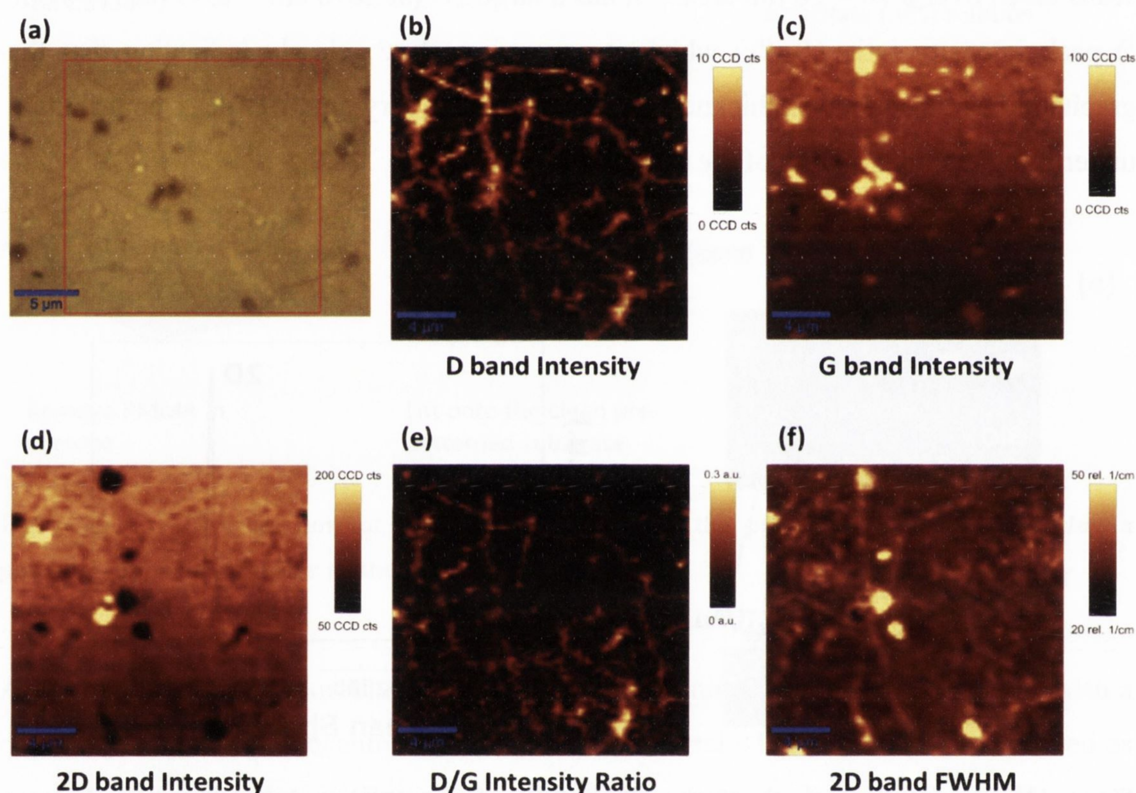

Figure 44 (a) Optical micrograph of area of graphene scanned. Raman maps of (b) D band intensity, (c) G band intensity, (d) 2D band intensity, (e) D/G intensity ratio and (f) Lorentzian fit of 2D band FWHM were extracted.

The D/G intensity ratio map shown in Figure 44(e) indicates that these defect contributions are relatively low. A map of the full width at half maximum (FWHM) of the 2D band is shown in Figure 44(f). This indicates that the 2D FWHM is typical uniform and rather narrow (~ 30 cm^{-1}) except for in the regions of secondary crystallite nucleation. The 2D band for monolayer graphene can be well fitted with a single Lorentzian peak, whereas that of bilayer graphene consists of four distinct contributions and as more layers are added the 2D band shape trends towards that of bulk graphite.[142]

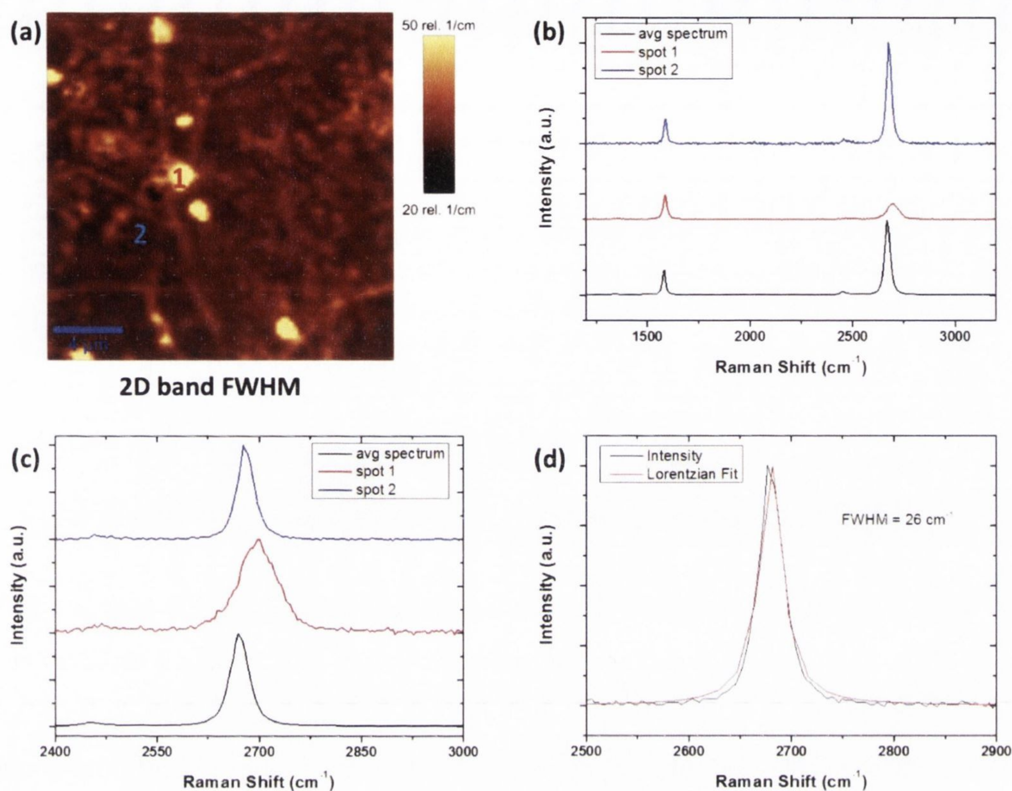

Figure 45 (a) 2D FWHM Raman map marked with spots 1 and 2 from which point spectra were extracted. (b) Average Raman spectrum of the sample as well as point spectra from spots 1 and 2, normalized to the G band intensity. (c) Average Raman spectrum of the sample as well as point spectra from spots 1 and 2 normalized to the 2D band intensity so as to highlight the change in 2D band shape and FWHM. (d) Lorentzian fitting of the 2D band for spot 2 indicating a FWHM of 26 cm^{-1}.

Table 9 Summary of peak intensity ratio (I_{2D}/I_G), peak position and FWHM for the 2D and G band in Figure 45(b).

	I_{2D}/I_G	G peak position [cm^{-1}]	2D peak position [cm^{-1}]	G peak FWHM [cm^{-1}]	2D peak FWHM [cm^{-1}]
Average	2.96	1582	2671	17	30
Spot 1	0.64	1589	2697	20	60
Spot 2	4.01	1591	2680	16	26

Individual spectra, extracted from the Raman maps shown in Figure 44, representing monolayer and multilayer regions, are shown in Figure 45. In Figure 45(b) it is evident that regions of high 2D FWHM correspond to multilayer growth, with a broadened

non-Lorentzian 2D band and a low 2D/G intensity ratio. Detailed information including peak intensity ratio, peak position and FWHM for the 2D and G band in Figure 45(b) is summarised in Table 9. The change in shape and width of the 2D band in these regions is emphasised in Figure 45(c). These small regions of multilayer growth have the effect of broadening the 2D FWHM in the average spectrum acquired over the scan area. However, individual spectra can be well fitted with a single Lorentzian of FWHM < 30 cm^{-1} as shown in Figure 45(d). This indicates that the graphene is predominantly monolayer.

3.2.5 Current-Voltage Measurement

The dark *J-V* measurement data of the graphene/n-Si (G/n-Si) SBD device are plotted in Figure 46, which shows typical rectifying behaviour. As described in Chapter 3.1, the relationship between the current density (J) of the diode and the voltage drop across the junction (V_D) of the Schottky junction can be described using thermionic emission theory.[157] When considering the effect of the series resistance of the system, which can stem from the resistance of the graphene and Si substrate, the contact resistances to the metal electrodes and interface states at the junction, Eq. (3.5) is adopted to characterise dc *J-V* measurement data. By applying Cheung's method[180] which is used in Chapter 3.1, diode parameters such as the ideality factor (n) and the barrier height ($q\varphi_B$) can be extracted. The plots of $dV/d(\ln J)$ vs. J and $H(J)$ vs. J for the G/n-Si SBD are presented in Figure 47, giving the values of $n = 1.38 \pm 0.02$ and $q\varphi_B = 0.69 \pm 0.01$ eV. Such a low ideality factor value, which is close to the unity, indicates that this G/n-Si SBD performs well as a rectifier. Compared to other previous graphene-silicon SBDs,[190,191,193] this device shows the lowest reported value of ideality factor. The ideality factor and Schottky barrier height (SBH) values of different SBDs are summarised in Table 10. The SBH values of G/n-Si SBDs are distributed between 0.7 – 0.8 eV and the small variation of the SBH values can arise from various factors including non-ideal surface conditions of graphene-silicon interfaces, unintentionally doping of graphene during the processing steps and different Si doping level of the devices.

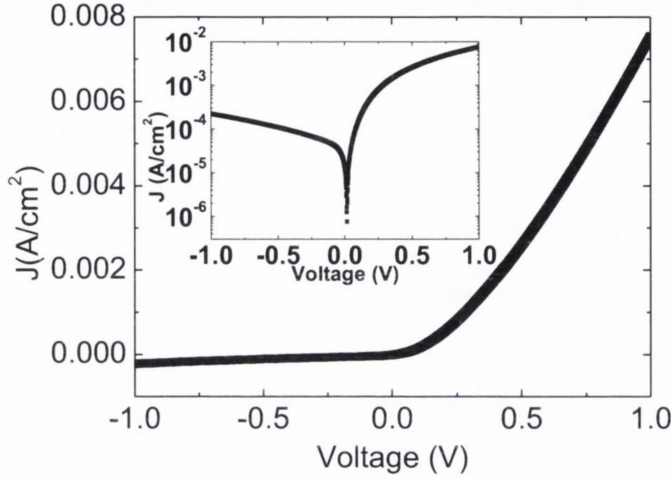

Figure 46 **Dark *J-V* measurement of the G/n-Si SBD on a linear scale. Inset: *J-V* curve on a semi-logarithmic scale.**

In general, the ideality factor higher than the unity observed in real SBDs can be attributed to several factors such as the image force lowering effect, additional thermally assisted carrier tunnelling at the junction, bias dependent SBHs, and Schottky barrier inhomogeneity in the junction area.[196,197] In the case of G-Si SBDs, it is known that charge puddles can be formed unintentionally during the graphene synthesis or transfer process, which causes Schottky barrier inhomogeneity at the interface. These factors can be quantified by calculating the flat band barrier height (φ_{BF}), where the influence of such factors on the evaluation of *J-V* data does not exist, so it can be used as a fundamental value for the comparison between experimental and theoretical data.[198,199] φ_{BF} can be calculated by using

$$\varphi_{BF} = n\varphi_B - (n-1)\left(\frac{k_B T}{q}\right)\ln\left(\frac{N_c}{N_d}\right), \qquad (3.20)$$

where N_c is the effective density of states in the conduction band and N_d is the carrier density. Using this equation, the calculated value of $q\varphi_{BF}$ is found to be 0.84 eV, which is larger than $q\varphi_B$ from the *J-V* measurement data.

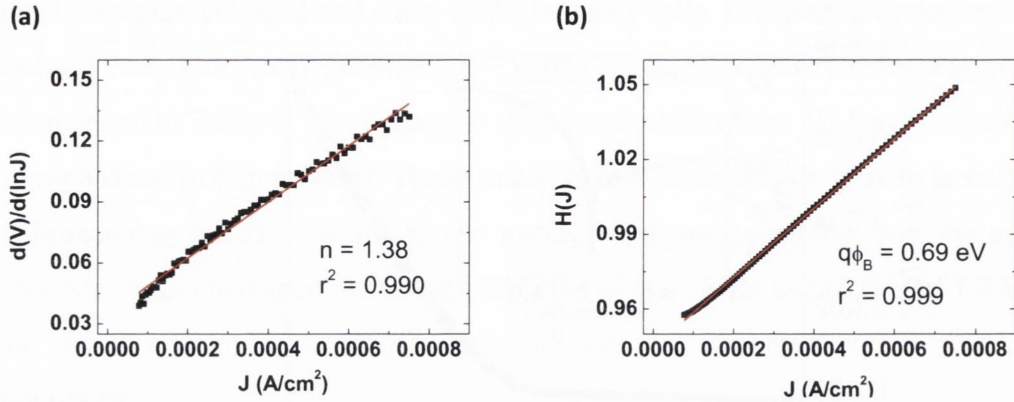

Figure 47 **Plots of** $dV/d(\ln J)$ **vs.** J **and** $H(J)$ **vs.** J **for the G/n-Si SBD.**

Table 10 **Summary of the ideality factor (*n*) and SBH ($q\varphi_B$) values of different graphene-silicon SBDs.**

Graphene	Si type and doping density	*n*	$q\varphi_B$ [eV]	Reference
CVD grown monolayer	n-type Si, 1.5×10^{15} cm^{-3}	1.57	0.75	ref[190]
CVD grown monolayer	n-type Si, 8.0×10^{14} cm^{-3}	1.60 – 2.00	0.79	ref[191]
CVD grown monolayer	n-type Si, 5.0×10^{14} cm^{-3}	1.41	0.74	ref[193]
CVD grown monolayer	n-type Si, 5.0×10^{14} cm^{-3}	1.38	0.69	this work

3.2.6 Impedance Spectroscopy Measurement

Impedance spectra of the G/n-Si SBD device were obtained in the frequency range of 0.1 Hz to 1 MHz with an ac voltage of 10 mV under various dc biases (from -0.6 to +0.6 volts with a step of 0.1 V) at room temperature. Figure 48(a) and (b) show Nyquist impedance plots of the G/n-Si SBD under forward, zero and reverse dc bias. The radius of the semicircles, which is related to the total impedance of the device, increases as the dc bias decreases in the forward bias region while it shows a clear upsurge in diameter in the zero and reverse bias regions. This means the impedance value of the device is dependent on the applied dc bias and it has a much larger value under reverse bias than forward bias. The nearly semi-circular shape of the impedance spectra over the whole dc bias range indicates that the Schottky junction can be expressed using an equivalent circuit model which is composed of a combination of resistance and capacitance (RC) networks.[161]

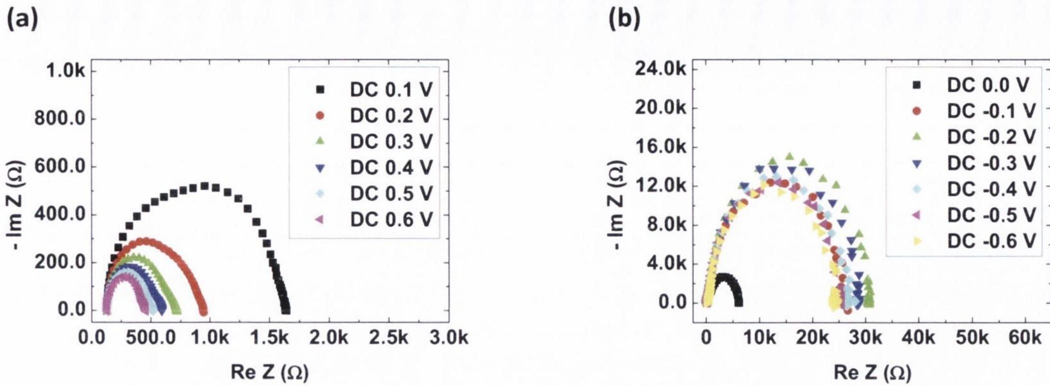

Figure 48 Nyquist plots of the G/n-Si SBD under (a) forward, (b) zero and reverse dc bias.

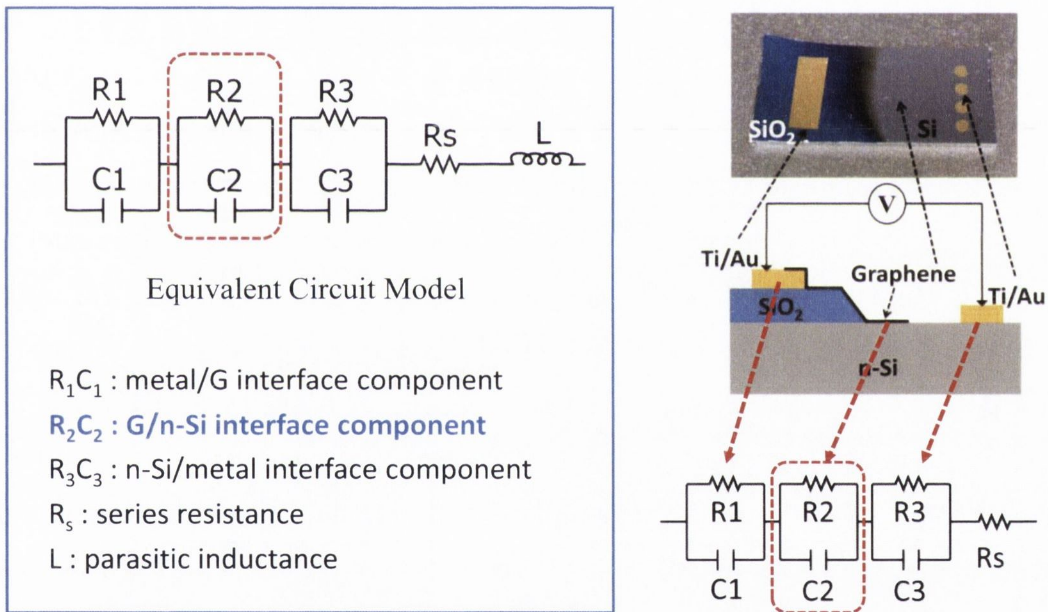

Figure 49 Equivalent circuit model of the G/n-Si SBD for the IS analysis where R_1C_1, R_2C_2 and R_3C_3 represent the RC networks related to the interfaces of Au-graphene, graphene-Si and Si-Ti respectively. R_S is the series resistance and L represents a parasitic inductance associated with the electrical leads.

As explained in Chapter 3.1, a typical equivalent circuit model of a Schottky junction consists of a parallel connected RC network and a series resistance which is serially connected to the RC network. The RC network represents the space charge region and the series resistance accounts for the contact and bulk resistance of the device, respectively, showing a perfect semi-circular Nyquist impedance plot. However, the

plots of Figure 48(a) and (b) do not have perfect semi-circular shapes. This implies there is more than one RC component in the system where the contact area of each metal electrode can cause extra capacitive components in the device. Therefore, a more complex equivalent circuit model which was introduced in Chapter 3.1 was used for the analysis of the impedance spectra,[194] where the influence of the contacts between the Au pad and the graphene sheet, and the Ti/Au electrode and the n-Si substrate are taken into account. The equivalent circuit model and schematic of the device structure associated with the model is presented in Figure 49. It has three RC pairs in series connected with a series resistance (R_S) and a parasitic inductance (L). C_1, C_2 and C_3 are the capacitances related to the Au-graphene, graphene-Si and Si-Ti interfaces, respectively with corresponding shunt resistances R_1, R_2 and R_3.

Mathematical analysis of the equivalent circuit model in Figure 49 and fitting it with the experimental data were carried out using Eq (3.10), Eq. (3.15) and Eq. (3.16) in order to find values of RC components.[161] The fitted curves, with experimental data obtained under various dc biases using these equations, are depicted in Figure 50(a) – (d), showing a good fit with each other. The resistance and capacitance values extracted from the best fit of the experimental impedance data are plotted in Figure 51(a) and (b) with a semi-logarithmic scale for the G/n-Si SBD device, and detailed data are presented in Table 11. While the series resistance, R_S, is constant over the whole bias region with an average value of 130.1 ± 0.7 Ω, R_2 shows a significant change as the dc bias varies from the forward to reverse region. It has very high values compared to the other resistances in the reverse dc bias region, and it can be conceived that the R_2C_2 component of the equivalent circuit model is related to the Schottky barrier at the G/n-Si interface because R_2 suppresses the current flow at the junction under reverse dc bias. When a forward dc bias is applied, it suddenly drops dramatically with increasing bias voltage. This can be explained by considering that more current can flow through the Schottky junction since the barrier is lowered by the forward bias, leading to a drop in the junction resistance.

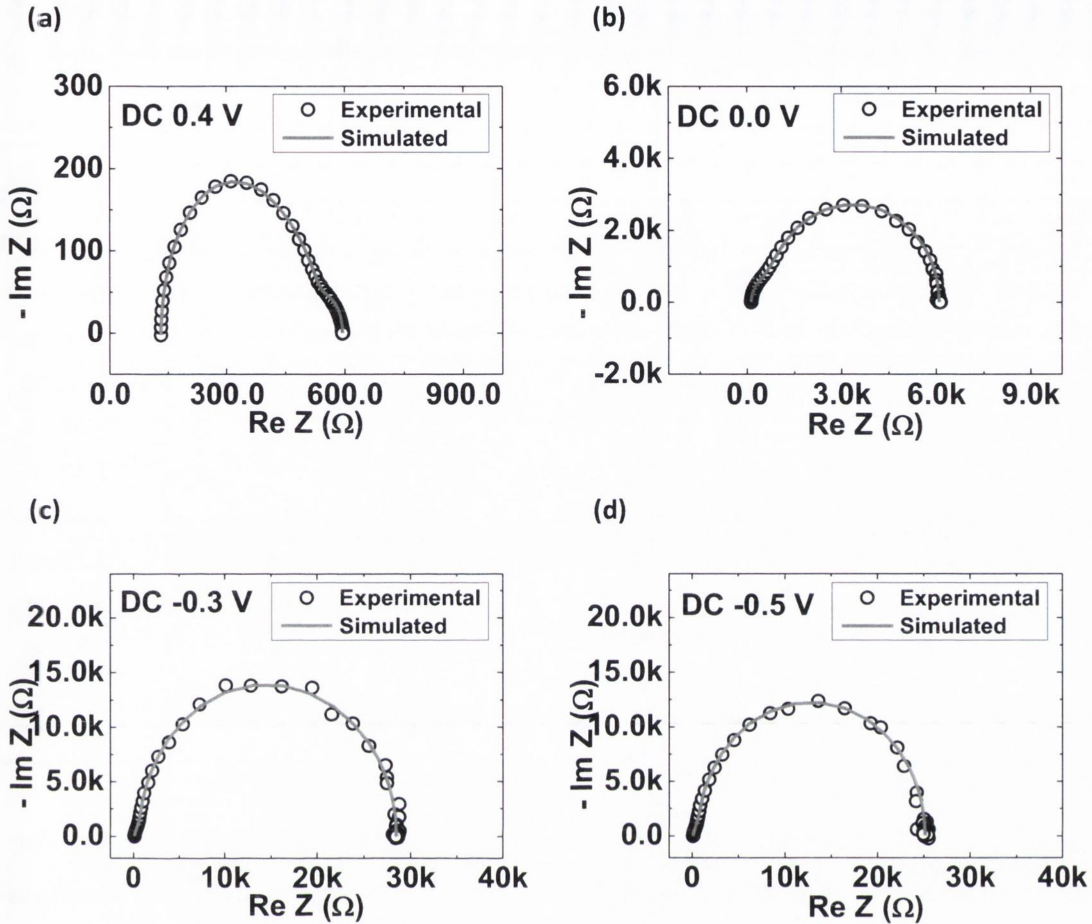

Figure 50 Nyquist plots and corresponding fit from the equivalent circuit model on the G/n-Si SBD under dc bias of (a) +0.4 V, (b) 0.0 V, (c) -0.3 V and (d) -0.5 V.

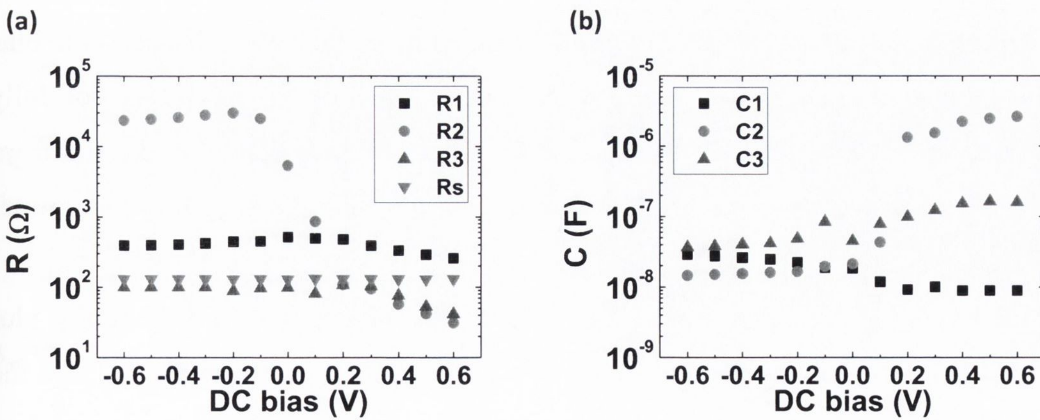

Figure 51 Semi-logarithmic plots of (a) resistance and (b) capacitance values for dc bias voltages in the range of +0.6 V to -0.6 V achieved from the best fit of the impedance spectra of the G/n-Si SBD using the equivalent circuit model of Figure 49.

Table 11 Values of R_1, C_1, R_2, C_2, R_3, C_3, R_S and L along with the applied dc bias voltages from +0.6 V to -0.6 V obtained from the best fit of the measured impedance spectra of the G/n-Si SBD using the equivalent circuit model of Figure 49.

DC Bias (V)	R_1 (Ω)	C_1 (F)	R_2 (Ω)	C_2 (F)	R_3 (Ω)	C_3 (F)	R_s (Ω)	L (H)
0.6	256.1	8.91E-09	31.3	2.64E-06	41.7	1.62E-07	129.7	3.33E-06
0.5	288.1	8.86E-09	42.2	2.48E-06	53.2	1.65E-07	129.6	3.34E-06
0.4	330.4	8.88E-09	57.3	2.25E-06	76.3	1.54E-07	129.7	3.34E-06
0.3	388.3	1.01E-08	94.5	1.55E-06	103.2	1.24E-07	129.8	3.30E-06
0.2	478.6	9.18E-09	108.6	1.33E-06	107.9	9.90E-08	129.9	3.28E-06
0.1	492.4	1.19E-08	856.2	4.34E-08	80.9	7.92E-08	132.0	3.20E-06
0	513.5	1.84E-08	53.5E+02	2.14E-08	99.2	4.53E-08	129.6	3.37E-06
-0.1	449.9	1.88E-08	24.9E+03	1.96E-08	96.8	8.45E-08	130.1	3.30E-06
-0.2	442.8	2.25E-08	29.9E+03	1.66E-08	88.6	4.86E-08	129.6	3.35E-06
-0.3	418.9	2.47E-08	27.8E+03	1.60E-08	99.8	4.21E-08	129.8	3.38E-06
-0.4	402.6	2.61E-08	25.9E+03	1.55E-08	99.7	4.04E-08	130.0	3.36E-06
-0.5	397.1	2.75E-08	24.5E+03	1.51E-08	99.9	3.83E-08	130.4	3.29E-06
-0.6	390.3	2.87E-08	23.5E+03	1.46E-08	99.9	3.67E-08	130.6	3.28E-06

The other RC network components (R_1C_1 and R_3C_3) of the model, related to the Au-graphene contact and the Ti-Si contact, respectively, show relatively small variation over the whole dc bias region with an average contact resistance value of 403.8 ± 21.2 Ω for R_1 and 88.2 ± 5.6 Ω for R_3. In the ideal case, the interfaces at the Au-graphene and Si-Ti contacts should not be influenced by the external bias, however, imperfect surface conditions such as possible defects at the interfaces can give rise to such variation in a practical case. Even though the detailed mechanism which causes the bias dependent behaviour at the metal electrode contact area of the device is not fully understood, IS makes it possible to separate the effect of each electrode contact from the whole capacitive component of the device and quantify it using the proper equivalent circuit model.

Using the depletion capacitance (C_2) of the Schottky junction, a Mott-Schottky plot ($1/C^2$ vs. V) can be established and information on the built-in potential (V_{bi}) and the SBH ($q\varphi_B$) of the device at the junction can be derived.[157] The Mott-Schottky plot of the G/n-Si SBD is shown in Figure 52. The V_{bi} can be determined by linear extrapolation of the intercept with the x axis (dc bias), giving values of V_{bi} = 0.54 ± 0.04 V and a calculated value of $q\varphi_B$ = 0.82 ± 0.04 eV. The value of SBH obtained from the Mott-Schottky plot is not fully consistent with the value from the previous J-V

data ($q\varphi_B$ = 0.69 eV), showing an increase of 0.13 eV. This discrepancy may stem from the possible presence of a thin insulating layer at the G-Si interface and/or Schottky barrier inhomogeneity.[191,195,197] The value of SBH from the Mott-Schottky plot is in excellent agreement with the above calculated flat band barrier height ($q\varphi_{BF}$ = 0.84 eV), underlining the fact that IS results in a more accurate parameter extraction on the SBH of the device than the dc *J-V* measurement method. However, it should be noted that while a dc *J-V* measurement method is mainly utilised to define the current transport mechanism at the junction and the ideality factor representing the performance of diodes, an ac IS measurement method has merit for the characterisation of the space charge region at the junction and it can localise the effect of metal electrode contacts from the system, therefore, they are complementary for the study of the interface of SBDs.

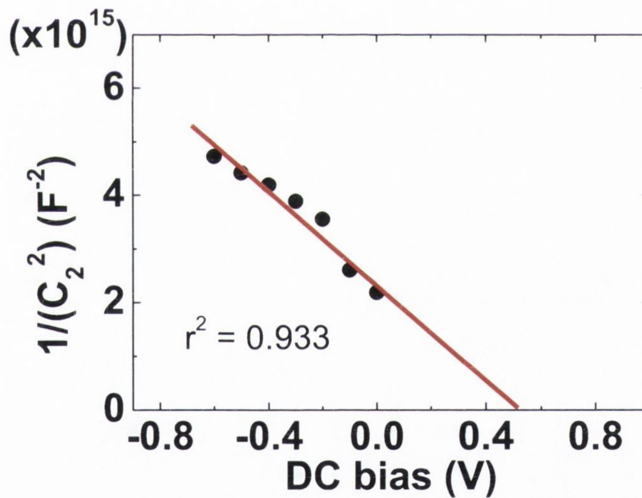

Figure 52 Mott-Schottky plot ($1/C^2$ vs. V) of the G/n-Si SBD with C_2 values extracted from the simulated results using the equivalent circuit model of Figure 49.

3.2.7 Conclusion

G/n-Si SBDs were fabricated and investigated using dc *J-V* and ac IS measurements. An ideality factor of 1.38 and a SBH of 0.82 eV were extracted from the experimental data. The IS method was utilised to obtain a more reliable SBH value using a proper equivalent circuit model for the analysis. It is expected that this kind of approach to the investigation of graphene-based nanoscale devices will allow the interface of the

devices to be interpreted in a more comprehensive and detailed way. This is of particular importance because most graphene SBDs are not completely free from the effect of metal electrode contacts and also the graphene-semiconductor interfaces may not be ideal. Thus, this study will facilitate graphene-based device developments, particularly for diodes, sensors and solar cells.

4. Heterojunction Hybrid Devices from Vapour Phase Grown MoS_2[‡‡]

4.1 Background

Molybdenum disulfide (MoS_2) is considered to be a promising material for future electronic devices because of its fascinating electronic and optical/optoelectronic properties.[61,106-108] Many recent studies have been based on mechanically exfoliated MoS_2 flakes with e-beam defined contacts in a 3-terminal field effect transistor (FET) configuration. These investigations focused on field-induced charge carrier movements, however, photoconductivity measurements at the junction between layered MoS_2 and conventional semiconducting substrates have rarely been conducted, which may be due to the lateral size limit of mechanically exfoliated flakes.[200] Recently, large-area growth techniques based on vapour phase sulfurisation of thin Mo films have been adopted for the synthesis of MoS_2 thin films.[125,201]

In this work, p-n heterojunction diodes fabricated by transferring vapour phase grown n-type MoS_2 thin films onto p-type silicon (p-Si) substrates are introduced. In the previous chapter it was shown that high quality diodes can be created by transferring monolayer graphene onto pre-patterned silicon substrates.[193,202] In a similar fashion, MoS_2 layers of varying thicknesses are transferred forming a vertical hybrid device. This design allows the MoS_2 film to be directly exposed to light. The effect of varying the incident light intensity, wavelength and MoS_2 film thickness was investigated. The devices produced here display extraordinary sensitivity to changes in illumination. The spectral response showed a very broad spectrum with contributions from indirect and direct band gap transitions.

4.2 MoS_2 Synthesis

MoS_2 thin films were synthesised using a vapour phase sulfurisation process.[§§125,201,203] Mo films of varying thickness were deposited on SiO_2/Si substrates using a Gatan Precision Etching and Coating System (PECS), where the Mo film deposition rate ($<$ 0.1 nm/s) and thickness were monitored using a quartz crystal microbalance.

‡‡ Parts of this chapter appeared in P-1.

§§ MoS_2 films were prepared by Maria O'Brien.

Sulfurisation of the Mo samples took place in a quartz tube furnace consisting of two different heating zones. The sputtered films were placed in a zone which was heated to 750 °C and annealed for 30 minutes at a pressure of ~1 Torr under an argon (Ar) flow of 150 sccm. Sulfur powder was heated to its melting point (113 °C) in a second upstream zone of the furnace, and the generated sulfur vapour was supplied to the Mo films, where it reacted to produce MoS_2. This technique yielded a continuous multilayer of MoS_2. A schematic diagram of the process is presented in Figure 53.

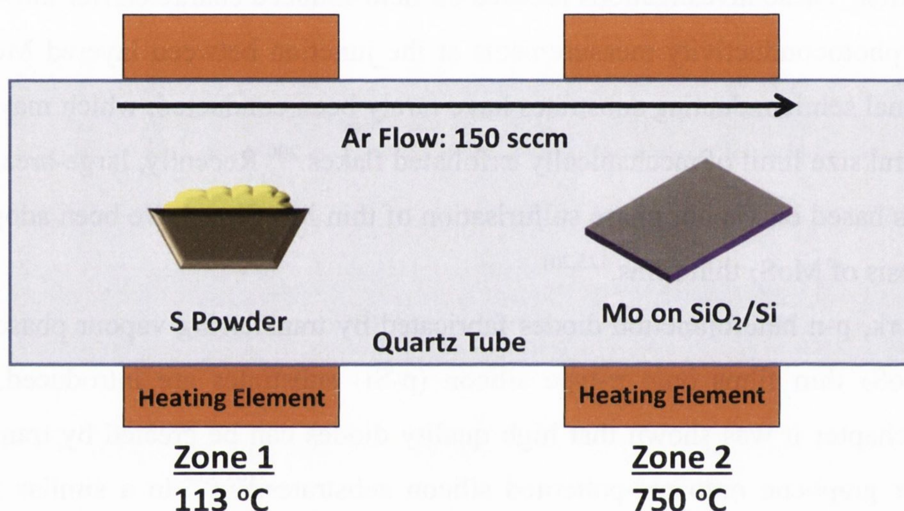

Figure 53 Schematic diagram of the vapour phase sulfurisation process used for MoS_2 thin film synthesis.

4.3 Film Characterisation

4.3.1 Thickness Measurements

Thickness measurements of MoS_2 thin films were carried out using a spectroscopic ellipsometry (SE) tool (Alpha SE, J. A. Woollam Co., Inc.) operating in the wavelength range of 380 – 900 nm at an angle of incidence of 70 ° with a beam spot size of ~40 mm^2. SE data were analysed using CompleteEASE 4.72 (J. A. Woollam Co., Inc.).
The thicknesses of the MoS_2 films were found to be 4.17 ± 0.18, 8.26 ± 0.29, 12.52 ± 0.26 and 15.96 ± 0.16 nm, respectively, by spectroscopic ellipsometry (SE).[203] A four-layer optical model which consists of a Si substrate, an interface layer between Si and

SiO_2, a SiO_2 layer and a MoS_2 layer was built to analyse the SE spectra. A newly developed material dispersion for MoS_2 using a Tauc-Lorentz oscillation model was used to determine the thicknesses of the MoS_2 thin films.[176,203] More details on SE modelling procedure can be found in Appendix A.1.

4.3.2 Raman Analysis

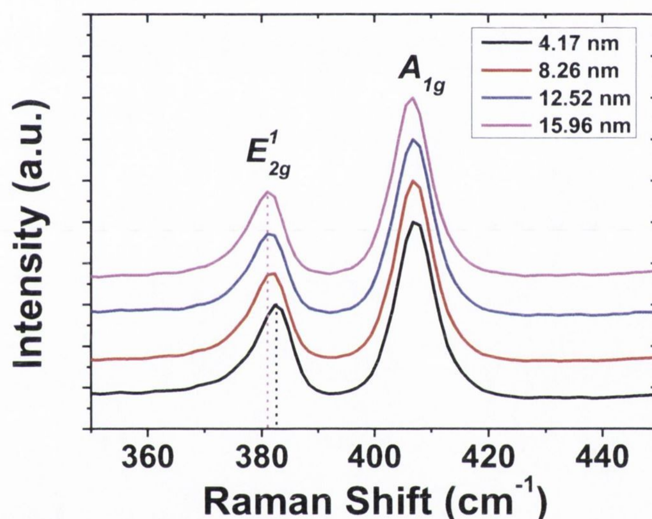

Figure 54 **Raman spectra of the MoS_2 thin films with various thicknesses grown by vapour phase sulfurisation of Mo thin films. A slight shift of the E^1_{2g} band is evident.**

Raman spectra were used to assess the quality of the MoS_2 films, as shown in Figure 54.*** Raman spectra were obtained with a Witec Alpha 300 R confocal Raman microscope, using an excitation wavelength of 532 nm with a power of < 1 mW and a spectral grating with 1800 lines/mm. The spectra all show the characteristic signal of 2H-MoS_2 with no obvious contributions from carbon contamination, polymer residue or oxides. The positions of the E^1_{2g} (~383 cm^{-1}) and A_{1g} (~408 cm^{-1}) peaks of the MoS_2 films, which are related to in plane and out of plane vibrational modes, respectively, are labelled for clarity. Previous reports on mechanically exfoliated flakes have noted a divergence in these peaks for films progressing from few-layer (< 5) to bulk MoS_2.[25] In

*** Raman spectroscopy was performed with the assistance of Dr. Niall McEvoy.

this work, all of the films resemble bulk MoS_2 except for the 4.17 nm film, which displays a blue-shifted E^1_{2g} peak. The average thickness of 4.17 nm, as measured by SE, suggests an average number of layers of ~6. However, given that the films are polycrystalline, it is probable that the observed peak shift can be explained by the presence of some few-layer (< 5) crystals. For thicker films, Raman data from the area scan were analysed additionally. Raman maps were acquired from the MoS_2 film (~12 nm thick) transferred onto SiO_2 at a power of 250 μW by taking 100 × 100 spectra over a 25 × 25 μm area (10, 000 discrete spectra). Each spectrum had an acquisition time of 0.2 s. As shown in Figure 55, the spectra are consistent over the entire film, indicating the homogeneity of the film synthesis.

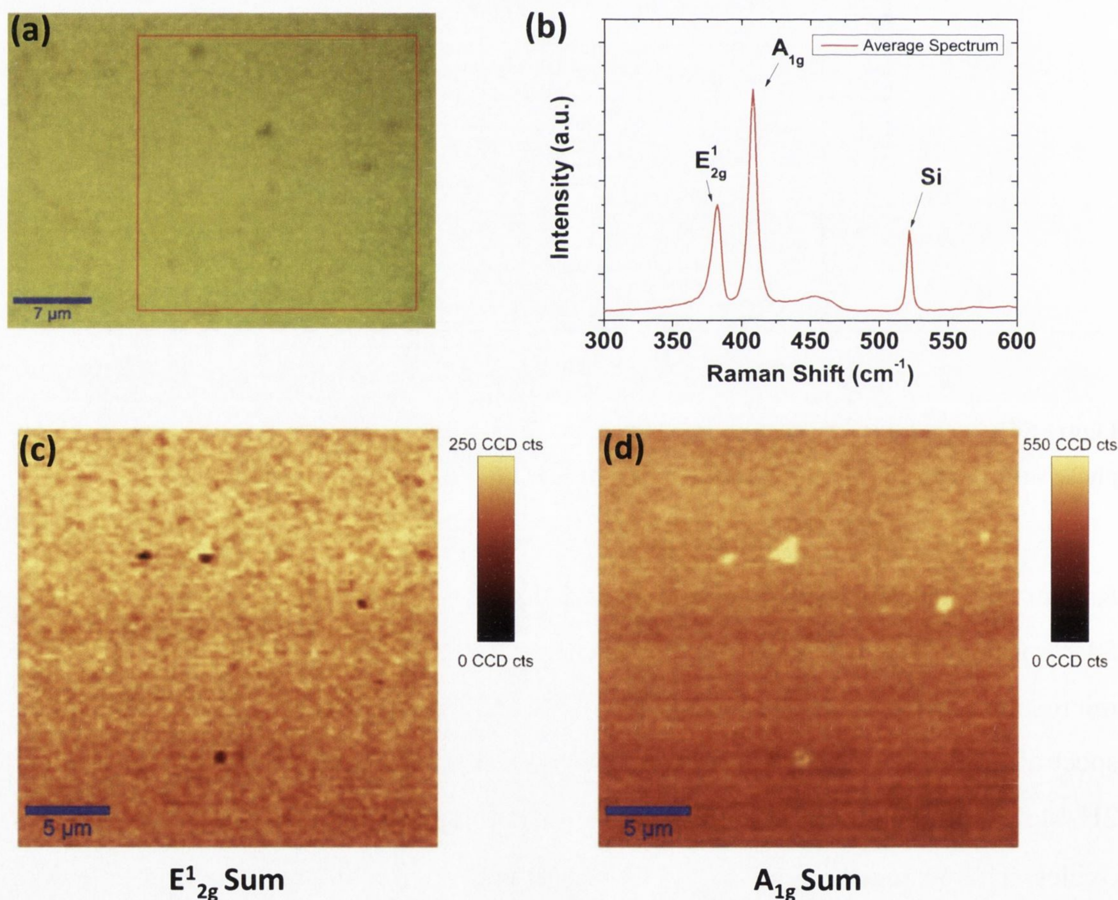

Figure 55 (a) Optical microscopy image of MoS_2 film transferred onto SiO_2. The red box indicates the 25 × 25 μm area over which Raman spectra were acquired. (b) Raman spectrum obtained by averaging over 10,000 discrete spectra which comprised the Raman map. Raman maps showing the intensity of the (c) E^1_{2g} and (d) A_{1g} peaks.

4.3.3 HRTEM Analysis

HRTEM analysis[†††] was performed in an FEI Titan transmission electron microscope at an acceleration voltage of 300 kV. Diffraction patterns were acquired at a camera length of 580 mm to expand the 100 diffraction ring; this increased the pixel count and improved the accuracy of the lattice measurements. MoS_2 films were prepared for TEM characterisation by floating the layers as described previously, then, from water dredging them onto a 300 mesh lacey carbon copper TEM grid (Agar Scientific).

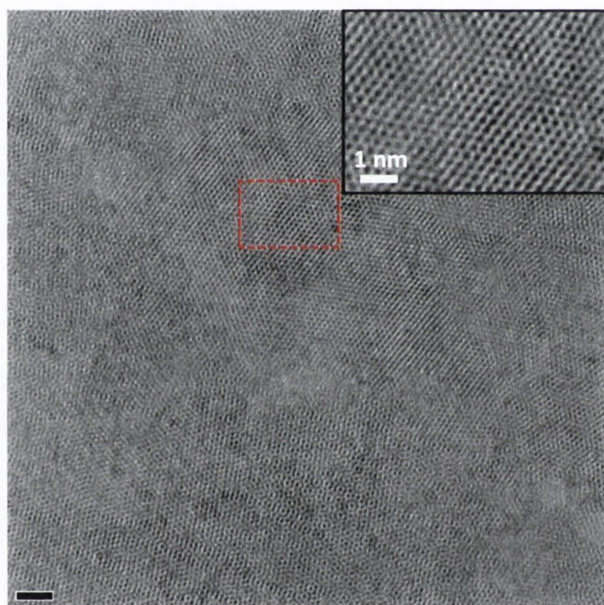

Figure 56 HRTEM image of a MoS_2 thin film transferred to a TEM grid (Inset: a corresponding image at high magnification).

HRTEM analysis of the 8.26 nm film transferred to a TEM grid is depicted in Figure 56, which indicates a polycrystalline structure in plane. Analysis of the selected area electron diffraction (SAED) pattern in various regions gave a Mo-Mo lattice spacing of ~0.32 nm which is in agreement with the literature value (Figure 57(a)).[204-207] However, ~20 % of SAED results showed lattice spacing values between 0.306 – 0.308 nm, which is 4% less than the reported literature value of 0.32 nm (Figure 57(b)). Such an assignment is preliminary, even though the greatest care was taken in ensuring the accuracy of these measurements.

[†††] Maria O'Brien and Clive Downing performed HRTEM imaging.

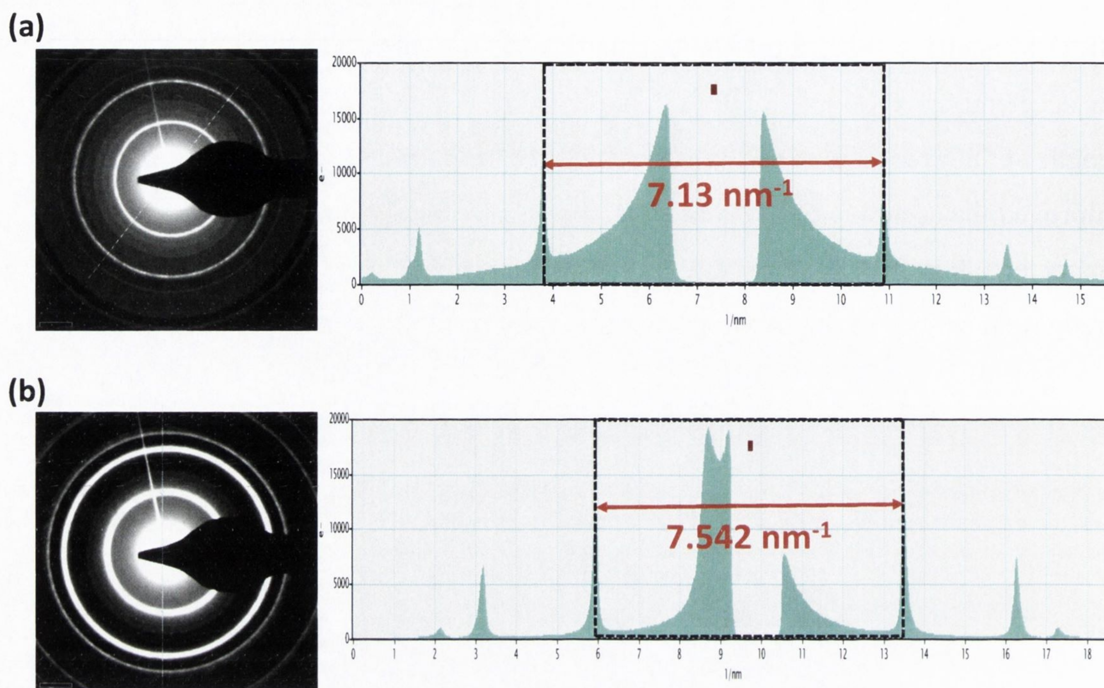

Figure 57 **Representative electron diffraction patterns from different areas of the MoS_2 film revealing Mo-Mo lattice spacing of (a) 0.324 nm and (b) 0.306 nm, respectively.**

4.4 Device Fabrication

Commercially available lightly doped p-Si wafers with a thermally grown SiO_2 layer (292 nm) were used as substrates. The p-Si wafer had a dopant (boron) concentration of 2.5×10^{15} cm^{-3} and <100> orientation. Part of the SiO_2 layer was completely etched by immersing it in 3 % diluted HF for 20 minutes, resulting in a sloped sidewall at the Si/SiO_2 boundary. Using a shadow mask, nickel (Ni) and gold (Au) metal electrodes (Ni/Au = 20/50 nm) were deposited on top of the remaining SiO_2 layer and the exposed p-Si area. In order to achieve ohmic contacts between p-Si and Ni, the substrate was annealed at 400 °C under N_2 flow for 5 minutes. The as-grown MoS_2 thin films were transferred onto the pre-patterned substrates to fabricate devices. A polymer support technique was employed for the transfer process, whereby PMMA (MicroChem) was spin-coated onto the MoS_2. The films were then floated on 2 M NaOH at room temperature until the SiO_2 layer between the MoS_2 and the Si substrates was completely etched away, leaving MoS_2/PMMA films floating on the surface. After cleaning in

deionised water the films were transferred onto the desired substrates. The PMMA support layer was then dissolved by immersion in acetone at room temperature for 20 minutes. Details on the transfer process are presented in Figure 58.

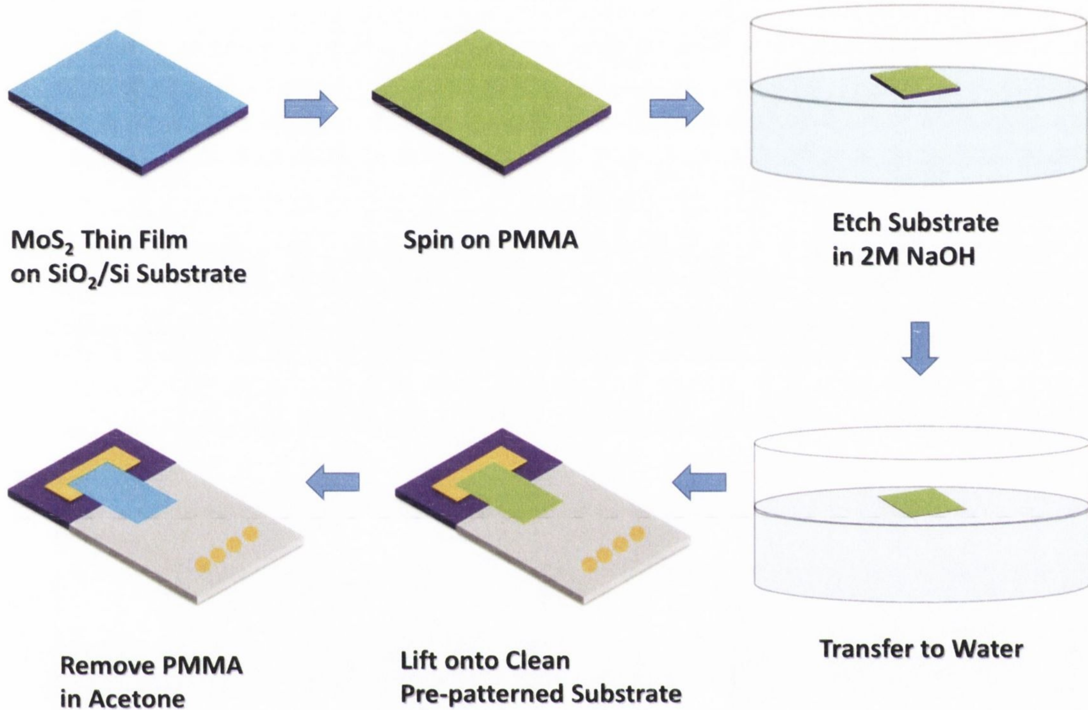

Figure 58 **Transfer process of as-grown MoS_2 thin films onto the pre-patterned substrate.**

4.5 Current-Voltage Measurement

As presented in Figure 58, large-scale MoS_2 films were transferred using a polymer support technique leaving the films mechanically and electrically intact. In order to fabricate photodiodes, MoS_2 films of ~1 cm^2 area were transferred onto the pre-patterned p-Si substrates. The native oxide layer on the exposed silicon surface was removed with HF prior to deposition, ensuring good electrical contact between the MoS_2 and the Si. As shown in Figure 59, one end of the transferred MoS_2 film was placed on the p-Si surface without touching the metal electrode on the p-Si substrate, while the other end was connected to the Au pad on the SiO_2 layer, forming an ohmic contact between them.[109,110,208]

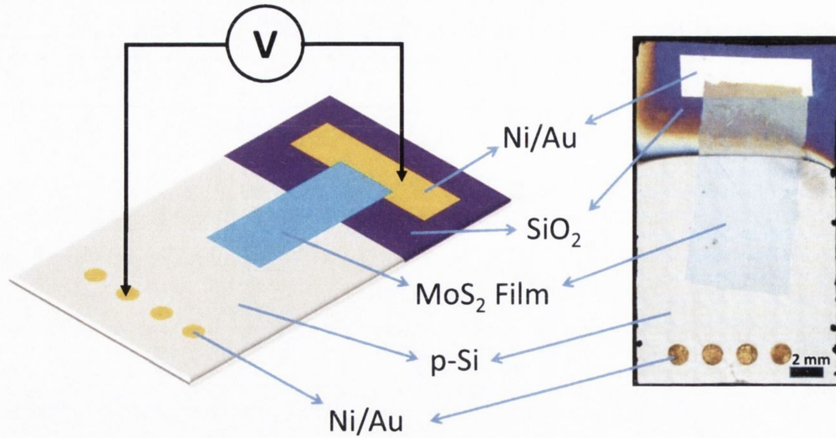

Figure 59 Schematic (left) and photograph (right) of the n-type MoS_2/p-Si heterojunction diode.

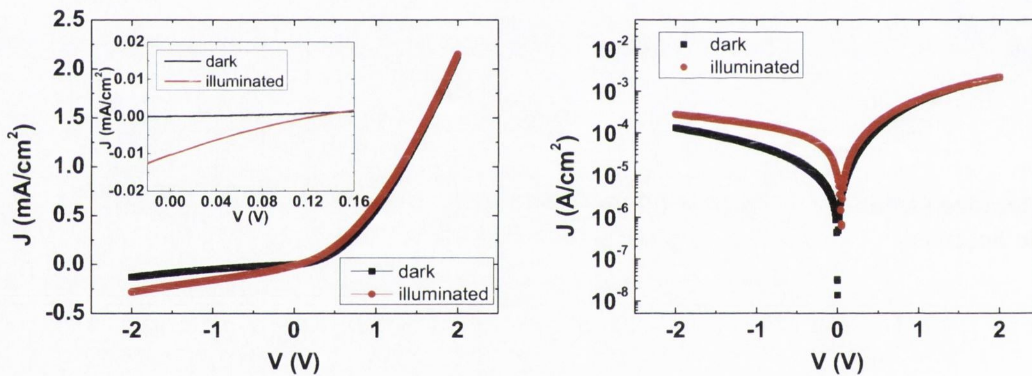

Figure 60 A *J-V* plot of the diode with 12.52 nm thick MoS_2 on a linear scale (left) and semi-logarithmic scale (right) under dark (black) and illuminated (red) conditions. Inset of the left indicates open-circuit voltage (0.13 V) and short-circuit current (0.01 mA/cm^2).

Electrical measurements were conducted on a Suss probe station connected to a Keithley 2612A source meter unit under ambient conditions. The metal electrode on the p-Si substrate was positively biased and the electrode on the SiO_2 layer was negatively biased. A white light source with a solid state dimmer for variable light intensity (ACE Light Source, SCHOTT: A20500, 150 watt halogen lamp) was used for photoconductivity measurements. A plot of current-voltage (*J-V*) measurements of the diode device with 12.52 nm thick MoS_2 is depicted in Figure 60. The MoS_2 layers were fully electrically intact and well contacted by the gold pad as detailed above and

therefore current transport was dominated by the MoS_2/Si interface region. Clear rectifying behaviour was observed in the dark.

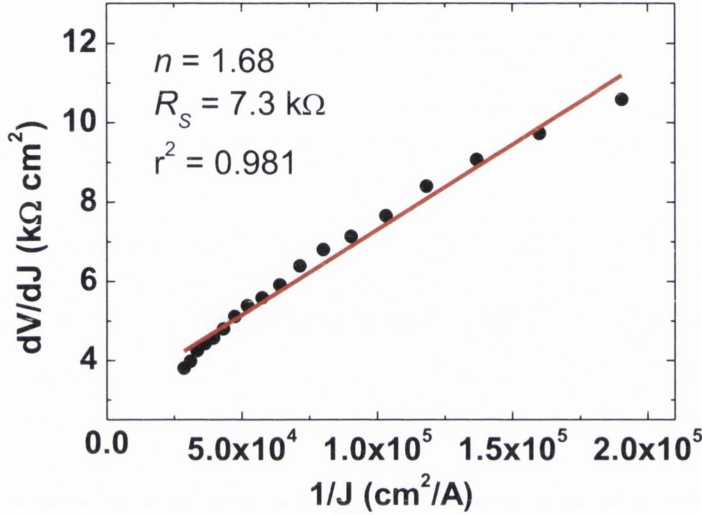

Figure 61 Plot of *dV/dJ* vs. *1/J* extracted from the *J-V* data of the diode with 12.52 nm thick MoS_2, giving a series resistance value of 7.3 kΩ and an ideality factor value of 1.68.

The forward *J-V* characteristics of a diode in dark conditions can be explained by thermionic emission theory and analysed using Eq. (3.5). The equation can be modified in terms of *V* and *J* and rewritten as the following equation.

$$V = JAR_S + \frac{nk_BT}{q}\ln\left(\frac{J}{J_S}\right), \tag{4.1}$$

Differentiating Eq. (4.1) in terms of *J*, we obtain

$$\frac{dV}{dJ} = AR_S + \frac{nk_BT}{qJ}. \tag{4.2}$$

According to Eq (4.2), *dV/dJ* is linearly proportional to *1/J*. Thus, the ideality factor ($n \geq 1$) of a diode and the series resistance can be extracted by extrapolating the linear region of the plot of *dV/dJ* vs. *1/J*. The *dV/dJ* vs. *1/J* plot of the 12.52 nm device is shown in Figure 61, giving a series resistance value of 7.3 ± 0.3 kΩ from the y-axis intercept and an ideality factor value of 1.68 ± 0.05 from the slope.

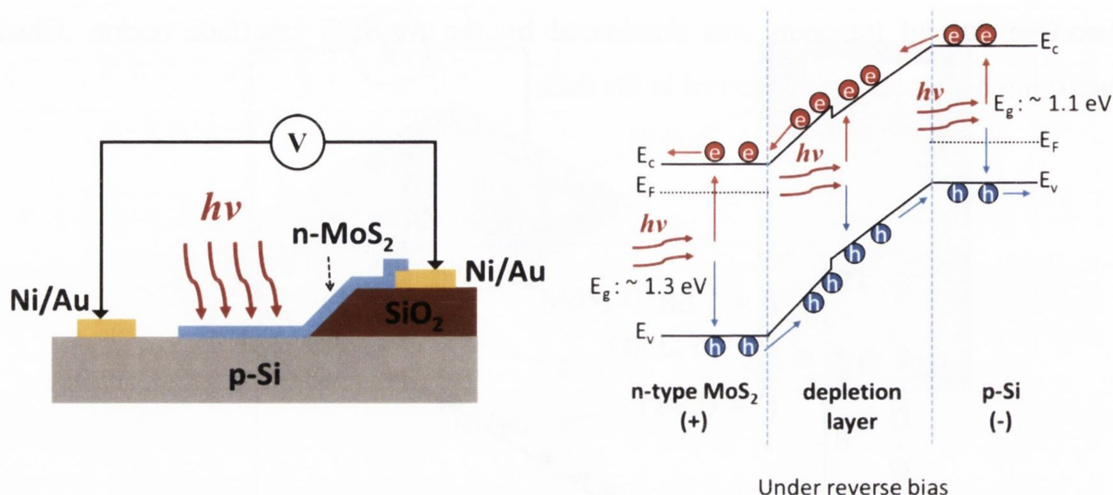

Figure 62 **Cross sectional view of the n-type MoS2/p-Si diode structure (left) and its energy band diagram in reverse bias (right) under illumination, describing the movement of electrons (ⓔ) and holes (ⓗ). E_c, E_F, E_v, E_g and $h\nu$ denote the conduction band, Fermi energy level, valence band, band gap and photon energy of the incident light, respectively.**

4.6 Photoconductivity

The diodes exhibit obvious photoconductivity under illumination with a white light source as presented in Figure 60. While little variation in the current density is seen between dark and illuminated conditions under forward bias, there is an obvious distinction in the reverse bias region. In the dark the device is in the off state under reverse bias and there is low reverse leakage current, but while illuminated, an evident current increase is observed in the reverse bias region. A cross sectional view of the n-type MoS_2/p-Si diode structure and its energy band diagram in reverse bias under illumination are shown in Figure 62. The n-type MoS_2 and the p-Si substrate form a p-n heterojunction and the topside of the MoS_2 film is exposed to the light source. Upon the incidence of photons, the valence band electrons are excited to the conduction band, generating electron-hole pairs in the n-type MoS_2, depletion layer and p-type Si. In the depletion layer, the excited electrons and holes are accelerated to the n-type MoS_2 and to the p-Si, respectively, and they are then collected in the n-type MoS_2 and p-Si region. When the electrodes of the p-Si substrate and n-type MoS_2 thin film are connected to an external circuit, electrons will flow away from the n-type MoS_2 film to the p-Si side

and holes will flow away from the p-Si substrates to the n-type MoS_2 side, generating a current.

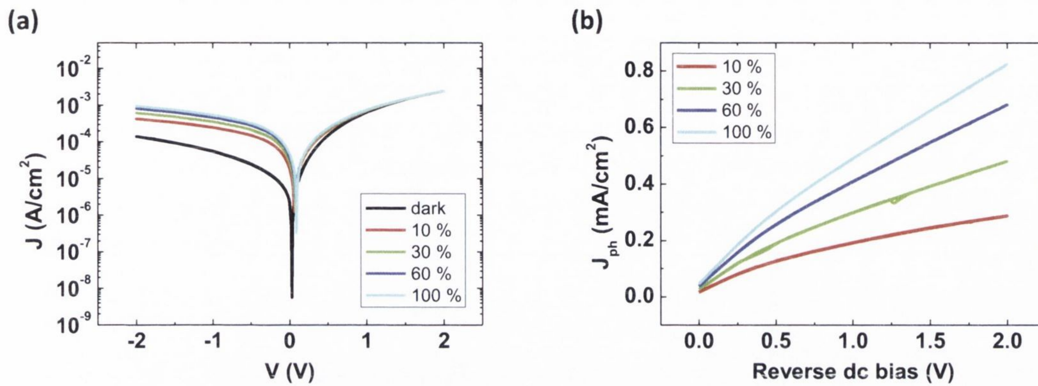

Figure 63 (a) *J-V* plot of the diode with the 12.52 nm thick MoS_2 film under various incident light intensities (dark, 10, 30, 60 and 100 % of full intensity) and (b) an associated photocurrent density (J_{ph}) plot extracted from the *J-V* measurements in the reverse bias region.

Figure 63(a) and (b) show a *J-V* plot of the diode with the 12.52 nm thick MoS_2 film under various light intensities and a photocurrent density (J_{ph}) plot extracted from the *J-V* measurements in the reverse bias region. The incident light intensity was controlled by a solid state dimmer and expressed using a relative value for the full intensity of the white light source. When the light intensity increased from 0 to 100 %, the measured current density also showed an increasing trend in the reverse bias region proportional to the incident light intensity. From the photo response of the diode, which measures the output photocurrent for varying input light intensity, the relative responsivity of the diodes to the light can be compared. At reverse dc biases of V = -1 V and -2 V, the generated J_{ph} shows a nearly linear increment giving a photocurrent value of 0.49 mA and 0.83 mA at the full intensity of the light source, respectively (Figure 64). The larger responsivity at higher reverse dc biases can be attributed to the fact that the energy barrier height at the junction between n-type MoS_2 and p-Si increases due to the increasing external electric field when a higher reverse bias is applied to the junction. This means the electrical potential difference across the depletion layer at the junction becomes much larger, which results in a stronger acceleration of electrons and holes in the depletion region and therefore a higher current.

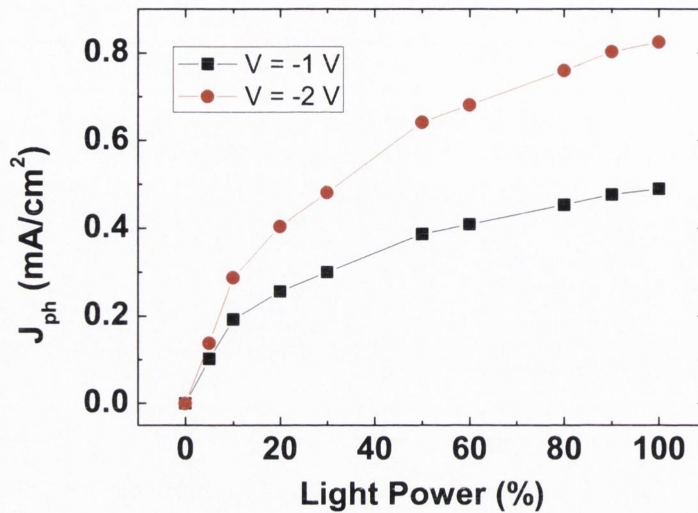

Figure 64 **A J_{ph} plot with varying incident light intensity at reverse biases of V = -1 and -2 V.**

In addition, the effect of modifying the MoS_2 thickness on the photocurrent was investigated. The thickness values of MoS_2 films, as measured by SE, were found to be 4.17, 8.26 and 15.96 nm. The *J-V* plots exhibit clear photoconductivity for all the devices when they are illuminated by the light source, as shown in Figure 65(a) – (c). The J_{ph} values of the diodes with different MoS_2 thicknesses under reverse bias are compared in Figure 65(d). It is clear from these results that when the same incident light intensity (5 % of full intensity) is applied, the diode device with a thicker MoS_2 thin film shows higher photocurrent values. This is because the volume of photon absorption in the n-type MoS_2 thin film becomes larger with increased MoS_2 film thickness. As more photons are absorbed in the thicker MoS_2 layer more electron-hole pairs are produced, increasing the photocurrent of the device. This implies that it is possible to define the level of photoconductivity for MoS_2/Si photodiode devices through modulation of the MoS_2 film thickness.

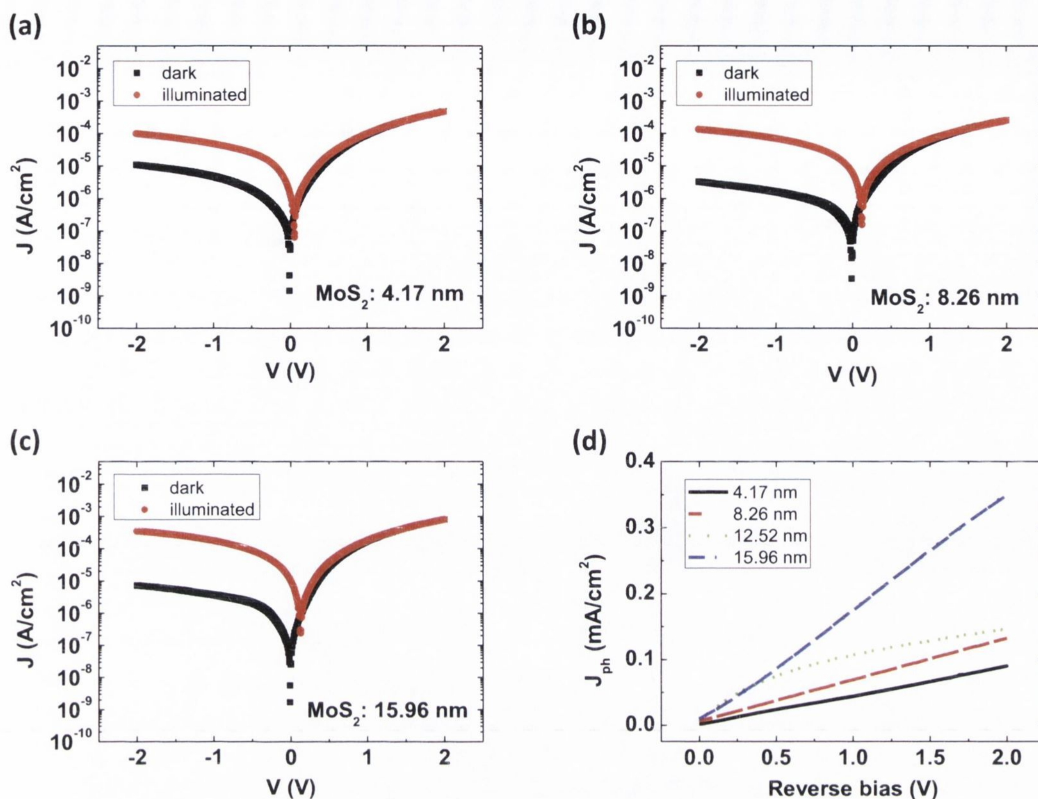

Figure 65 Semi-logarithmic *J-V* plots of the MoS_2/p-Si diode devices with MoS_2 film thickness of (a) 4.17 nm, (b) 8.26 nm, and (c) 15.96 nm in the dark and illumination (5 % of full intensity). (d) A plot of J_{ph} of the diode devices with different MoS_2 thickness (4.17, 8.26, 12.52 and 15.96 nm) under reverse dc bias.

4.7 Spectral Response

The absolute spectral response[‡‡‡] was measured using a lock-in technique with a chopped photon flux over an investigated wavelength interval of 10 nm. It was measured by a comparative method to a known spectral response of a reference detector using a Labview controlled setup. The light was generated by a tungsten-halogen and a deuterium-arc lamp, and covered the wavelength range of 200 – 2000 nm. Specific wavelengths were selected by a monochromator (Acton Research Corporation, SP-555) using appropriate grids and filters. The light power density varied from 1 μW/cm^2 at a wavelength of 200 nm up to 55 μW/cm^2 at a wavelength of 1150 nm. A silicon photodiode was used to calibrate the setup. Due to the spectral limitation of the silicon

[‡‡‡] Spectral response was measured by Sarah Riazimehr in University of Siegen, Germany.

photodiode, the spectral response measurement was limited to the range of 400 nm – 1250 nm. The detector currents were measured by pre-amplifiers (Femto, DLPCA-200) and lock-in amplifiers (Princeton Applied Research Corporation, Model 5210) with 300 ms integration time and 0.4 Hz band width at 17 Hz optical chopper frequency for detection of ultra-low currents down to 10 pA. The measurement principle allows a wavelength dependent correction factor to be established for the probe spectral response calculation which takes into account variations of the preamplifiers, the difference between the reference detector area and the probe area as well as varying photo flux densities caused by the monochromator grids and filters.

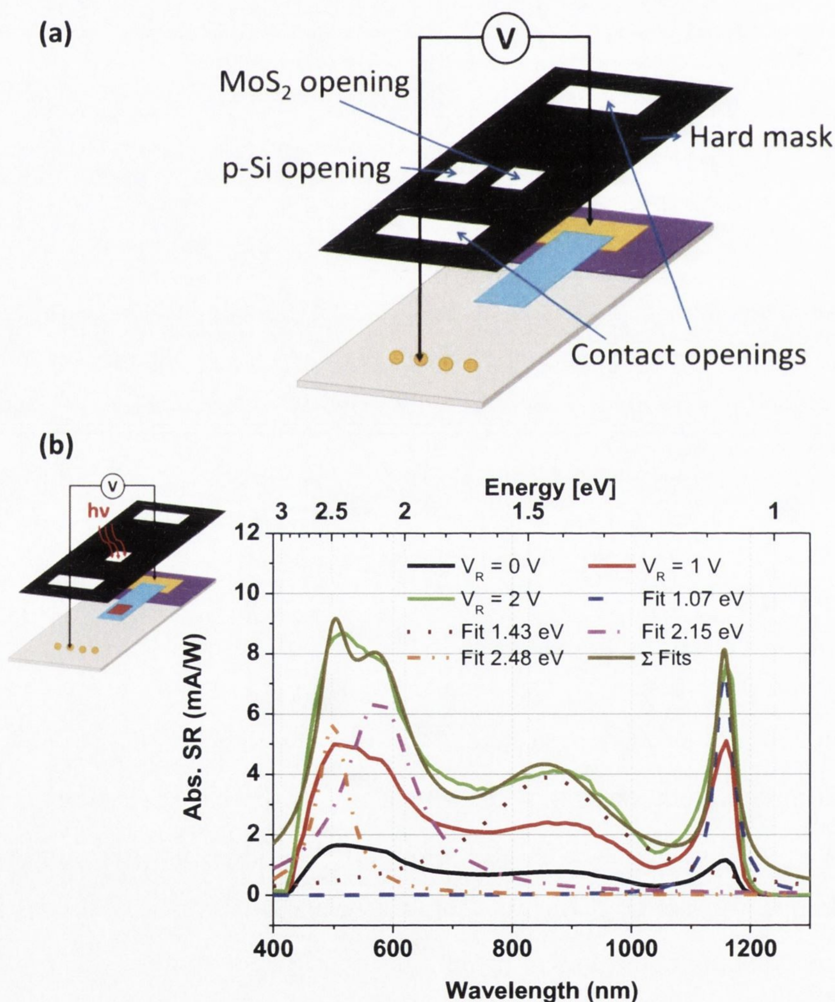

Figure 66 (a) Schematic of the heterojunction diode with mask openings for MoS_2 and p-Si indicated for spectral response measurements. (b) Plot of absolute spectral response (Abs. SR) vs. wavelength (lower x-axis) and energy (upper x-axis) related to the diode device with an 8.26 nm thick MoS_2 film at zero bias and reverse bias (V_R) of 1 and 2 V with the mask openings on MoS_2 and (c) p-Si. The inset indicates the area of the diode illuminated.

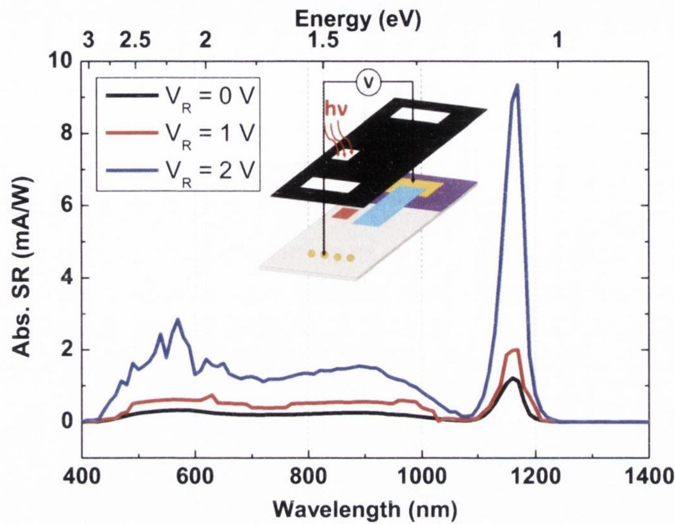

Figure 67 Plot of absolute spectral response (Abs. SR) vs. wavelength (lower x-axis) and energy (upper x-axis) related to the diode device with an 8.26 nm thick MoS2 film at zero bias and reverse bias (VR) of 1 and 2 V with the mask openings on p-Si.

Since the collimated incident light beam is bigger than the probe active area, a mask was used to define an illumination spot of 20 mm^2 on the device, either on the MoS_2 region or on the p-Si next to the MoS_2 (Figure 66(a)). This allows contributions from the blank p-Si substrate to the generated photocurrent to be eliminated. The spectral response of the diode device with an 8.26 nm thick MoS_2 film for a reverse bias voltage between 0 – 2 V is plotted in Figure 66(b). The multilayer MoS_2 photodiode exhibits a wide spectral response, which increases with higher reverse bias voltages due to the increase of the external electrical field. The spectral responsivity of 1.4 – 8.6 mA/W at a reverse dc bias of V = -2 V is achieved in the broad spectral range from visible to near-infrared. While this performance is inferior to that of recently reported monolayer (800 A/W) and multilayer MoS_2 (thickness 30 – 60 nm, 120 – 210 mA/W) photodetectors,[114,209,210] it is better than previously reported monolayer MoS_2 phototransistors (~7.5 mA/W)[118] and graphene photodetectors (~0.5 mA/W).[211]

The underlying p-type silicon absorption peak is observed at approximately 1.07 eV (1158 nm) confirmed in a reference measurement where the illumination spot was moved to the p-Si (Figure 67). Three additional peaks were identified through fitting in the spectrum at 1.43 eV, 2.15 eV and 2.48 eV. The first peak at 1.43 eV (867 nm) can be explained by the indirect band transition (Σ_m-Γ_v) of multilayer MoS_2 as indicated by

the blue arrow in Figure 68(a). Moreover, there is a strong contribution from the direct band gap transition observed in nanoscale MoS_2 films. This is an interesting observation considering the thickness of the film is 8.26 nm and therefore approximately 12 layers thick. The direct band gap contribution is split into light- (K_m-K_{v1}) and heavy holes (K_m-K_{v2}). Therefore, two distinct peaks in the spectral response are observed at energies of 2.15 eV (576 nm) and 2.48 eV (500 nm), illustrated by the red and green arrow in Figure 68(a). Interestingly, a blue-shift of 0.13 eV for the indirect transition and of approximately 0.4 eV for both direct transitions was observed compared to the theoretical values for exfoliated MoS_2 (i.e. 1.3 eV for the indirect band transition and 1.8 eV and 2.0 eV for light- and heavy holes for the direct band transition)[106,209] and those observed experimentally.[122,203] This blue shift in the spectral response of bulk MoS_2 compared with the absorption spectrum was previously mentioned by Wilson and Yoffe.[212]

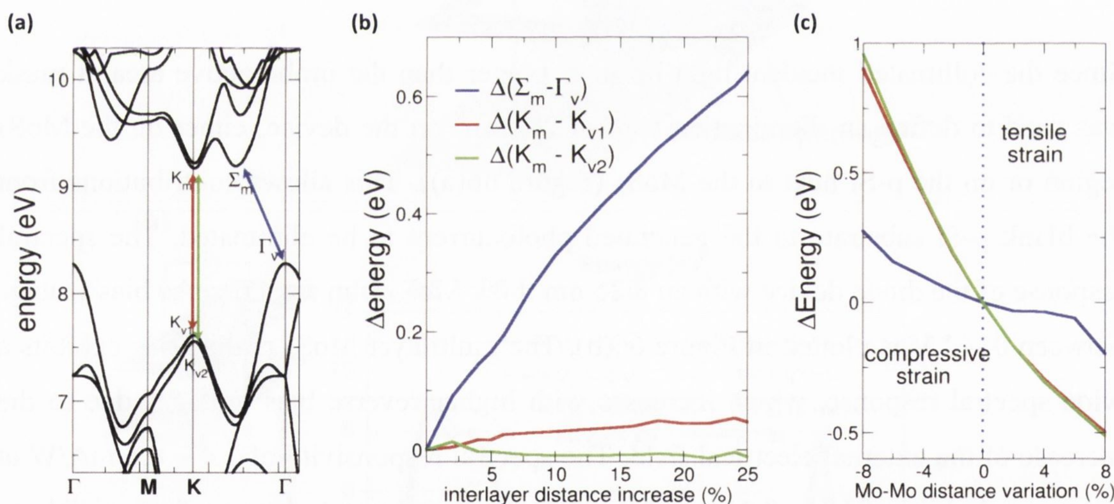

Figure 68 (a) Calculated energy bands for bulk MoS_2. (b) Variation of the direct and indirect band gaps, with respect to the equilibrium case, as a function of the interlayer distance (expressed in %) and (c) variation of the direct and indirect band gaps, with respect to the equilibrium case, as a function of the lattice spacing (expressed in %).

Density functional theory (DFT) calculations§§§ were employed to investigate potential causes of the observed blue shift. In particular, the influence of both inter-layer spacing and lattice spacing on the band structure of multilayer MoS_2 was studied. DFT

§§§ DFT calculation was performed by Prof. Gianluca Fiori in University of Pisa, Italy.

calculations were performed to compute the electronic band structure of bulk MoS_2. Computed bands are shown in Figure 68(a), where the maxima (K_m, Σ_m) and the minima (K_{v1}, K_{v2}, Γ_v) of the conduction and valence bands, respectively, are highlighted. In Figure 68(b), the variations of the direct (K_m-K_{v1}/K_{v2}) and indirect band gap (Σ_m-Γ_v) with respect to the equilibrium case, as a function of the inter-layer distance (expressed in %) are shown. As soon as the interlayer distance is increased, the indirect band gap increases, while the direct band gap is negligibly affected. This is in agreement with recent simulations performed on bilayer MoS_2.[119] Γ_v are characterised by *p*-orbital wave-functions centred in correspondence of S atoms, while K minima are related to *d*-orbitals localised around Mo atoms. As a consequence, K points are less affected by increases in the interlayer distance, while the opposite holds for Γ_v minimum. In Figure 68(c), the same quantities as above are shown, but as a function of lattice spacing variation. In this case, the larger shift of the direct band gaps with respect to the indirect band gap is qualitatively reproduced as soon as the lattice is compressed. From a quantitative point of view, a compression of 4% serves to explain the observed blue-shifted peak positions for both the indirect and direct transitions in the spectral response analysis of the device. Thus the observed blue-shifted absorption peaks is tentatively assigned to the disordered lattice of the MoS_2 films. This assumption is supported by the HRTEM analysis which shows slight compression in regions of the polycrystalline films. This could stem from the high temperature growth mechanism or could possibly be caused by the film transfer process. It must be noted here that a difference in the strain transfer and relaxation mechanism may exist when the MoS_2 films are transferred onto different substrates, such as a TEM grid and a silicon substrate. Further, the presence of dopants and contamination (e.g. oxygen) in the films cannot be completely ruled out, which could lead to lattice distortions. Nonetheless, the variation of the photo-response of 2D TMDs is an exciting and unexpected finding and will undoubtedly be the subject of further investigation, particularly as this variation in the spectral response of layered TMDs could present a wide range of opportunities in material design.

4.8 Conclusion

P-n heterojunction diodes were fabricated using n-type MoS_2 films with varying thicknesses and p-Si substrates. MoS_2 thin films are laterally in contact with p-Si substrates over the substrate area, allowing for direct exposure to incident light of varying intensity. Electrical measurements revealed that the n-type MoS_2/p-Si diodes have good rectifying behaviour as well as clear photoconductive characteristics. The photocurrent of the device has a strong dependence on the MoS_2 film thickness whereby the thicker MoS_2 films produce more photocurrent due to their increased volume for photon absorption. This demonstrates that it is possible to control the photocurrent of MoS_2/Si diodes by modulating the thickness of the MoS_2 layer. The spectral response of the device showed that there are contributions from direct and indirect band transitions in the multilayer MoS_2 film. Further, a substantially extended spectral range for the device into the visible range was observed.

By employing a polymer support transfer process for the MoS_2 thin films the MoS_2/Si hybrid structure, which combines a semiconducting nanoscale TMD and a traditional semiconducting material, was realised. This approach could potentially be extended to various other semiconducting materials in such hybrid structures. Further comprehensive studies of such structures are required to improve device performance and engineer the properties of the interface. Nevertheless, this type of hybrid device demonstrates the benefits of using long developed semiconducting technology to take advantage of the novel properties of nanomaterials for future nano- and optoelectronic devices.

5. Summary and Future Work

5.1 Summary

Two kinds of vertically stacked hybrid devices have been fabricated on silicon substrates using various conductive carbon thin films and a semiconducting TMD thin film, and their material characteristics as well as electrical properties have been investigated in this thesis.

In the first part of this work, the electrical characteristics of Schottky contacts between three types of conductive carbon thin films (i.e. pyrolytic carbon, glassy carbon from pyrolysed photoresist and graphene) and n-type silicon were intensively studied in diode devices. While the pyrolytic carbon films were synthesised by CVD from hydrocarbon precursors, the glassy carbon thin films were made by pyrolysing photoresist, which was deposited on substrates by spin-coating, at high temperature. The graphene was produced on copper foils using a CVD method. Typical dc current-voltage measurements were conducted for the devices and all the devices displayed very clear rectifying behaviour. Several important diode parameters including the ideality factor, n, the barrier height, φ_B and the series resistance, R_S, were extracted from the analysis of the dc current-voltage measurement data. Furthermore, ac impedance spectra were recorded at various dc biases. An equivalent circuit model which includes the effect of the metal electrode contacts of the device was developed for analysis of the impedance spectra. By simulating the equivalent circuit model with experimental data, additional information on the Schottky contacts could be obtained, such as the built-in potential and more reliable barrier height values. Therefore, it can be emphasised that utilising impedance spectroscopy makes it possible to localise the undesirable secondary effects such as contact capacitance and resistance of metal electrodes from the total electrical signal, allowing more reliable analysis of Schottky contacts.

In the second part, vertically stacked p-n heterojunction diodes have been made using n-type MoS_2 and p-type silicon. The n-type MoS_2 thin films were synthesised on a large scale using a vapour phase sulfurisation process, whereby pre-deposited Mo films on insulators are sulfurised in a quartz tube furnace. Continuous MoS_2 thin films with various thicknesses were obtained by changing the pre-deposited Mo metal thickness. The p-n heterojunction diodes were then fabricated by transferring the as-grown MoS_2

thin films onto the pre-patterned p-type silicon substrates. From the electrical measurements, the devices were shown to have good rectifying performance. In addition, the p-n heterojunction diodes exhibited good photoconductivity which could be controlled by changing the thickness of the MoS_2 layer. Spectral response tests indicated that the diodes have a broad spectral response, and it was found that this is caused by direct and indirect band transitions of the nanoscale MoS_2 thin films.

5.2 Future Work

Conductive carbon thin films have been characterised in various ways and the electrical properties of the Schottky contacts between carbon and silicon have been thoroughly studied. Although high performance devices have been achieved, further work is still needed to fulfil general requirements for industrial applications. In particular, our PPF/n-Si and PyC/n-Si SBDs have a very simple integration scheme and both carbon depositions are very cost effective processes. A more advanced integration scheme, including guard rings to avoid edge leakage, complete removal of any possible Si oxidation at the interface and a reduction of the series resistance could give even better performance. Schottky diodes are frequently used as high-speed switching devices due to their simple structure and relatively fast on/off speed compared to other p-n diodes or FETs. The carbon-silicon SBDs hold great promise, particularly for power switching device applications. Since carbon electrodes are very stable at very high temperatures, unlike metals which can migrate into silicon, one can expect that carbon-silicon Schottky diodes would be ideal for high temperature and high current density switching devices. However, sufficient practical endurance tests under such conditions have not yet been carried out. In addition, it is necessary to continue more work to define the dependence of the SBH on the doping level of the silicon substrates used as it is expected that the value of Schottky barrier height of carbon-silicon contact could be changed depending on the impurity concentration of silicon substrates. In reverse, with known silicon doping, the SBDs could be also used to determine the doping of the carbon electrode since doped carbon films are predicted to have a wide range of applications in electronic devices and energy applications.

Due to its large surface area, graphene has been widely used for sensor device applications.[187,213-215] However, most graphene sensors thus far have been based on

FET devices which require complex fabrication processes and typically suffer from poor reproducibility. Recently, graphene sensors using a graphene-silicon SBD have been introduced, showing robust sensing performance for various chemicals with good repeatability and long-term stability (see Figure 69).[193] Furthermore, surface doping could lead to changes in the diode performance which could be used for bio sensing applications such as bacteria sensors. Sufficient studies of the reactivity of such devices under various conditions have yet to be undertaken and further investigation into the selectivity is still necessary. Nevertheless, the ease of fabrication, large surface area and long-term stability make graphene-silicon SBDs promising future sensor devices.

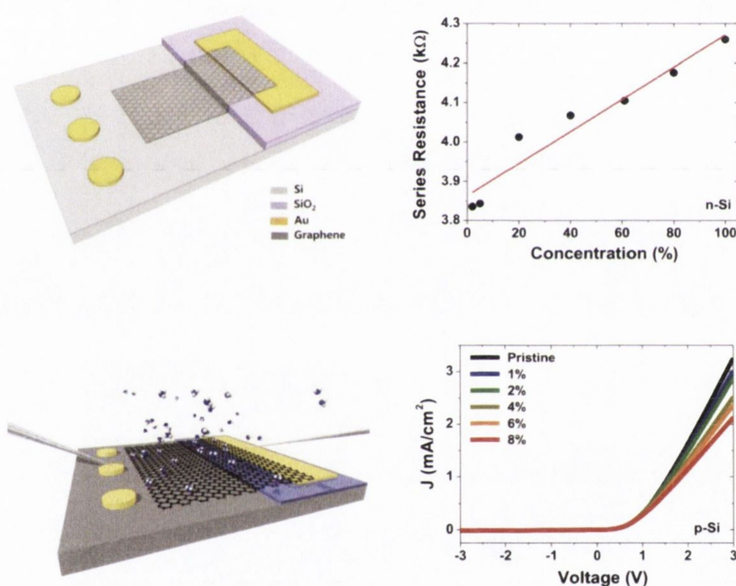

Figure 69 Schematic diagram of a graphene-silicon SBD sensor. Example of the chemical sensor device (top) showing variation of the series resistance of the SBD as a function of the concentration of anisole in benzene, and example of gas sensor (bottom) showing change of current-voltage characteristics of the SBD depending on the concentration of ammonia in argon.[193]

Vapour phase sulfurised multilayer MoS_2 thin films were used to fabricate MoS_2-silicon p-n heterojunction diodes in this work. Although it has been confirmed that these show good photoconductivity, the analysis of their time response measurements have not been carried out yet. The time response measurements would be quite interesting and it would give more comprehensive information of the potential for future applications, particularly as light sensors or switching devices. In addition, a diode based on a monolayer MoS_2 film has not yet been tested. Since the direct band

gap transition is dominant in single layer MoS_2, it is expected that p-n heterojunction diodes consisting of single layer MoS_2 on silicon substrates could be used for practical light emitting diode applications. Also, it should be noted that the multilayer MoS_2 films used in the study are polycrystalline in nature, and devices fabricated from such films typically show inferior performance compared to their pristine counterparts prepared by mechanical exfoliation. This can possibly be attributed to degradation of performance caused by the adverse effects of the grain boundaries. Although a few studies on device applications with vapour phase grown single-crystalline MoS_2 have appeared recently (see Figure 70),[115,216-218] the difficulty in growing a continuous film with a large grain size and the development of a reliable transfer technique must be resolved for the realisation of practical device applications.

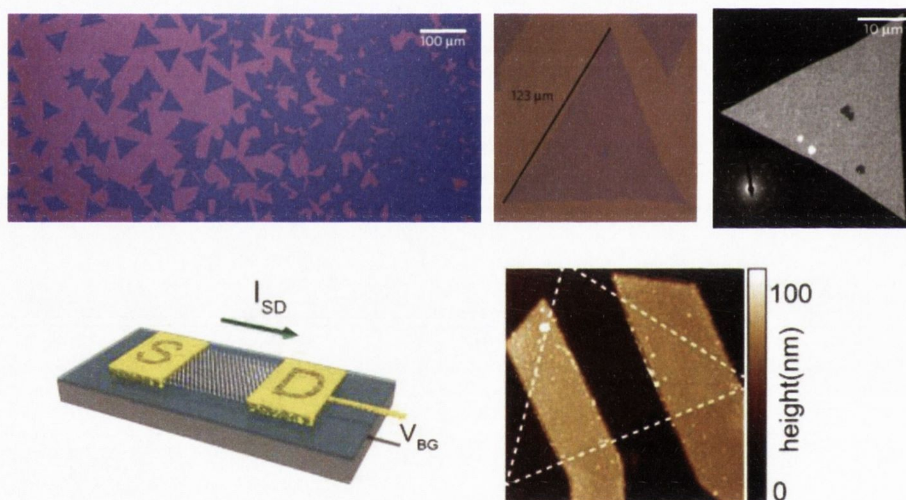

Figure 70 Optical image of triangular vapour phase sulfurised MoS_2 on a SiO_2/Si substrate and its dark-filed TEM image with the diffraction pattern inset showing that the triangle is a continuous single crystal (top row).[216] Schematic diagram of a single-crystalline monolayer MoS_2 FET device and atomic force microscopy image (10 µm) of a two-terminal FET device where the shape of the triangular crystal is highlighted (bottom row).[218]

Recently, strain engineering of 2D layered TMDs has been regarded as a powerful strategy to investigate the modification of the band structure and its electronic and optoelectronic properties. For example, Conley *et al.*[219] experimentally showed that the uniaxial tensile mechanical strain on mechanically exfoliated mono- and bilayer MoS_2 results in band gap modulation and a transition from an optically direct to an indirect material in strained MoS_2 samples. Liu *et al.*[220] also carried out strain-induced band gap

engineering for CVD grown monolayer MoS_2 on flexible polymer substrates, quantifying the effective transferred strain from the substrates to MoS_2. In this study, a certain influence of strain on MoS_2 films has been monitored from the spectral response measurements of MoS_2/Si photodiodes. From the spectral response analysis of our MoS_2/Si photodiodes, it has been revealed that there was slight blue shift of direct and indirect transition peaks of the MoS_2 film. HRTEM analysis and DFT calculation proved that the blue shift can be caused by the effect of in-plane compressive strain of MoS_2. This is remarkable because our results suggest that spectral response studies for 2D layered materials can be effectively utilised as a strain-mapping tool. It can be particularly advantageous to explore novel physics of 2D materials and tune their optical/electronic properties for device applications such as photodetectors and photovoltaic devices since one can easily monitor strain-induced spectral response variation over the broad range of wavelength. However, thorough study on the origin of such strain has not been conducted yet, although we tentatively suggested the high temperature growth mechanism or the film transfer process as possible causes for the strain. Further studies including comparison of the spectral response data between as-grown MoS_2 and transferred MoS_2, and monitoring strain-induced band gap modulation from photodiodes composed of other 2D TMDs such as $MoSe_2$, WS_2 and WSe_2 should be followed for this.

Appendix

A.1 Analysis of MoS_2 Thin Films using Spectroscopic Ellipsometry****

A.1.1 Background

For optoelectronic device applications of MoS_2 to be fully understood, it is necessary to know information about its optical constants such as the refractive index (*n*) and extinction coefficient (*k*). Spectroscopic ellipsometry (SE) is a powerful non-destructive technique to measure the optical properties of thin films. In SE the wavelength dependent optical constants and the thickness of thin films can be determined by analysing the change in the polarisation state of the reflected light from the film surface and developing an optical dispersion model for the film material.[145] It is frequently used in industry for film characterisation and in *in-situ* thickness monitoring because it is fast, cheap and non-destructive. In recent years, SE has been employed to investigate the optical constants of graphene,[221-224] however, to date SE characterisation on 2D layered TMDs, such as MoS_2, has rarely been reported.

Here, the optical properties of MoS_2 thin films with different thicknesses are characterised using SE. The MoS_2 thin films were synthesised on substrates using a vapour phase sulfurisation process and characterised by UV-visible absorption spectroscopy and Raman spectroscopy. Based on SE measurements an optical dispersion model was developed for the MoS_2 thin films and the optical constants (*n*, *k*) and the film thickness values were extracted. In addition, optical band gap values of the MoS_2 thin films were obtained from analysis of the extracted *k* values. The values are consistent with data derived from other techniques and theoretical values. This work establishes SE as a viable tool for the characterisation of TMDs. Further, the results obtained indicate that vapour phase derived MoS_2 exhibits similar optical properties to exfoliated materials, making it a strong candidate for the manufacture for optoelectronic devices.

**** Parts of this chapter appeared in P-4.

A.1.2 MoS_2 Synthesis

Vapour phase sulfurisation was employed to synthesise MoS_2 thin films as described in Chapter 4.[††††125,201] Mo (99.99 %, MaTecK) films with various thicknesses (1 – 20 nm) were deposited on fused quartz substrates (~10 mm × 10 mm) and on SiO_2/Si (SiO_2, ~290 nm thick) substrates (~10 mm × 10 mm), using a Gatan Precision Etching and Coating System (PECS). A quartz crystal microbalance was used to monitor the Mo film deposition rate (< 0.1 nm/s) and thickness. The Mo samples were sulfurised in a quartz tube furnace as shown in Figure 53. The vapour phase sulfurisation process is explained in detail in the experimental section of Chapter 4.

A.1.3 Film Characterisation

In the synthesis method employed, vapourised sulfur reacts with pre-deposited Mo layers, yielding continuous MoS_2 thin films. An optical image of MoS_2 thin films on SiO_2/Si substrates (sample A, B, C, D and E) is shown in Figure A - 1. The samples are clearly distinguishable from each other due to the difference in surface colour caused by their varying thicknesses. The films appear homogeneous over the sample area of ~10 mm × 10 mm.

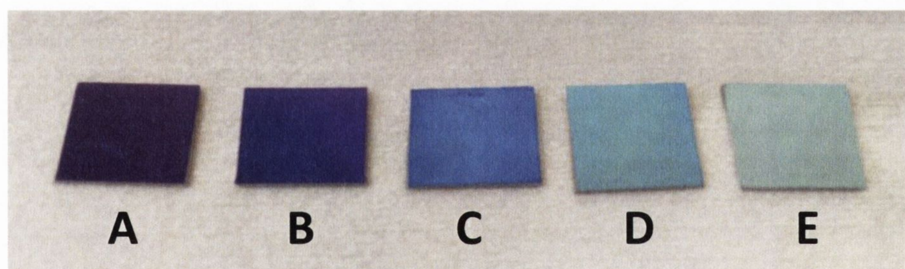

Figure A - 1 Photograph of MoS_2 samples synthesised by vapour phase sulfurisation with increasing thickness (A – E).

†††† MoS_2 films were prepared by Maria O'Brien.

Raman Spectroscopy: ‡‡‡‡ Raman spectra of five films, with different thicknesses, are shown in Figure A - 2. It is evident that the E^1_{2g} and A_{1g} peaks shift closer to one another with decreasing film thickness. This is consistent with the report of Li *et al.*,[143] who described the layer thickness dependence of the Raman signal of mechanically exfoliated MoS_2 with decreasing layer thicknesses. In the case of sample E the E^1_{2g} and A_{1g} peaks are seen at 384.2 cm^{-1} and 409.6 cm^{-1}, a separation of 25.4 cm^{-1}, whereas for sample A the same peaks manifest at 387.0 cm^{-1} and 407.1 cm^{-1}, a separation of 20.1 cm^{-1}. This suggests that sample A consists of very few (1 – 3) layers, whereas sample E behaves like bulk MoS_2.

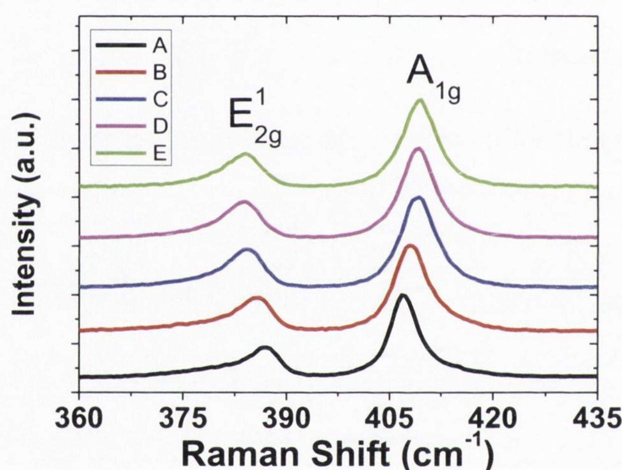

Figure A - 2 **Raman spectra of the MoS_2 thin films on the SiO_2/Si substrates (sample A, B, C, D and E).**

A.1.4 Optical Properties Analysis

The optical properties of the MoS_2 thin films were investigated by SE. The raw SE data comprise a tabulation versus wavelength of the amplitude ratio (Ψ, psi) and the phase difference (Δ, delta) between the p- and s-polarised components of the reflected light. The two parameters measured by a SE system are related to the ratio ρ, defined by the equation of $\rho = r_p/r_s = \tan(\Psi)\exp(i\Delta)$, where r_p and r_s are the amplitude reflection coefficients for the p-polarised and s-polarised light, respectively.[145] As shown in

‡‡‡‡ Raman spectroscopy was performed with the assistance of Dr. Niall McEvoy.

Figure A - 3, a four-layer optical model which consists of a Si substrate, an interface layer between Si and SiO_2, a SiO_2 layer and a MoS_2 layer was built to analyse the SE spectra. Each layer of the model has several fitting variables such as thickness and optical dispersion model parameters.

A value of the goodness of fit, which quantifies how well the data generated by the optical model (G) fit the experimental data (E), is derived from the root mean squared error (MSE) as defined by

$$\mathrm{MSE} = \sqrt{\frac{1}{3m-l}\sum_{i=1}^{m}[(N_{E_i} - N_{G_i})^2 + (C_{E_i} - C_{G_i})^2 + (S_{E_i} - S_{G_i})^2]} \times 1000, \quad \text{(A.1)}$$

where m is the number of wavelengths measured, l is the number of fit parameters, and $N = \cos(2\Psi)$, $C = \sin(2\Psi)\cos(\Delta)$, $S = \sin(2\Psi)\sin(\Delta)$.[225] The Levenberg-Marquardt nonlinear regression algorithm is used to minimise the MSE during the fitting process.

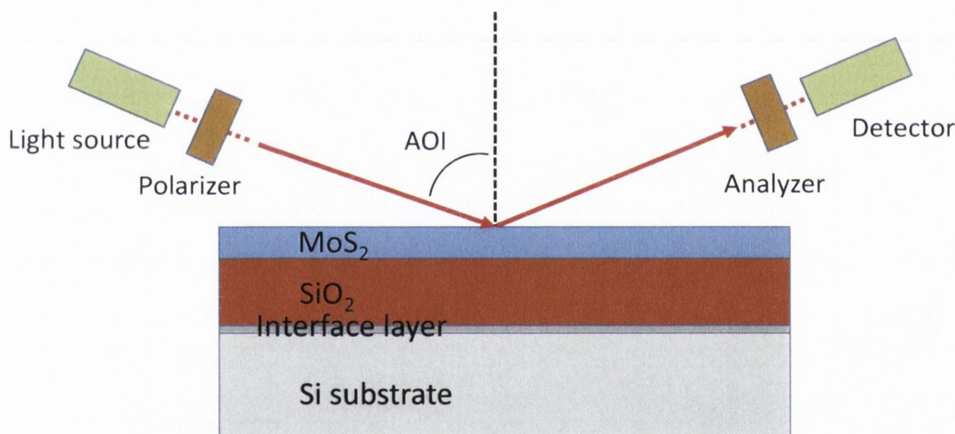

Figure A - 3 Schematic diagram of the optical model of MoS_2 samples and SE measurement system.

In a multilayer structure model, it is important to define the optical response of underlying layers in order to minimise optical correlation effects between layers and find more accurate values for the optical constants and the thickness of the top layer. Therefore, SE spectra of reference SiO_2/Si substrates, where Mo layers were not deposited, were first measured and analysed using a three-layer optical model composed of a Si substrate, an interface layer between Si and SiO_2 and a SiO_2 layer. It is assumed that the underlying layers are stable with well-established optical constants.[226] The crystalline Si substrate of the model can be presumed to have a semi-infinite thickness, so the thicknesses of the interface and SiO_2 layers were determined

from the fitting process. Then, the MoS_2 layer is added on top of the SiO_2 layer in the model structure, allowing its optical properties to be characterised in the presence of well-defined underlying layers.

A Tauc-Lorentz (T-L) oscillation model was used to determine the optical properties of the MoS_2 thin film. The complex dielectric function of the energy (E) is defined as $\varepsilon(E) = \varepsilon_1 + i\varepsilon_2$, and in the T-L model, ε_1 and ε_2 can be defined using Eq. (3.1) and Eq. (3.2).[176] The thickness of MoS_2 and the fitting parameters of the T-L oscillation model are varied until the best fit between experimental spectra and simulated data from the optical model is achieved with the lowest MSE values.

The experimental and simulated spectra (Ψ and Δ) for MoS_2 samples A, B, C, D and E are depicted in Figure A - 4, showing a good match between them. Extracted MoS_2 thickness values of the five samples (A, B, C, D and E) are 1.99 ± 0.01 nm, 3.01 ± 0.07 nm, 5.53 ± 0.08 nm, 9.83 ± 0.04 nm and 19.88 ± 0.05 nm, respectively. More details on fitting parameter values of the T-L oscillation model for the best fit are listed in Table A - 1.

In addition, X-ray reflectivity (XRR) measurements[§§§§] of the samples were carried out to verify the MoS_2 film thickness, using a Bruker D8-Discover X-ray diffractometer. Thickness values were obtained by fitting the XRR data using a computer simulation called LEPTOS. Thickness measurements of the MoS_2 thin films were performed by grazing incidence angle of XRR, and a representative plot of XRR data obtained from the sample E for the thickness measurement is depicted in Figure A - 5. Thickness values of the MoS_2 films (sample A, B, C, D and E) derived from SE and XRR measurements are summarised in Table A - 2. Thickness values of the sample A and B from XRR measurements are not available since the films were thinner than the minimum measurement limit (~5 nm) of XRR. The measured values from XRR were consistent with those extracted using the T-L oscillation model.

[§§§§] XRR analysis was carried out by Dr. Inam Mirza.

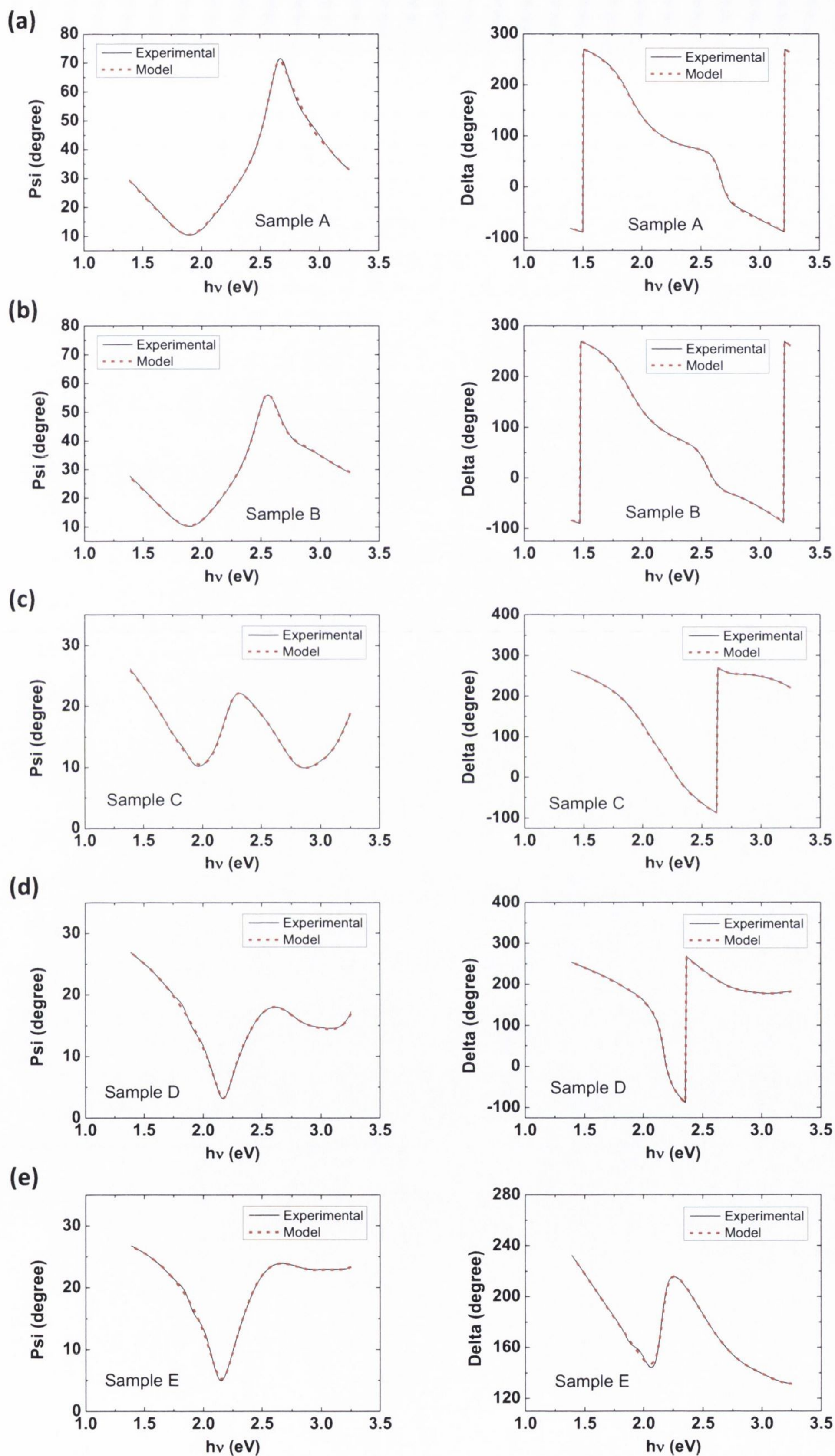

Figure A - 4 Plots of the experimental and simulated (model) SE spectra (psi and delta) of MoS_2 samples A – E ((a) – (e)).

Table A - 1 Thickness values of the MoS_2 thin films (sample A, B, C, D and E) from SE and fitting parameter values of the Tauc-Lorentz (T-L) oscillation model for the best fit.

Sample		A	B	C	D	E
Thickness [nm]		1.99 ± 0.01	3.01 ± 0.07	5.53 ± 0.08	9.83 ± 0.04	19.88 ± 0.05
$\varepsilon_1(\infty)$		1.15	0.92	0.92	0.99	0.97
	A_1 [eV]	5.46	9.58	27.84	16.13	10.75
T-L	C_1 [eV]	0.37	0.45	0.52	0.43	0.46
Oscillator 1	E_{01} [eV]	2.77	2.77	2.73	2.70	2.70
	E_{b1} [eV]	1.16	1.16	1.18	1.20	0.42
	A_2 [eV]	3.96	2.56	25.46	2.22	7.43
T-L	C_2 [eV]	0.31	0.31	0.38	0.36	0.44
Oscillator 2	E_{02} [eV]	2.03	2.07	1.94	1.97	1.92
	E_{b2} [eV]	0.23	0.16	1.32	0.01	0.64
	A_3 [eV]	0.01	70.17	43.53	18.83	47.13
T-L	C_3 [eV]	1.19	1.88	2.06	4.09	1.52
Oscillator 3	E_{03} [eV]	0.48	0.62	0.60	2.03	0.76
	E_{b3} [eV]	0.75	0.72	0.60	0.57	0.76
	A_4 [eV]	4.88	36.56	40.36	72.99	35.97
T-L	C_4 [eV]	0.44	0.67	0.84	1.02	0.84
Oscillator 4	E_{04} [eV]	3.03	3.03	3.07	2.94	3.00
	E_{b4} [eV]	0.37	1.96	1.42	1.49	1.35
MSE		4.10	7.07	3.61	4.43	5.17

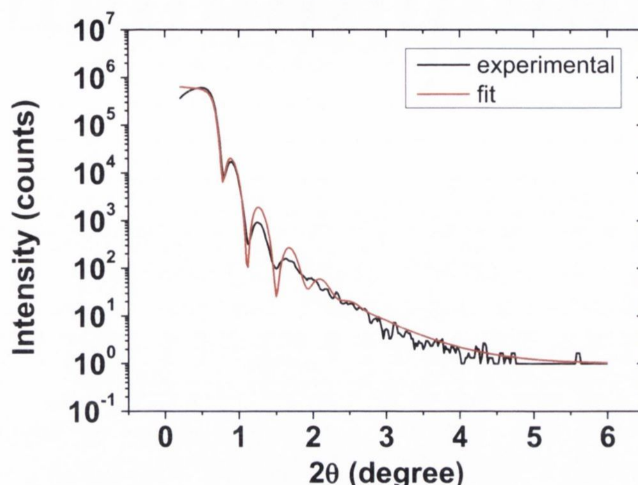

Figure A - 5 Representative plot of XRR data measured from sample E for the thickness measurement.

Table A - 2 Summary of the MoS_2 thickness values from SE data and XRR measurements for the five MoS_2 samples (sample A, B, C, D and E). Thickness values of samples A and B from XRR measurements are not available due to the thickness resolution limit of XRR.

	Sample	A	B	C	D	E
SE	Thickness [nm]	1.99 ± 0.01	3.01 ± 0.07	5.53 ± 0.08	9.83 ± 0.04	19.88 ± 0.05
XRR	Thickness [nm]	N.A	N.A	4.4 ± 1.4	9.9 ± 1.6	19.4 ± 1.6

Figure A - 6(a) and (b) show *n*/*k* values of the MoS_2 layer for each sample derived from the optical model with the best fits. Two dominant peaks are observed at the energy of ~2.0 eV and ~2.9 eV in the *k* plot, implying that there is an increase in optical absorption at these points. In addition, an absorbance spectrum of a MoS_2 thin film (~20 nm) on a quartz substrate was measured, as depicted in the inset of Figure A - 6(b). Two spectral regions with dominant absorption variations are observed in the photon energy range of 1.5 eV – 3.8 eV, which are related to A/B excitonic peaks in the range of 1.8 – 2.0 eV, and C/D excitonic peaks in the range of 2.7 – 3.1 eV, respectively.[122] This shows good agreement with the two *k* peaks observed at energies of ~2.0 eV and ~2.9 eV in the *k* plot.

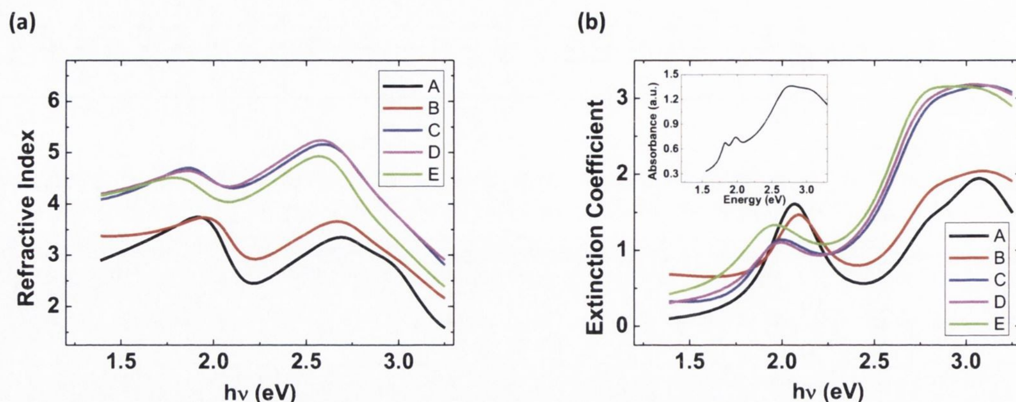

Figure A - 6 Plots of (a) the refractive index *n* and (b) extinction coefficient *k* values of the MoS_2 layers for the five samples (A, B, C, D and E) derived from the optical model with the best fits. The inset of (b) shows a UV-visible absorption spectrum of a MoS_2 thin film on a quartz substrate.

A.1.5 Optical Band Gap

Studies of the optical band gap energy of the MoS_2 thin films were also conducted using SE data. The optical absorption coefficient (α) of MoS_2 thin films can be calculated from the extinction coefficient k and wavelength λ by means of $\alpha = 4\pi k/\lambda$. The relationship between the absorption coefficient α and the photon energy can be expressed by

$$\alpha = \frac{K(hv-E_g)^m}{hv}, \qquad \text{(A.2)}$$

where K is a constant, hv is the incident photon energy and m is a number that characterises the transition process.[227,228] Depending on the transition type, m has a value of 1/2 for a direct transition and 2 for an indirect transition. Since the MoS_2 thin films being probed can be considered as multilayer MoS_2 films with thicknesses of 1.99 – 19.88 nm, it is believed that they have primarily indirect band gap transitions.[106] Thus, the variation of α with hv can be determined by using the relation of $(\alpha hv)^{1/2} \sim (hv - E_g)$ and the optical band gap E_g can be extracted by extrapolating the linear region of a $(\alpha hv)^{1/2}$ vs. hv plot to $(\alpha hv)^{1/2} = 0$. Plots of $(\alpha hv)^{1/2}$ vs. hv for the MoS_2 thin films (samples A, B, C, D and E) are shown in Figure A - 7.

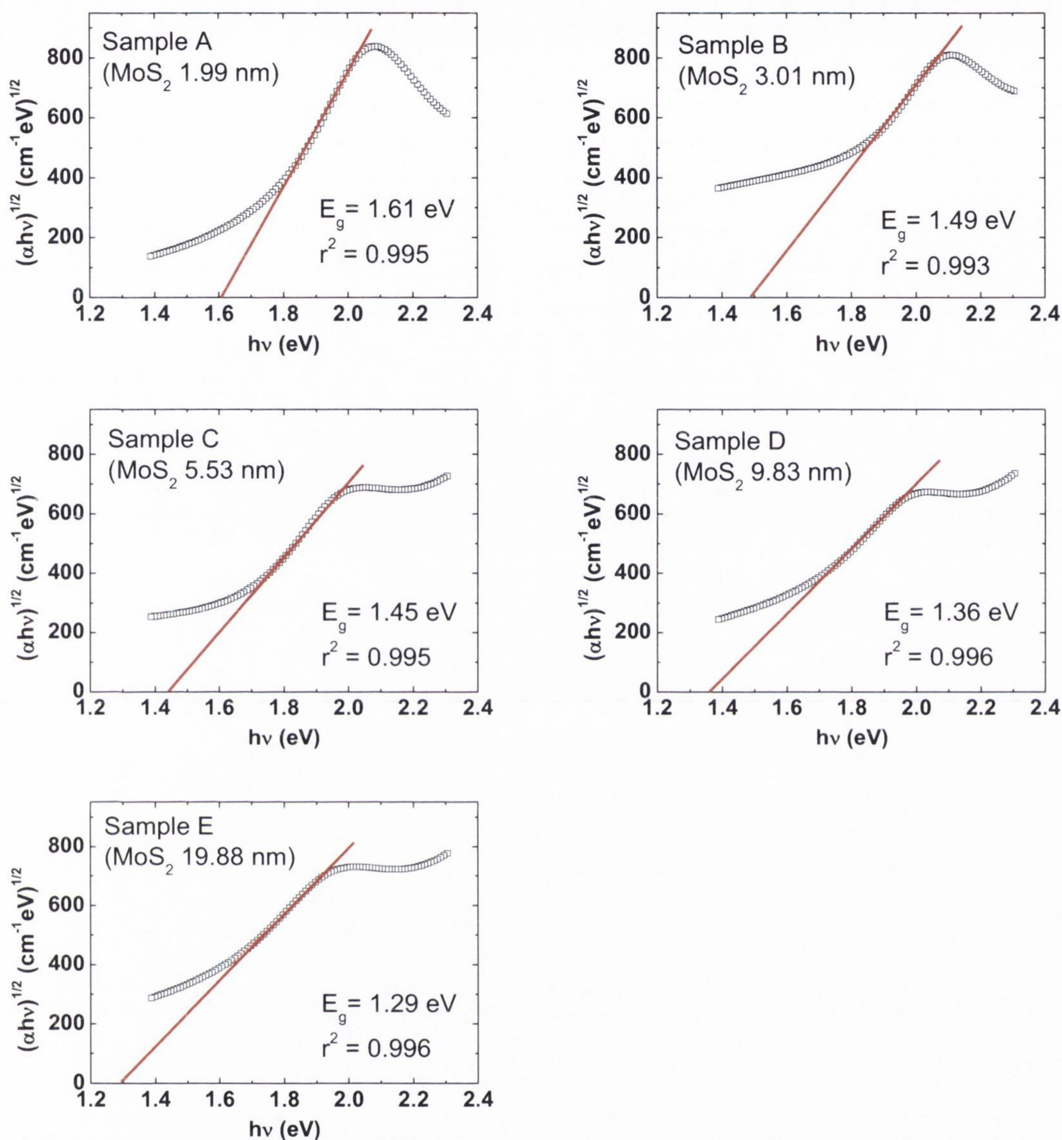

Figure A - 7 Plots of $(\alpha h\nu)^{1/2}$ vs. $h\nu$ for sample A, B, C, D and E. The extrapolation of the linear region to $(\alpha h\nu)^{1/2} = 0$ (red line) gives the E_g value.

The extracted E_g values of the five samples are 1.61 ± 0.03, 1.49 ± 0.03, 1.45 ± 0.02, 1.36 ± 0.02, and 1.29 ± 0.02 eV for samples A, B, C, D and E, respectively. It is evident that the thinner MoS_2 films have a larger E_g. The thinnest MoS_2 film (sample A) with a measured thickness of 1.99 nm shows the largest E_g (1.61 eV), and as the MoS_2 film thickness increases E_g decreases towards the band gap of bulk MoS_2 (~1.3 eV). These first ellipsometric measurements of layered MoS_2 films are comparable with previous reports on E_g of mechanically exfoliated single and multilayer MoS_2 from photoluminescence (PL) spectra,[106] as presented in Figure A - 8.

Lee *et al.*[110] also characterised the optical band gap energy of single and few layer mechanically exfoliated MoS_2 from electrical measurements of MoS_2 phototransistors and found that the band gap decreased in energy with increasing MoS_2 thickness. In addition, Eda *et al.*[122] observed a similar trend in E_g from chemically exfoliated MoS_2 using PL spectra measurements. This consistency is notable since it implies that vapour phase derived MoS_2 has comparable optical characteristics to those of exfoliated materials. This study further establishes SE as a viable tool for the characterisation of 2D materials as it can be used to investigate E_g of MoS_2, or indeed other TMDs (e.g., WTe_2, $MoSe_2$, etc.), while also giving information on optical constants and thicknesses. Such measurements are fast, non-destructive and relatively easy to perform.

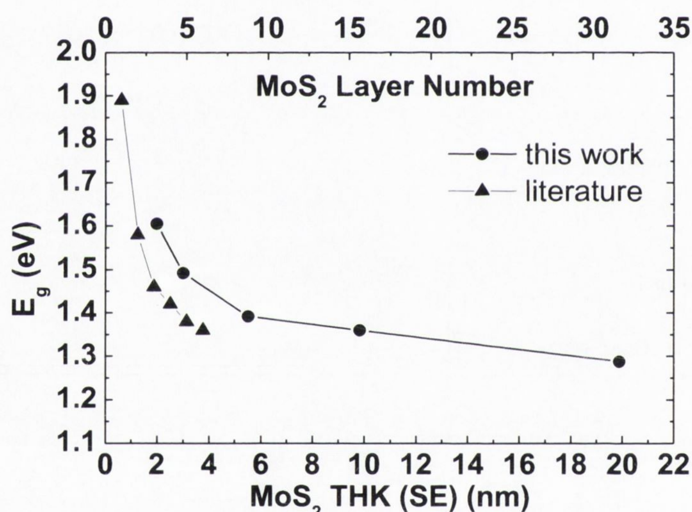

Figure A - 8 Plot of E_g vs. MoS_2 thickness/layer number obtained from this work (circle) and literature[106] (triangle). It is assumed that single layer MoS_2 thickness is 0.65 nm.

A.1.6 Conclusion

SE measurements have been carried out on MoS_2 thin films with different thicknesses synthesised by vapour phase sulfurisation. In addition, they were characterised by XRR, UV-visible absorption spectroscopy and Raman spectroscopy. An optical dispersion model of MoS_2 was developed for SE data analysis. Values of optical constants (n, k) and the thickness were determined by fitting the optical model function to the experimental data. The optical band gap energy E_g of the MoS_2 thin films was also investigated. Using the absorption coefficients of MoS_2 calculated from the

extracted k values, E_g of each MoS_2 film was extracted. The extracted E_g values of the MoS_2 films show a clear dependence on the MoS_2 film thickness, indicating that thinner MoS_2 films have a larger E_g. This study establishes SE as a promising technique for optical characterisation of TMD films.

List of Publications and Presentations

Publication: Parts of the results on this report have been reported on the list below.

P-1. **Chanyoung Yim**, Maria O'Brien, Niall McEvoy, Sarah Riazimehr, Heiko Schäfer-Eberwein, Andreas Bablich, Ravinder Pawar, Giuseppe Iannaccone, Clive Downing, Gianluca Fiori, Max C Lemme, Georg S Duesberg, "Heterojunction Hybrid Devices from Vapor Phase Grown MoS_2", *Scientific Reports*, 2014, **4**, 5458. (DOI: 10.1038/srep05458)

P-2. Hugo Nolan, Niall McEvoy, Maria O'Brien, Nina C Berner, **Chanyoung Yim**, Toby Hallam, Aidan R McDonald, and Georg Duesberg, "Molybdenum disulfide/pyrolytic carbon hybrid electrodes for scalable hydrogen evolution", *Nanoscale*, 2014, **6** (14), pp 8185-8191. (DOI: 10.1039/C4NR01528B)

P-3. Toby Hallam, Nina C Berner, **Chanyoung Yim**, and Georg S Duesberg, "Strain, Bubbles, Dirt, and Folds: A Study of Graphene Polymer-Assisted Transfer", *Advanced Materials Interfaces*, 2014, Published Online (7 May 2014). (DOI: 10.1002/admi.201400115)

P-4. **Chanyoung Yim**, Maria O'Brien, Niall McEvoy, Sinéad Winters, Inam Mirza, James G Lunney, and Georg S Duesberg, "Investigation of the optical properties of MoS_2 thin films using spectroscopic ellipsometry", *Applied Physics Letters*, 2014, **104** (10), 103114. (DOI: 10.1063/1.4868108)

P-5. **Chanyoung Yim**, Niall McEvoy, and Georg S Duesberg, "Characterization of graphene-silicon Schottky barrier diodes using impedance spectroscopy", *Applied Physics Letters*, 2013, **103** (19), 193106. (DOI: 10.1063/1.4829140)

P-6. Georg S Duesberg, Hye-Young Kim, Kangho Lee, Niall McEvoy, Sinead Winters, and **Chanyoung Yim**, "Investigation of carbon-silicon Schottky diodes and their use as chemical sensors", *2013 Proceedings of the European Solid-State Device Research Conference (ESSDERC)* (Bucharest, Romania, September 16-20, 2013) pp 85-90. (DOI: 10.1109/ESSDERC.2013.6818825)

P-7. **Chanyoung Yim**, Niall McEvoy, Hye-Young Kim, Ehsan Rezvani, and Georg S Duesberg, "Investigation of the Interfaces in Schottky Diodes using

Equivalent Circuit Models", *ACS Applied materials & Interfaces*, 2013, **5** (15), pp 6951–6958. (DOI: 10.1021/am400963x)

P-8. Hye-Young Kim, Kangho Lee, Niall McEvoy, **Chanyoung Yim**, and Georg S. Duesberg, "Chemically Modulated Graphene Diodes", *Nano Letters*, 2013, **13** (5), pp 2182-2188. (DOI: 10.1021/nl400674k)

P-9. **Chanyoung Yim**, Ehsan Rezvani, Shishir Kumar, Niall McEvoy, and Georg S. Duesberg, "Investigation of carbon–silicon Schottky barrier diodes", *Physica Status Solidi (b)*, 2012, **249** (12), pp 2553–2557. (DOI: 10.1002/pssb.201200106)

P-10. **Chanyoung Yim**, Niall McEvoy, Ehsan Rezvani, Shishir Kumar, and Georg S. Duesberg, "Carbon–Silicon Schottky Barrier Diodes", *Small*, 2012, **8** (9), pp 1360-1364. (DOI: 10.1002/smll.201101996)

Patent

1. UK Patent (GB1201390.0), "Carbon-Si Schottky Barrier Diode and Method of Making Same" in application. (January, 2012)

Presentation

1. "Investigation of Photodiodes from Vapour Phase Grown MoS_2", Trends in Nanotechnology International Conference (TNT2014), October 27 – 31, 2014. Barcelona, Spain. (Talk)
2. "Photodiodes from Vapour Phase Grown MoS_2", Flatlands beyond Graphene 2014, July 9 – 11, 2014. Trinity Biomedical Sciences Institute (TBSI) and Centre for Research on Adaptive Nanostructures and Nanodevices (CRANN), Trinity College Dublin, Dublin, Ireland. (Poster: Best Poster Award)
3. "Electrical Characteristics of Graphene-Silicon Schottky Barrier Diodes", Intel Ireland Research Conference 2013, November 21 – 22, 2013. Clontarf Castle, Dublin, Ireland. (Poster)
4. "Investigation of Carbon-Silicon Schottky Contacts in Diode Devices", AMBER Launch & Research Day, October 24, 2013. Croke Park, Dublin, Ireland. (Poster)

5. "Investigation of Carbon-Silicon Schottky Barrier Diodes", 2013 Nanodays Workshop, October 10, 2013. Fraunhofer IGB, Stuttgart, Germany. (Talk)
6. "Impedance Analysis for the Interface of Carbon-Silicon Schottky Contact in Diode Devices", The 14th International Conference on the Formation of Semiconductor Interfaces (ICFSI-14), June 30 – July 05, 2013. Gyeongju, South Korea. (Poster)
7. "Electrical Analysis for the Interface of Carbon-Silicon Schottky Contacts", Intel Ireland Research Conference 2012 – Intel ERIC Series 2012, October 03 – 04, 2012. Croke Park, Dublin, Ireland. (Poster)
8. "Investigation of Carbon-Silicon Schottky Barrier Diode", 26th International Winterschool on Electronic Properties of Novel Materials (IWEPNM 2012), March 3 – 10, 2012. Kirchberg, Austria. (Poster)
9. "Investigation of Pyrolytic Carbon-Silicon Schottky Barrier Diode", Intel European Research & Innovation Conference 2011, October 12 – 14, 2011. Leixlip, Intel Ireland Ltd. (Poster)

References

1 Terrones, M. *et al.* Graphene and graphite nanoribbons: Morphology, properties, synthesis, defects and applications. *Nano Today* **5**, 351-372 (2010).

2 Falcao, E. H. L. & Wudl, F. Carbon allotropes: beyond graphite and diamond. *J. Chem. Technol. Biotechnol.* **82**, 524-531 (2007).

3 Wissler, M. Graphite and carbon powders for electrochemical applications. *J. Power Sources* **156**, 142-150 (2006).

4 Celzard, A., Marêché, J. F. & Furdin, G. Modelling of exfoliated graphite. *Progress in Materials Science* **50**, 93-179 (2005).

5 Goss, J. P., Eyre, R. J. & Briddon, P. R. in *Physics and Applications of CVD Diamond* 199-236 (Wiley-VCH Verlag GmbH & Co. KGaA, 2008).

6 Wort, C. J. H. & Balmer, R. S. Diamond as an electronic material. *Mater. Today* **11**, 22-28 (2008).

7 Gicquel, A., Hassouni, K., Silva, F. & Achard, J. CVD diamond films: from growth to applications. *Curr. Appl. Phys.* **1**, 479-496 (2001).

8 Graham, A. P. *et al.* Carbon Nanotubes for Microelectronics? *Small* **1**, 382-390 (2005).

9 Hoenlein, W. *et al.* Carbon nanotubes for microelectronics: status and future prospects. *Mater. Sci. Eng. C* **23**, 663-669 (2003).

10 Wu, J., Pisula, W. & Müllen, K. Graphenes as Potential Material for Electronics. *Chem. Rev.* **107**, 718-747 (2007).

11 Novoselov, K. S. *et al.* Electric Field Effect in Atomically Thin Carbon Films. *Science* **306**, 666-669 (2004).

12 Novoselov, K. S. *et al.* Two-dimensional gas of massless Dirac fermions in graphene. *Nature* **438**, 197-200 (2005).

13 Zhang, Y., Tan, Y.-W., Stormer, H. L. & Kim, P. Experimental observation of the quantum Hall effect and Berry's phase in graphene. *Nature* **438**, 201-204 (2005).

14 Katsnelson, M. I. Graphene: carbon in two dimensions. *Mater. Today* **10**, 20-27 (2007).

15 Kim, H.-G., Ahn, S.-H., Kim, J.-G., Park, S. J. & Lee, K.-R. Electrochemical behavior of diamond-like carbon films for biomedical applications. *Thin Solid Films* **475**, 291-297 (2005).

16 Jenkins, G. M. & Kawamura, K. *Polymeric carbons : carbon fibre, glass and char.* (Cambridge University Press, 2011).

17 McDermott, M. T., McDermott, C. A. & McCreery, R. L. Scanning tunneling microscopy of carbon surfaces: relationships between electrode kinetics, capacitance, and morphology for glassy carbon electrodes. *Anal. Chem.* **65**, 937-944 (1993).

18 McDermott, M. T. & McCreery, R. L. Scanning Tunneling Microscopy of Ordered Graphite and Glassy Carbon Surfaces: Electronic Control of Quinone Adsorption. *Langmuir* **10**, 4307-4314 (1994).

19 Harris, P. J. F. New Perspectives on the Structure of Graphitic Carbons. *Crit. Rev. Solid State Mater. Sci.* **30**, 235-253 (2005).

20 Masheter, A. T. *et al.* Voltammetric and X-ray photoelectron spectroscopic fingerprinting of carboxylic acid groups on the surface of carbon nanotubes via derivatisation with arylnitro labels. *J. Mater. Chem.* **17**, 3515-3524 (2007).

21 Hutton, H. D. *et al.* Preparation of nanoscale platinum(0) clusters in glassy carbon and their catalytic activity. *Chem. Mater.* **5**, 1727-1738 (1993).

22 Hutton, H. D. *et al.* Synthesis, characterization, and electrochemical activity of halogen-doped glassy carbon. *Chem. Mater.* **5**, 1110-1117 (1993).

23 Callstrom, M. R., Neenan, T. X., McCreery, R. L. & Alsmeyer, D. C. Doped glassy carbon materials (DGC): low-temperature synthesis, structure, and catalytic behavior. *J. Am. Chem. Soc.* **112**, 4954-4956 (1990).

24 McCreery, R. L. Advanced Carbon Electrode Materials for Molecular Electrochemistry. *Chem. Rev.* **108**, 2646-2687 (2008).

25 Manoharan, M. P., Lee, H., Rajagopalan, R., Foley, H. C. & Haque, M. A. Elastic Properties of 4-6 nm-thick Glassy Carbon Thin Films. *Nanoscale Res. Lett.* **5**, 14-19 (2010).

26 Kim, J., Song, X., Kinoshita, K., Madou, M. & White, B. Electrochemical studies of carbon films from pyrolyzed photoresist. *J. Electrochem. Soc.* **145**, 2314-2319 (1998).

27 Kostecki, R. *et al.* Surface studies of carbon films from pyrolyzed photoresist. *Thin Solid Films* **396**, 36-43 (2001).

28 Schreiber, M. *et al.* Transparent ultrathin conducting carbon films. *Appl. Surf. Sci.* **256**, 6186-6190 (2010).

29 Zoski, C. G. *Handbook of Electrochemistry* 111-153 (Elsevier B.V., 2007).

30 Ranganathan, S., McCreery, R., Majji, S. M. & Madou, M. Photoresist-Derived Carbon for Microelectromechanical Systems and Electrochemical Applications. *J. Electrochem. Soc.* **147**, 277-282 (2000).

31 Kostecki, R., Song, X. Y. & Kinoshita, K. Influence of Geometry on the Electrochemical Response of Carbon Interdigitated Microelectrodes. *J. Electrochem. Soc.* **147**, 1878-1881 (2000).

32 Ranganathan, S. & McCreery, R. L. Electroanalytical Performance of Carbon Films with Near-Atomic Flatness. *Anal. Chem.* **73**, 893-900 (2001).

33 Lyons, A. M. Photodefinable carbon films: Electrical properties. *J. Non-Cryst. Solids* **70**, 99-109 (1985).

34 Lyons, A. M., Hale, L. P. & Wilkins, J. C. W. Photodefinable carbon films: Control of image quality. *J. Vac. Sci. Technol. B* **3**, 447-452 (1985).

35 Reznik, B. & Hüttinger, K. J. On the terminology for pyrolytic carbon. *Carbon* **40**, 621-624 (2002).

36 Lieberman, M. L. & Pierson, H. O. Effect of gas phase conditions on resultant matrix pyrocarbons in carbon/carbon composites. *Carbon* **12**, 233-241 (1974).

37 Pierson, H. O. & Lieberman, M. L. The chemical vapor deposition of carbon on carbon fibers. *Carbon* **13**, 159-166 (1975).

38 Oberlin, A. Pyrocarbons. *Carbon* **40**, 7-24 (2002).

39 Benzinger, W., Becker, A. & Hüttinger, K. J. Chemistry and kinetics of chemical vapour deposition of pyrocarbon: I. Fundamentals of kinetics and chemical reaction engineering. *Carbon* **34**, 957-966 (1996).

40 Benzinger, W. & Hüttinger, K. J. Chemical vapour infiltration of pyrocarbon: I. Some kinetic considerations. *Carbon* **34**, 1465-1471 (1996).

41 McEvoy, N. *et al.* Synthesis and analysis of thin conducting pyrolytic carbon films. *Carbon* **50**, 1216-1226 (2012).

42 Koster, A., Matzner, H. D. & Nicholsi, D. R. PBMR design for the future. *Nucl. Eng. Des.* **222**, 231-245 (2003).

43 Wen, C.-Y. & Huang, G.-W. Application of a thermally conductive pyrolytic graphite sheet to thermal management of a PEM fuel cell. *J. Power Sources* **178**, 132-140 (2008).

44 Brückmann, H. & Hüttinger, K. J. Carbon, a promising material in endoprosthetics. Part 1: the carbon materials and their mechanical properties. *Biomaterials* **1**, 67-72 (1980).

45 PesÁkovÁ, V., Kle´zl, Z., Bali´k, K. & Adam, M. Biomechanical and biological properties of the implant material carbon-carbon composite covered with pyrolytic carbon. *J. Mater. Sci.: Mater. Med.* **11**, 793-798 (2000).

46 Taylor, C. A. & Chiu, W. K. S. Characterization of CVD carbon films for hermetic optical fiber coatings. *Surf. Coat. Technol.* **168**, 1-11 (2003).

47 Kreupl, F. in *2010 MRS Fall meeting.* 3-14 (MRS Online Proc Library 2011).

48 Graham, A. P., Schindler, G., Duesberg, G. S., Lutz, T. & Weber, W. An investigation of the electrical properties of pyrolytic carbon in reduced dimensions: Vias and wires. *J. Appl. Phys.* **107**, 114316 (2010).

49 Graham, A. P. *et al.* An investigation of the electrical properties of the interface between pyrolytic carbon and silicon for Schottky diode applications. *J. Appl. Phys.* **111**, 124511 (2012).

50 Yim, C., McEvoy, N., Rezvani, E., Kumar, S. & Duesberg, G. S. Carbon-Silicon Schottky Barrier Diodes. *Small* **8**, 1360-1364 (2012).

51 Yim, C., Rezvani, E., Kumar, S., McEvoy, N. & Duesberg, G. S. Investigation of carbon–silicon Schottky barrier diodes. *Phys. Status Solidi B* **249**, 2553-2557 (2012).

52 Raghavan, G., Hoyt, J. L. & Gibbons, J. F. Polycrystalline Carbon: A Novel Material for Gate Electrodes in MOS Technology. *Jpn. J. Appl. Phys.* **32**, 380-383 (1993).

53 Aichmayr, G. *et al.* Carbon / high-k Trench Capacitor for the 40nm DRAM Generation. *2007 Symposium on VLSI Technology Digest of Technical Papers* **10B**, 186-187 (2007).

54 Graham, A. P. *et al.* An investigation of the electrical properties of metal-insulator-silicon capacitors with pyrolytic carbon electrodes. *J. Appl. Phys.* **108**, 104508 (2010).

55 Castro Neto, A. H., Guinea, F., Peres, N. M. R., Novoselov, K. S. & Geim, A. K. The electronic properties of graphene. *Rev. Mod. Phys.* **81**, 109-162 (2009).

56 Wallace, P. R. The Band Theory of Graphite. *Physical Review* **71**, 622-634 (1947).

57 Slonczewski, J. C. & Weiss, P. R. Band Structure of Graphite. *Physical Review* **109**, 272-279 (1958).

58 Geim, A. K. & Novoselov, K. S. The rise of graphene. *Nat. Mater.* **6**, 183-191 (2007).

59 Semenoff, G. W. Condensed-Matter Simulation of a Three-Dimensional Anomaly. *Phys. Rev. Lett.* **53**, 2449-2452 (1984).

60 DiVincenzo, D. P. & Mele, E. J. Self-consistent effective-mass theory for intralayer screening in graphite intercalation compounds. *Phys. Rev. B* **29**, 1685-1694 (1984).

61 Novoselov, K. S. *et al.* Two-dimensional atomic crystals. *Proc. Natl. Acad. Sci. U. S. A.* **102**, 10451-10453 (2005).

62 Bolotin, K. I. *et al.* Ultrahigh electron mobility in suspended graphene. *Solid State Commun.* **146**, 351-355 (2008).

63 Morozov, S. V. *et al.* Giant Intrinsic Carrier Mobilities in Graphene and Its Bilayer. *Phys. Rev. Lett.* **100**, 016602 (2008).

64 Lee, C., Wei, X., Kysar, J. W. & Hone, J. Measurement of the Elastic Properties and Intrinsic Strength of Monolayer Graphene. *Science* **321**, 385-388 (2008).

65 Balandin, A. A. *et al.* Superior Thermal Conductivity of Single-Layer Graphene. *Nano Lett.* **8**, 902-907 (2008).

66 Cai, W., Zhu, Y., Li, X., Piner, R. D. & Ruoff, R. S. Large area few-layer graphene/graphite films as transparent thin conducting electrodes. *Appl. Phys. Lett.* **95**, 123115 (2009).

67 Li, X. *et al.* Transfer of Large-Area Graphene Films for High-Performance Transparent Conductive Electrodes. *Nano Lett.* **9**, 4359-4363 (2009).

68 Lin, Y.-M. *et al.* Operation of Graphene Transistors at Gigahertz Frequencies. *Nano Lett.* **9**, 422-426 (2008).

69 Lin, Y. M. *et al.* 100-GHz Transistors from Wafer-Scale Epitaxial Graphene. *Science* **327**, 662-662 (2010).

70 Yu-Ming, L. *et al.* Dual-Gate Graphene FETs With f_T of 50 GHz. *IEEE Electron Device Lett.* **31**, 68-70 (2010).

71 Liao, L. *et al.* High-speed graphene transistors with a self-aligned nanowire gate. *Nature* **467**, 305-308 (2010).

72 Xia, F., Farmer, D. B., Lin, Y.-m. & Avouris, P. Graphene Field-Effect Transistors with High On/Off Current Ratio and Large Transport Band Gap at Room Temperature. *Nano Lett.* **10**, 715-718 (2010).

73 Wu, Y. *et al.* State-of-the-Art Graphene High-Frequency Electronics. *Nano Lett.* **12**, 3062-3067 (2012).

74 Son, Y.-W., Cohen, M. L. & Louie, S. G. Energy Gaps in Graphene Nanoribbons. *Phys. Rev. Lett.* **97**, 216803 (2006).

75 Han, M. Y., Özyilmaz, B., Zhang, Y. & Kim, P. Energy Band-Gap Engineering of Graphene Nanoribbons. *Phys. Rev. Lett.* **98**, 206805 (2007).

76 Barone, V., Hod, O. & Scuseria, G. E. Electronic Structure and Stability of Semiconducting Graphene Nanoribbons. *Nano Lett.* **6**, 2748-2754 (2006).

77 Ohta, T., Bostwick, A., Seyller, T., Horn, K. & Rotenberg, E. Controlling the Electronic Structure of Bilayer Graphene. *Science* **313**, 951-954 (2006).

78 Castro, E. V. *et al.* Biased Bilayer Graphene: Semiconductor with a Gap Tunable by the Electric Field Effect. *Phys. Rev. Lett.* **99**, 216802 (2007).

79 Zhang, Y. *et al.* Direct observation of a widely tunable bandgap in bilayer graphene. *Nature* **459**, 820-823 (2009).

80 Yu, W. J., Liao, L., Chae, S. H., Lee, Y. H. & Duan, X. Toward Tunable Band Gap and Tunable Dirac Point in Bilayer Graphene with Molecular Doping. *Nano Lett.* **11**, 4759-4763 (2011).

81 Zhang, H. *et al.* Aryl Functionalization as a Route to Band Gap Engineering in Single Layer Graphene Devices. *Nano Lett.* **11**, 4047-4051 (2011).

82 Park, J. *et al.* Band gap formation in graphene by in-situ doping. *Appl. Phys. Lett.* **98**, 203102 (2011).

83 Stankovich, S. *et al.* Synthesis of graphene-based nanosheets via chemical reduction of exfoliated graphite oxide. *Carbon* **45**, 1558-1565 (2007).

84 Eda, G., Fanchini, G. & Chhowalla, M. Large-area ultrathin films of reduced graphene oxide as a transparent and flexible electronic material. *Nat. Nanotechnol.* **3**, 270-274 (2008).

85 Park, S. & Ruoff, R. S. Chemical methods for the production of graphenes. *Nat. Nanotechnol.* **4**, 217-224 (2009).

86 Hernandez, Y. *et al.* High-yield production of graphene by liquid-phase exfoliation of graphite. *Nat. Nanotechnol.* **3**, 563-568 (2008).

87 Coleman, J. N. Liquid Exfoliation of Defect-Free Graphene. *Acc. Chem. Res.* **46**, 14-22 (2012).

88 Wintterlin, J. & Bocquet, M. L. Graphene on metal surfaces. *Surf. Sci.* **603**, 1841-1852 (2009).

89 Li, X. *et al.* Large-Area Synthesis of High-Quality and Uniform Graphene Films on Copper Foils. *Science* **324**, 1312-1314 (2009).

90 Li, X., Cai, W., Colombo, L. & Ruoff, R. S. Evolution of Graphene Growth on Ni and Cu by Carbon Isotope Labeling. *Nano Lett.* **9**, 4268-4272 (2009).

91 Lee, Y. *et al.* Wafer-Scale Synthesis and Transfer of Graphene Films. *Nano Lett.* **10**, 490-493 (2010).

92 Losurdo, M., Giangregorio, M. M., Capezzuto, P. & Bruno, G. Graphene CVD growth on copper and nickel: role of hydrogen in kinetics and structure. *Phys. Chem. Chem. Phys.* **13**, 20836-20843 (2011).

93 Li, X. *et al.* Large-Area Graphene Single Crystals Grown by Low-Pressure Chemical Vapor Deposition of Methane on Copper. *J. Am. Chem. Soc.* **133**, 2816-2819 (2011).

94 Kumar, S. *et al.* CVD growth and processing of graphene for electronic applications. *Phys. Status Solidi B* **248**, 2604-2608 (2011).

95 Kang, J., Shin, D., Bae, S. & Hong, B. H. Graphene transfer: key for applications. *Nanoscale* **4**, 5527-5537 (2012).

96 Song, J. *et al.* A general method for transferring graphene onto soft surfaces. *Nat. Nanotechnol.* **8**, 356-362 (2013).

97 Lin, W.-H. *et al.* A Direct and Polymer-Free Method for Transferring Graphene Grown by Chemical Vapor Deposition to Any Substrate. *ACS Nano* **Published Online (January 28, 2014), DOI: 10.1021/nn406170d** (2014).

98 Gorantla, S. *et al.* A universal transfer route for graphene. *Nanoscale* (2014).

99 de Heer, W. A. *et al.* Epitaxial graphene. *Solid State Commun.* **143**, 92-100 (2007).

100 Hass, J., Heer, W. A. d. & Conrad, E. H. The growth and morphology of epitaxial multilayer graphene. *J. Phys.: Condens. Matter* **20**, 323202 (2008).

101 Emtsev, K. V. *et al.* Towards wafer-size graphene layers by atmospheric pressure graphitization of silicon carbide. *Nat. Mater.* **8**, 203-207 (2009).

102 Aristov, V. Y. *et al.* Graphene Synthesis on Cubic SiC/Si Wafers. Perspectives for Mass Production of Graphene-Based Electronic Devices. *Nano Lett.* **10**, 992-995 (2010).

103 Neto, A. H. C. & Novoselov, K. Two-Dimensional Crystals: Beyond Graphene. *Materials Express* **1**, 10-17 (2011).

104 Novoselov, K. S. Nobel Lecture: Graphene: Materials in the Flatland. *Rev. Mod. Phys.* **83**, 837-849 (2011).

105 Wang, Q. H., Kalantar-Zadeh, K., Kis, A., Coleman, J. N. & Strano, M. S. Electronics and optoelectronics of two-dimensional transition metal dichalcogenides. *Nat. Nanotechnol.* **7**, 699-712 (2012).

106 Mak, K. F., Lee, C., Hone, J., Shan, J. & Heinz, T. F. Atomically Thin MoS_2: A New Direct-Gap Semiconductor. *Phys. Rev. Lett.* **105**, 136805 (2010).

107 Splendiani, A. *et al.* Emerging Photoluminescence in Monolayer MoS2. *Nano Lett.* **10**, 1271-1275 (2010).

108 Korn, T., Heydrich, S., Hirmer, M., Schmutzler, J. & Schüller, C. Low-temperature photocarrier dynamics in monolayer MoS2. *Appl. Phys. Lett.* **99**, 102109 (2011).

109 Radisavljevic, B., Radenovic, A., Brivio, J., Giacometti, V. & Kis, A. Single-layer MoS2 transistors. *Nat. Nanotechnol.* **6**, 147-150 (2011).

110 Lee, H. S. *et al.* MoS2 Nanosheet Phototransistors with Thickness-Modulated Optical Energy Gap. *Nano Lett.* **12**, 3695-3700 (2012).

111 Radisavljevic, B. & Kis, A. Mobility engineering and a metal–insulator transition in monolayer MoS2. *Nat. Mater.* **12**, 815-820 (2013).

112 Chhowalla, M. *et al.* The chemistry of two-dimensional layered transition metal dichalcogenide nanosheets. *Nature Chemistry* **5**, 263-275 (2013).

113 Ganatra, R. & Zhang, Q. Few-Layer MoS2: A Promising Layered Semiconductor. *ACS Nano* **8**, 4074-4099 (2014).

114 Lopez-Sanchez, O., Lembke, D., Kayci, M., Radenovic, A. & Kis, A. Ultrasensitive photodetectors based on monolayer MoS2. *Nat. Nanotechnol.* **8**, 497-501 (2013).

115 Wu, W. *et al.* High mobility and high on/off ratio field-effect transistors based on chemical vapor deposited single-crystal MoS_2 grains. *Appl. Phys. Lett.* **102**, 142106 (2013).

116 Radisavljevic, B., Whitwick, M. B. & Kis, A. Integrated Circuits and Logic Operations Based on Single-Layer MoS2. *ACS Nano* **5**, 9934-9938 (2011).

117 Liu, L., Lu, Y. & Guo, J. On Monolayer MoS_2 Field-Effect Transistors at the Scaling Limit. *IEEE Trans. Electron Dev.* **60**, 4133-4139 (2013).

118 Yin, Z. *et al.* Single-Layer MoS2 Phototransistors. *ACS Nano* **6**, 74-80 (2012).

119 Zhao, W. *et al.* Origin of Indirect Optical Transitions in Few-Layer MoS_2, WS_2, and WSe_2. *Nano Lett.* **13**, 5627-5634 (2013).

120 Coleman, J. N. *et al.* Two-Dimensional Nanosheets Produced by Liquid Exfoliation of Layered Materials. *Science* **331**, 568-571 (2011).

121 Zeng, Z. *et al.* Single-Layer Semiconducting Nanosheets: High-Yield Preparation and Device Fabrication. *Angewandte Chemie International Edition* **50**, 11093-11097 (2011).

122 Eda, G. *et al.* Photoluminescence from Chemically Exfoliated MoS2. *Nano Lett.* **11**, 5111-5116 (2011).

123 Xu, M., Liang, T., Shi, M. & Chen, H. Graphene-Like Two-Dimensional Materials. *Chem. Rev.* **113**, 3766-3798 (2013).

124 Lee, Y.-H. *et al.* Synthesis of Large-Area MoS2 Atomic Layers with Chemical Vapor Deposition. *Adv. Mater.* **24**, 2320-2325 (2012).

125 Zhan, Y., Liu, Z., Najmaei, S., Ajayan, P. M. & Lou, J. Large-Area Vapor-Phase Growth and Characterization of MoS2 Atomic Layers on a SiO2 Substrate. *Small* **8**, 966-971 (2012).

126 Lin, Y.-C. *et al.* Wafer-scale MoS2 thin layers prepared by MoO3 sulfurization. *Nanoscale* **4**, 6637-6641 (2012).

127 Liu, K.-K. *et al.* Growth of Large-Area and Highly Crystalline MoS2 Thin Layers on Insulating Substrates. *Nano Lett.* **12**, 1538-1544 (2012).

128 Vanmeirhaeghe, R. L., Laflere, W. H. & Cardon, F. Influence of defect passivation by hydrogen on the Schottky-barrier height of GaAs and InP contacts. *J. Appl. Phys.* **76**, 403-406 (1994).

129 Prokopyev, A. I. & Mesheryakov, S. A. Restrictions of forward I-V methods for determination of Schottky diode parameters. *Measurement* **33**, 135-144 (2003).

130 Neamen, D. A. *Semiconductor Physics and Devices*. Third Edition edn, 326 (McGraw Hill, 2003).

131 Jung, C. *et al.* in *20th International Symposium on Space Terahertz Technology.* 255 -256.

132 Liu, J.-m. *Photonic Devices*. (Cambridge University Press, 2005).

133 Saleh, B. E. A. & Teich, M. C. *Fundamentals of Photonics*. 2nd edn, (John Wiley & Sons, Inc., 2007).

134 Yan, X.-T. & Xu, Y. *Chemical Vapour Deposition*. 1st edn, (Springer, 2010).

135 Egerton, R. F. *Physical Principles of Electron Microscopy*. 1st edn, 34 (Springer, 2005).

136 *Atomic World - Transmission Electron Microscope (TEM) - Principle of TEM*, <http://www.hk-phy.org/atomic_world/tem/tem02_e.html> (2010).

137 *Scanning Electron Microscope*, <http://www.purdue.edu/rem/rs/sem.htm> (2009).

138 Wang, Y., Alsmeyer, D. C. & McCreery, R. L. Raman spectroscopy of carbon materials: structural basis of observed spectra. *Chem. Mater.* **2**, 557-563 (1990).

139 Pimenta, M. A. *et al.* Studying disorder in graphite-based systems by Raman spectroscopy. *Phys. Chem. Chem. Phys.* **9**, 1276-1290 (2007).

140 Ferrari, A. C. Raman spectroscopy of graphene and graphite: Disorder, electron–phonon coupling, doping and nonadiabatic effects. *Solid State Commun.* **143**, 47-57 (2007).

141 Wang, Y. y. *et al.* Raman Studies of Monolayer Graphene: The Substrate Effect. *J. Phys. Chem. C* **112**, 10637-10640 (2008).

142 Ferrari, A. C. *et al.* Raman Spectrum of Graphene and Graphene Layers. *Phys. Rev. Lett.* **97**, 187401 (2006).

143 Li, H. *et al.* From Bulk to Monolayer MoS2: Evolution of Raman Scattering. *Adv. Funct. Mater.* **22**, 1385-1390 (2012).

144 Bertrand, P. A. Surface-phonon dispersion of MoS2. *Phys. Rev. B* **44**, 5745-5749 (1991).

145 Fujiwara, H. *Spectroscopic ellipsometry : principles and applications*. (John Wiley & Sons Ltd, 2007).

146 Woollam, J. A. *CompleteEASE Data Analysis Manual*. Ver. 4.63 edn, (J. A. Woollam Co., Inc., 2011).

147 Keithley-Instruments. *Low Level Measurements Handbook*. 6th edn, (Keithley Instruments, Inc., 2004).

148 Barsoukov, E. & Macdonald, J. R. *Impedance spectroscopy : theory, experiment, and applications*. 2nd edn, (John Wiley & Sons, Inc., 2005).

149 Jonda, C. & Mayer, A. B. R. Investigation of the Electronic Properties of Organic Light-Emitting Devices by Impedance Spectroscopy. *Chem. Mater.* **11**, 2429-2435 (1999).

150 Huang, J. *et al.* Study on carrier mobility measurement using electroluminescence in frequency domain and electrochemical impedance spectroscopy. *Measurement* **43**, 295-298 (2010).

151 Chen, C.-C. *et al.* Impedance spectroscopy and equivalent circuits of conductively doped organic hole-transport materials. *Org. Electron.* **11**, 1901-1908 (2010).

152 Reddy, V. S., Das, S., Ray, S. K. & Dhar, A. Studies on conduction mechanisms of pentacene based diodes using impedance spectroscopy. *J. Phys. D: Appl. Phys.* **40**, 7687 (2007).

153 Huang, W., Peng, J., Wang, L., Wang, J. & Cao, Y. Impedance spectroscopy investigation of electron transport in solar cells based on blend film of polymer and nanocrystals. *Appl. Phys. Lett.* **92**, 013308 (2008).

154 Agarwal, P., Crisalle, O. D., Orazem, M. E. & GarciaRubio, L. H. Application of measurement models to impedance spectroscopy .2. Determination of the stochastic contribution to the error structure. *J. Electrochem. Soc.* **142**, 4149-4158 (1995).

155 Okutan, M. & Yakuphanoglu, F. Analysis of interface states and series resistance of Ag/SiO2/n-Si MIS Schottky diode using current-voltage and impedance spectroscopy methods. *Microelectron. Eng.* **85**, 646-653 (2008).

156 Rhoderick, E. H. Metal-Semiconductor contacts. *IEE Proc.* **129**, 1-14 (1982).

157 Sze, S. M. & Ng, K. K. *Physics of Semiconductor Devices*. 3rd edn, 134-196 (John Wiley & Sons, Inc., 2007).

158 Auret, F. D. & Nel, M. Deep level transient spectroscopy of hole defects in bulk-grown p-GaAs using Schottky barrier diodes. *Appl. Phys. Lett.* **48**, 130-132 (1986).

159 Wang, C. D. *et al.* Deep level defects in n-type GaN grown by molecular beam epitaxy. *Appl. Phys. Lett.* **72**, 1211-1213 (1998).

160 Card, H. C. & Rhoderick, E. H. Studies of tunnel MOS diodes I. Interface effects in silicon Schottky diodes. *J. Phys. D: Appl. Phys.* **4**, 1589-1601 (1971).

161 Macdonald, J. R. & Johnson, W. B. in *Impedance Spectroscopy: Theory, Experiment, and Applications* (eds Evgenij Barsoukov & J. Ross Macdonald) Ch. 1, 1-26 (John Wiley & Sons, Inc., 2005).

162 Yim, C. Y. *et al.* Electrical properties of the ZnO nanowire transistor and its analysis with equivalent circuit model. *J. Korean Phys. Soc.* **48**, 1565-1569 (2006).

163 Huh, J., Na, J., Ha, J. S., Kim, S. & Kim, G. T. Asymmetric Contacts on a Single SnO2 Nanowire Device: An Investigation Using an Equivalent Circuit Model. *ACS Appl. Mater. Interfaces* **3**, 3097-3102 (2011).

164 Terrones, M. Carbon nanotubes: synthesis and properties, electronic devices and other emerging applications. *Int. Mater. Rev.* **49**, 325-377 (2004).

165 Anantram, M. P. & Leonard, F. Physics of carbon nanotube electronic devices. *Rep. Prog. Phys.* **69**, 507-561 (2006).

166 Balasubramanian, K. & Burghard, M. Electrochemically functionalized carbon nanotubes for device applications. *J. Mater. Chem.* **18**, 3071-3083 (2008).

167 Liu, Z., Jiao, L., Yao, Y., Xian, X. & Zhang, J. Aligned, Ultralong Single-Walled Carbon Nanotubes: From Synthesis, Sorting, to Electronic Devices. *Adv. Mater.* **22**, 2285-2310 (2010).

168 Nourbakhsh, A. *et al.* Modified, semiconducting graphene in contact with a metal: Characterization of the Schottky diode. *Appl. Phys. Lett.* **97**, 163101 (2010).

169 Tongay, S., Schumann, T., Miao, X., Appleton, B. R. & Hebard, A. F. Tuning Schottky diodes at the many-layer-graphene/semiconductor interface by doping. *Carbon* **49**, 2033-2038 (2011).

170 Chen, C.-C., Aykol, M., Chang, C.-C., Levi, A. F. J. & Cronin, S. B. Graphene-Silicon Schottky Diodes. *Nano Lett.* **11**, 1863-1867 (2011).

171 López-Honorato, E., Meadows, P. J. & Xiao, P. Fluidized bed chemical vapor deposition of pyrolytic carbon – I. Effect of deposition conditions on microstructure. *Carbon* **47**, 396-410 (2009).

172 Tuinstra, F. & Koenig, J. L. Raman Spectrum of Graphite. *The Journal of Chemical Physics* **53**, 1126-1130 (1970).

173 Cançado, L. G. *et al.* General equation for the determination of the crystallite size La of nanographite by Raman spectroscopy. *Appl. Phys. Lett.* **88**, 163106 (2006).

174 Vallerot, J.-M., Bourrat, X., Mouchon, A. & Chollon, G. Quantitative structural and textural assessment of laminar pyrocarbons through Raman spectroscopy, electron diffraction and few other techniques. *Carbon* **44**, 1833-1844 (2006).

175 Cançado, L. G. *et al.* Quantifying Defects in Graphene via Raman Spectroscopy at Different Excitation Energies. *Nano Lett.* **11**, 3190-3196 (2011).

176 Jellison Jr., G. E. & Modine, F. A. Parameterization of the optical functions of amorphous materials in the interband region. *Appl. Phys. Lett.* **69**, 371-373 (1996).

177 Tian, H., Bergren, A. J. & McCreery, R. L. Ultraviolet-visible spectroelectrochemistry of chemisorbed molecular layers on optically transparent carbon electrodes. *Appl. Spectrosc.* **61**, 1246-1253 (2007).

178 Stagg, B. J. & Charalampopoulos, T. T. Refractive indices of pyrolytic graphite, amorphous carbon, and flame soot in the temperature range 25° to 600°C. *Combust. Flame* **94**, 381-396 (1993).

179 Rhoderick, E. H. & Williams, R. H. *Metal–Semiconductor Contacts*. 2nd edn, 252 (Clarendon Press, 1988).

180 Cheung, S. K. & Cheung, N. W. Extraction of Schottky Diode Parameters from Forward Current-Voltage Characteristics. *Appl. Phys. Lett.* **49**, 85-87 (1986).

181 Kavasoglu, A. S., Kavasoglu, N. & Oktik, S. Simulation for capacitance correction from Nyquist plot of complex impedance–voltage characteristics. *Solid-State Electron.* **52**, 990-996 (2008).

182 Hacke, P., Detchprohm, T., Hiramatsu, K. & Sawaki, N. Schottky barrier on n-type GaN grown by hydride vapor phase epitaxy. *Appl. Phys. Lett.* **63**, 2676-2678 (1993).

183 Ishigami, M., Chen, J. H., Cullen, W. G., Fuhrer, M. S. & Williams, E. D. Atomic Structure of Graphene on SiO2. *Nano Lett.* **7**, 1643-1648 (2007).

184 Das, B., Voggu, R., Rout, C. S. & Rao, C. N. R. Changes in the electronic structure and properties of graphene induced by molecular charge-transfer. *Chem. Commun.*, 5155-5157 (2008).

185 Krupka, J. & Strupinski, W. Measurements of the sheet resistance and conductivity of thin epitaxial graphene and SiC films. *Appl. Phys. Lett.* **96**, 082101 (2010).

186 Feng, T. *et al.* Graphene based Schottky junction solar cells on patterned silicon-pillar-array substrate. *Appl. Phys. Lett.* **99**, 233505 (2011).

187 Chen, F., Qing, Q., Xia, J., Li, J. & Tao, N. Electrochemical Gate-Controlled Charge Transport in Graphene in Ionic Liquid and Aqueous Solution. *J. Am. Chem. Soc.* **131**, 9908-9909 (2009).

188 Keeley, G. P. *et al.* DMF-exfoliated graphene for electrochemical NADH detection. *Phys. Chem. Chem. Phys.* **13**, 7747-7750 (2011).

189 Tongay, S. *et al.* Graphene/GaN Schottky diodes: Stability at elevated temperatures. *Appl. Phys. Lett.* **99**, 102102 (2011).

190 Li, X. *et al.* Graphene-On-Silicon Schottky Junction Solar Cells. *Adv. Mater.* **22**, 2743-2748 (2010).

191 Miao, X. *et al.* High Efficiency Graphene Solar Cells by Chemical Doping. *Nano Lett.* **12**, 2745-2750 (2012).

192 Yang, H. *et al.* Graphene Barristor, a Triode Device with a Gate-Controlled Schottky Barrier. *Science* **336**, 1140-1143 (2012).

193 Kim, H.-Y., Lee, K., McEvoy, N., Yim, C. & Duesberg, G. S. Chemically Modulated Graphene Diodes. *Nano Lett.* **13**, 2182-2188 (2013).

194 Yim, C., McEvoy, N., Kim, H.-Y., Rezvani, E. & Duesberg, G. S. Investigation of the Interfaces in Schottky Diodes Using Equivalent Circuit Models. *ACS Appl. Mater. Interfaces* **5**, 6951–6958 (2013).

195 Tongay, S. *et al.* Rectification at Graphene-Semiconductor Interfaces: Zero-Gap Semiconductor-Based Diodes. *Phys. Rev. X* **2**, 011002 (2012).

196 Tung, R. T. Recent advances in Schottky barrier concepts. *Mater. Sci. Eng. R* **35**, 1-138 (2001).

197 Werner, J. H. & Guttler, H. H. Barrier inhomogeneities at Schottky contacts. *J. Appl. Phys.* **69**, 1522-1533 (1991).

198 Werner, J. H. & Guttler, H. H. Temperature dependence of Schottky barrier heights on silicon. *J. Appl. Phys.* **73**, 1315-1319 (1993).

199 Tongay, S., Schumann, T. & Hebard, A. F. Graphite based Schottky diodes formed on Si, GaAs, and 4H-SiC substrates. *Appl. Phys. Lett.* **95**, 222103 (2009).

200 Lopez-Sanchez, O. *et al.* Light Generation and Harvesting in a van der Waals Heterostructure. *ACS Nano* **8**, 3042-3048 (2014).

201 Lee, K., Gatensby, R., McEvoy, N., Hallam, T. & Duesberg, G. S. High Performance Sensors Based on Molybdenum Disulfide Thin Films. *Adv. Mater.* **25**, 6699-6702 (2013).

202 Yim, C., McEvoy, N. & Duesberg, G. S. Characterization of graphene-silicon Schottky barrier diodes using impedance spectroscopy. *Appl. Phys. Lett.* **103**, 193106 (2013).

203 Yim, C. *et al.* Investigation of the optical properties of MoS_2 thin films using spectroscopic ellipsometry. *Appl. Phys. Lett.* **104**, 103114 (2014).

204 Joensen, P., Crozier, E. D., Alberding, N. & Frindt, R. F. A study of single-layer and restacked MoS_2 by X-ray diffraction and X-ray absorption spectroscopy. *J. Phys. C: Solid State Phys.* **20**, 4043-4053 (1987).

205 Ataca, C. & Ciraci, S. Functionalization of Single-Layer MoS_2 Honeycomb Structures. *J. Phys. Chem. C* **115**, 13303-13311 (2011).

206 Ataca, C., Topsakal, M., Aktürk, E. & Ciraci, S. A Comparative Study of Lattice Dynamics of Three- and Two-Dimensional MoS2. *J. Phys. Chem. C* **115**, 16354-16361 (2011).

207 Shi, Y. *et al.* van der Waals Epitaxy of MoS_2 Layers Using Graphene As Growth Templates. *Nano Lett.* **12**, 2784-2791 (2012).

208 Lembke, D. & Kis, A. Breakdown of High-Performance Monolayer MoS2 Transistors. *ACS Nano* **6**, 10070-10075 (2012).

209 Choi, W. *et al.* High-Detectivity Multilayer MoS2 Phototransistors with Spectral Response from Ultraviolet to Infrared. *Adv. Mater.* **24**, 5832-5836 (2012).

210 Esmaeili-Rad, M. R. & Salahuddin, S. High Performance Molybdenum Disulfide Amorphous Silicon Heterojunction Photodetector. *Sci. Rep.* **3**, 2345 (2013).

211 Xia, F., Mueller, T., Lin, Y.-m., Valdes-Garcia, A. & Avouris, P. Ultrafast graphene photodetector. *Nat. Nanotechnol.* **4**, 839-843 (2009).

212 Wilson, J. A. & Yoffe, A. D. The transition metal dichalcogenides discussion and interpretation of the observed optical, electrical and structural properties. *Adv. Phys.* **18**, 193-335 (1969).

213 Kumar, B. *et al.* The Role of External Defects in Chemical Sensing of Graphene Field-Effect Transistors. *Nano Lett.* **13**, 1962-1968 (2013).

214 Ang, P. K., Chen, W., Wee, A. T. S. & Loh, K. P. Solution-Gated Epitaxial Graphene as pH Sensor. *J. Am. Chem. Soc.* **130**, 14392-+ (2008).

215 Cheng, Z., Li, Q., Li, Z., Zhou, Q. & Fang, Y. Suspended Graphene Sensors with Improved Signal and Reduced Noise. *Nano Lett.* **10**, 1864-1868 (2010).

216 van der Zande, A. M. *et al.* Grains and grain boundaries in highly crystalline monolayer molybdenum disulphide. *Nat. Mater.* **12**, 554-561 (2013).

217 Park, W. *et al.* Photoelectron Spectroscopic Imaging and Device Applications of Large-Area Patternable Single-Layer MoS2 Synthesized by Chemical Vapor Deposition. *ACS Nano* **8**, 4961-4968 (2014).

218 Schmidt, H. *et al.* Transport Properties of Monolayer MoS2 Grown by Chemical Vapor Deposition. *Nano Lett.* **14**, 1909-1913 (2014).

219 Conley, H. J. *et al.* Bandgap Engineering of Strained Monolayer and Bilayer MoS2. *Nano Lett.* **13**, 3626-3630 (2013).

220 Liu, Z. *et al.* Strain and structure heterogeneity in MoS2 atomic layers grown by chemical vapour deposition. *Nature Communications* **5**, 5246 (2014).

221 Kravets, V. G. *et al.* Spectroscopic ellipsometry of graphene and an exciton-shifted van Hove peak in absorption. *Phys. Rev. B* **81**, 155413 (2010).

222 Nelson, F. J. *et al.* Optical properties of large-area polycrystalline chemical vapor deposited graphene by spectroscopic ellipsometry. *Appl. Phys. Lett.* **97**, 253110 (2010).

223 Weber, J. W., Calado, V. E. & van de Sanden, M. C. M. Optical constants of graphene measured by spectroscopic ellipsometry. *Appl. Phys. Lett.* **97**, 091904 (2010).

224 Matkovic, A. *et al.* Influence of transfer residue on the optical properties of chemical vapor deposited graphene investigated through spectroscopic ellipsometry. *J. Appl. Phys.* **114**, 093505 (2013).

225 Woollam, J. A. *CompleteEASE^{TM} Data Analysis Manual Version 4.63*. 45-46 (J. A. Woollam Co., Inc., 2011).

226 Herzinger, C. M., Johs, B., McGahan, W. A., Woollam, J. A. & Paulson, W. Ellipsometric determination of optical constants for silicon and thermally grown silicon dioxide via a multi-sample, multi-wavelength, multi-angle investigation. *J. Appl. Phys.* **83**, 3323-3336 (1998).

227 Koffyberg, F. P., Dwight, K. & Wold, A. Interband transitions of semiconducting oxides determined from photoelectrolysis spectra. *Solid State Commun.* **30**, 433-437 (1979).

228 Shaaban, E. R., Abd El-Sadek, M. S., El-Hagary, M. & Yahia, I. S. Spectroscopic ellipsometry investigations of the optical constants of nanocrystalline SnS thin films. *Phys. Scr.* **86**, 015702 (2012).